UNIVERSITY OF SOUTHAMPTON

FACULTY OF PHYSICAL AND APPLIED SCIENCES

School of Physics and Astronomy

Terahertz emission from ultrafast lateral diffusion currents within semiconductor devices

by

Mark E. Barnes

Thesis for the degree of Doctor of Philosophy

January 2014

To Eden

UNIVERSITY OF SOUTHAMPTON

ABSTRACT

FACULTY OF PHYSICAL AND APPLIED SCIENCES
School of Physics and Astronomy

Doctor of Philosophy

TERAHERTZ EMISSION FROM ULTRAFAST LATERAL DIFFUSION CURRENTS WITHIN SEMICONDUCTOR DEVICES

by Mark E. Barnes

Single cycle THz emission from unbiased semiconductor devices after ultrafast carrier excitation can be attributed to surge currents on the surface of the device. These currents are due to either drift currents where carriers are accelerated by an internal electric field perpendicular to the surface (surface field effect) or diffusion currents where a separation of charge forms due to electrons and holes having different mobilities (photo-Dember effect). This surface emission is difficult to out couple from the semiconductor device as the emission is parallel to the surface of the semiconductor. This difficulty in out coupling led to a decline in interest for these types of emitters in preference to photoconductive emitters which today are the standard type of emitters used in THz time domain spectroscopy. In recent years a new type of surface emitter based on lateral diffusion currents (lateral Dember currents) has been proposed and demonstrated. This work acted as the initial inspiration for the work described within this thesis. The emission was attributed to net diffusion currents that formed from an initially asymmetrical carrier distribution that formed due to partially masking the pump spot with a metal mask.

Simulations of the situation revealed that diffusion alone cannot account for the observed THz emission from these devices. From this I have extended the mechanism taking into account lateral diffusion currents and dipole suppression under a metal mask. Along with theoretical arguments experimental evidence is given that supports this new theory. These devices are further explored experimentally giving insights into the nature of the emission and how it depends on different pump parameters and external electric fields. Based on this new interpretation I present the design, fabrication, and testing of multiplex emitters that are are comparable with commercial photoconductive emitters in both power and band-width.

Contents

List of Figures

List of Tables

Declaration of Authorship

I, Mark E. Barnes , declare that the thesis entitled *Terahertz emission from ultrafast lateral diffusion currents within semiconductor devices* and the work presented in the thesis are both my own, and have been generated by me as the result of my own original research. I confirm that:

- this work was done wholly or mainly while in candidature for a research degree at this University;
- where any part of this thesis has previously been submitted for a degree or any other qualification at this University or any other institution, this has been clearly stated;
- where I have consulted the published work of others, this is always clearly attributed;
- where I have quoted from the work of others, the source is always given. With the exception of such quotations, this thesis is entirely my own work;
- I have acknowledged all main sources of help;
- where the thesis is based on work done by myself jointly with others, I have made clear exactly what was done by others and what I have contributed myself;
- none of this work has been published before submission

Signed:.....

Date:.....

Acknowledgements

First and foremost, I would like to thank my supervisor Dr. Vasilis Apostolopoulos for his help, support, and guidances during my PhD. I would like to thank Prof. Anne Tropper for her encouragement and insights before undertaking and during my PhD. I would also like to thank Dr. Geoff Daniell for his help on the theory and for interesting discussions on topics from Linux distributions to trumpets.
I would like to thank Dr. Zakaria Mihoubi for showing me the ropes of THz-TDS and I would like to thank Dr. Adrian Quaterman and Dr. Keith Wilcox for informative discussions early on in my research. I would like to thank Duncan McBryde who has worked along side or in collaboration with me and for being a good friend. I would like to also thank the rest of the THz group; Sam Berry, Paul Gow, Lewis Maple, Aaron Chung, Elean Mavrona and Jo Carthy.
On a personal note I would like to thank my family; my parents without whom I would not be here and my siblings, Lizzy, Chris, and Lloyd who are all tired of hearing about my research without understanding a word of what I was talking about. I would like to thank the lords and ladies of Entropy who I lived with during my studies. Especially Hannah for her love and support. And finally I would like to thank the rest of my close friends for their support and the warnings from friends that have been along this path before.

Chapter 1

Introduction

The motivation of the work presented here is to study and understand the origin and mechanism of single cycle, broadband, coherent Terahertz (THz) emission from partially masked semiconductor devices after ultrafast illumination from a band-gap matched laser source at a metal:semiconductor interface. In this work competing arguments for the mechanism involved are presented. Through theoretical arguments and experimental evidence the emission is shown to originate from lateral diffusion currents and partial suppression of radiating dipoles due to their proximity to a metal mask. Computational modelling shows that diffusion alone cannot account for the observed THz emission without the inclusion of dipole suppression. Experimental evidence confirms this as well validating the models and provides further insight. These devices are experimentally studied further to better understand the mechanism involved. Finally multiplex emitters are fabricated and tested based on the complete theory. These devices are shown to be comparable to state of the art commercial emitters in both power and bandwidth while being more durable and easier to fabricate.
This introduction contains a brief discussion of THz science and applications. It then gives a detailed description of the functionality of THz time domain spectrometers and explains the mechanisms involved for popular THz emission and detection schemes.
This chapter also outlines previous work on lateral photo-Dember emitters like the ones studied in this thesis as well as an explanation of the mechanism discovered during my PhD studies. Finally, I outline the contents of this thesis.

1.1 The Electromagnetic Spectrum and The Terahertz Gap

Terahertz (THz) radiation has a wavelength of 30 μm (30 THz) to 3 mm (100 GHz) sitting between microwaves and the long wave edge of far-infrared as shown in Fig. 1.1, these frequencies correspond to energies from 40 meV to 0.4 meV.

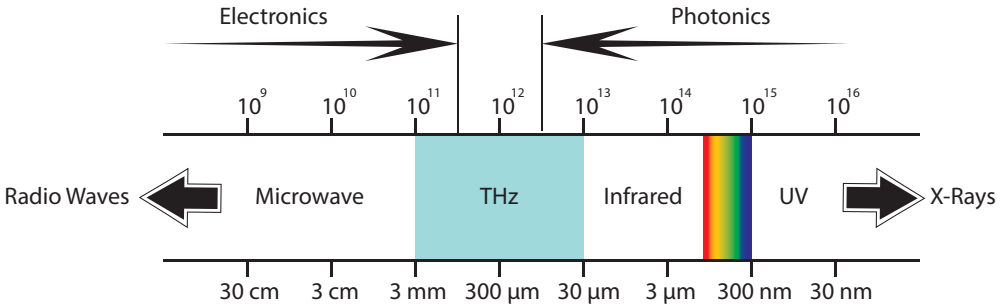

Figure 1.1: Schematic diagram showing the location of the THz region in the electromagnetic spectrum.

Incoherent THz radiation is abundant from thermal sources as anything with a temperature above 10 K will emit THz radiation as part of its black body radiation. Results from the NASA's Diffuse Infrared Background Experiment (DIRBE) on board the COBE satellite revealed that more than half the luminosity of the galaxy and 98% of photons emitted since the Big Bang fall within the THz region of the electromagnetic spectrum [3]. Emission from cool interstellar dust is the origin of most of this radiation, and thus conveys important information in both the temporal and spectral domains for insight into star formation and decay [4].

Many mature devices exist either side of the THz region within the infrared and microwaves. Despite this the THz region is lacking efficient sources and detectors and only recently has significant development started. The reason for this is because THz radiation bridges the gap between optical and electronic technologies. This makes it hard to adapt technologies from either side of the spectrum without suffering from reduced efficiency. For sources based on electronic oscillators the power rolls off beyond frequencies of tens of GHz as the devices becomes more unresponsive. Where as optical devices based on semiconductor technologies do not function well as the energy band-gap for THz is small compared with lattice phonon energy. The term 'Terahertz Gap' was coined to emphasise the lack of efficient, coherent sources, and detectors in this region.

Within the THz region many molecular vibrational, and rotational modes exist, making THz radiation a vital probe for the detection, identification, and study of chemical species. This has promoted much scientific interest in the THz region as it promises

	Electronic Sources		**Electro-Optical Sources**		**Optical Sources**	
	Backward Wave Oscillators	Multipliers	Photomixing	PC Switches	QCL	Germanium lasers
Average Power	mW	mW	nW	μW	mW	mW
Usable Range (THz)	0.1 - 10	0.1 - 1.5	0.3 - 10	0.1 - 10	2 - 10	0.3 - 10
Tunability	20%	15%	0.3 - 10 THz	N/A	10 GHz	Discrete Lines
CW/Pulsed	CW/Pulsed	CW	CW	Pulsed	CW	CW/Pulsed

Table 1.1: Table of THz Sources.

many potential applications. Despite this it has remained elusive due to the lack of efficient, long-lived, compact, coherent emitters, and detectors. This has also hindered transitioning THz technologies from research laboratories to real world applications.
Today there is a plethora of generation schemes for THz, such as gyrotrons, synchrotrons, quantum cascade lasers (QCL), photoconductive antennas (PCA), the photo-Dember effect, non-linear crystals, air plasma, p-type Germanium lasers, Gunn diodes, multipliers, backward wave oscillators, parametric oscillators, and surface field emission. Table 1.1 shows a comparison of some typical THz sources. Terahertz spectroscopy is the oldest and most common application of THz radiation. Many chemical species have strong spectral absorption lines due to rotational and vibrational modes sitting in the THz region [5], which triggered the initial interest to THz by Astronomy. This is most true for many gasses, which have narrow absorption lines in the far-infrared (FIR), for example water vapour, oxygen, and carbon monoxide. THz radiation is also sensitive to the dynamics of charged carriers within devices that happen within the picosecond time scale [6].
It is also possible to collimate and focus THz beams to the diffraction limit making it flexible for spectroscopy and imaging applications. The flexibility of THz spectroscopy systems facilitate different configurations that allow for probing of the carrier dynamics within bulk semiconductors [7], quantum wells [8], quantum dots [9], nanoparticles [10], and full semiconductor devices such as photovoltaic solar cells [11].

1.2 History

Traditionally the THz region was encompassed by the 'far-infrared' region of the electromagnetic spectrum. Its promotion to its own region is not just a simple case of semantics but represents a new field of scientific endeavour. Prior to the invention of ultrafast optical laser pulses, the most common source of THz radiation were black body radiation sources such as thermal lamps which produce weak CW incoherent THz radiation. For detection, sensors based on heterodyne schemes were implemented for spectroscopy applications but they are not useful with thermal lamps due to the lamps limited spectral intensity [3]. Other detectors were bolometers and Golay cells which are still commonly used for detection of CW sources. A bolometer measures the resistivity of a material with a temperature-dependent electrical resistance. When the material is heated by an incident electromagnetic wave its resistance measured which is proportional to the intensity of the electric field. A Golay cell is also a thermal measurement, it consists of an encased gas in an enclosure with a flexible diaphragm that deforms when the gas is heated. The deformation of this diaphragm is measured by reflecting a infrared LED off the surface and measured with a photo-Diode. In the late 1960s and 1970s with the increasing progress in the development of semiconductors, nonlinear optics, and the invention of the laser new fields were born, namely optoelectronics and photonics. The development within these fields lead to lasers with shorter pulses as new mechanisms for mode-locking were developed.

In the mid-1970s photoconductive switches pumped by laser pulses were pioneered by Auston [12] and Lee [13] using mode locked Nd:glass lasers and high-resistivity Si, or semi-insulating GaAs substrates for the switches.

Also in the 1970s two different groups [14, 15] independently generated far-infrared pulses just within the THz region from non-linear crystals.

As laser pulses got shorter in 1984 Auston et al.[16] generated 1.6 ps THz pulses which they detected with another photoconductive switch on the opposite side of a dielectric slab from the emitter giving birth to optoelectronic THz technologies and modern THz science. Auston also investigated THz emission from nonlinear rectification in the same year [17] and in the following year used it for spectroscopy [18].

In 1987, DeFonzo [19, 20] allowed for the THz pulses to propagate freely in air before detection. Making THz systems more flexible and attractive for other areas of research.

In 1989, van Exter et al. [21] demonstrated the first use of pulsed THz emission from photoconductive switches being used for THz time domain spectroscopy and measured the spectrum of water vapour.

The self-mode-locked Ti:S laser, invented in 1991 [22], was capable of generating sub-100 fs pulses. The subsequent commercialisation of these lasers spread the interest of THz pulses. At the same time MBE growth of low temperature (LT) GaAs was starting

to be used for photoconductive switches because of its fast carrier life time and large mobilities which can be tailored by changing the substrate temperature during growth. LT-GaAs today is still the most common substrate for THz photoconductive antenna switches.
In 1995, Wu et al. [23] demonstrated detection of THz pulses using non-linear crystals. They did this by utilising the Pockels effect also known as the linear electro-optical effect. This detection method is attractive as it allows for a flat frequency response over a large frequency range in comparison to photoconductive detectors.
In more recent years THz technologies have matured and used within a wide range of scientific and commercial application.

1.3 Applications of THz Radiation

Many materials that are opaque at visible frequencies are transparent in the THz region, such as plastics, ceramics, clothing, and paper [24]. In the case of dielectrics, absorption is dominated by optical phonons with energies above that of THz radiation [6]. Unlike X-Rays, THz radiation is non-ionising and does not damage DNA. This makes it useful as a non-disruptive probe of otherwise opaque materials. Organic molecule crystals have distinct vibrational modes that extend over large domains of a crystal lattice in the THz region making THz spectroscopy a unique spectroscopic tool. Furthermore, absorption of THz by matter results in, or originates from, carrier transport, thus THz spectra give information about carrier concentration, mobility, and dynamics [25]. THz pulses can also be used for imaging as first demonstrated by Hu et al. [26] in 1995; with THz imaging it is possible to get full spectral information for each pixel. Consequently, THz is attractive for a wide range of applications in areas such as security (airport scanners), medical imaging (cancer identification, pharmaceuticals), quality control and fundamental science.
Apart from sensing and characterisation applications THz radiation is increasingly used in information and communication technologies where it is employed for a wide range of applications such as wireless communications and high speed applications.

1.3.1 Biological, Pharmaceutical, and Medical Applications

Unlike infrared spectroscopy, terahertz spectroscopy allows for the observation of intermolecular vibrations [27] in many chemicals and organic molecules. This allows for enhanced studies of molecular systems giving insight into the dynamics of large biomolecular systems that will increase our knowledge of biology. THz radiation can

penetrate tissue over several millimetres if there is low water content such as fatty tissue and reflect back.

The existing technology within medical imaging is diverse utilising ultasound, X-ray systems, magnetic resonance imaging (MRI), optical tomography, and even positron emission tomography (PET). While mature, all these technologies have shortcomings, be it safety issues from X-ray sources, cost such as MRI or resolution limitations. As THz technologies mature they promise to show advantages over current technologies for numerous applications.

Two often cited applications of THz radiation within medical imaging is that of 3D dental imaging [28] and the identification of cancerous tissue within human skin [29]. In dentistry the early identification of dental caries is critical to prevent severe damage and the need for invasive drilling. Visual identification is difficult and dental X-rays carry a health risk so cannot be used frequently. THz radiation is not ionising and thus can be used as often as needed increasing the likelihood of early identification. THz radiation is also able to identify subtle changes in skin tissue allowing for the early detection of some skin cancers. Further ex vivo and in vivo studies [30] have shown that identification of cancerous tumours is possible with THz radiation due to the difference in hydration of healthy and cancerous tissue. Imaging of these tumours insure for better surgical removal reducing both tissue scarring and chance of recurrence.

Apart from the identification of different chemicals, Terahertz spectroscopy can also identify different crystalline structures of the same material (polymorphic structures). Different crystalline structures of the same chemical can have different physical and chemical properties which thus change its pharmaceutical properties. Classification of polymorphs in medicine [27] is important for pharmaceuticals and health. Popular methods for classification of polymorphs is X-ray diffraction and Raman spectroscopy but they are not without their problems. X-ray diffraction requires large crystalline structures whereas Raman spectroscopy is not a direct probe and can induce phase changes during measurement. Terahertz spectroscopy does not induce phase changes and is non-destructive [27]. THz imaging technologies have been developed with analysis of pharmaceutical tablets in mind. These systems are able to generate 3D THz images with spectroscopic information. This information allows for the identification of the chemical and structure. The images are also able to locate the active ingredient within the pill and also the thickness and quality of coatings.

1.3.2 Security Applications

Most fabric and plastics are transparent in the THz region allowing for THz to image concealed objects. Explosives and other contraband materials have distinct absorption

spectra making THz an ideal probe for security screening. This has lead to the development and commercialisation of THz scanners being used as scanners in airport security. Full body scanners however do pose questions about privacy and effectiveness [31].
Other security devices are available for scanning objects such as envelopes or packages for contraband. THz imaging is able to give spatial and spectral imaging of the hidden object allowing for identification without opening the package [32].

1.3.3 Quality Control

Paper, card, fabrics, plastics, and semiconductors are transparent in the THz region. This enables THz technologies to be useful for in-line quality control and non-destructive testing.
THz imaging has been used for inspection of the foam insulation of space shuttles as it is able to identify defects in the panels and is now part of routine checks [33]. THz radiation proves to be a unique probe for carrier dynamics of semiconductor devices and has been used for inspections for solar cells, nano materials, and films [11, 34, 35, 36]. Imaging of semiconductor devices even allows for identification of different doping levels. THz sources have also proven to be a useful tool for identification of damaged semiconductor devices.

1.3.4 Information and Communication Technologies

Higher frequencies allow for higher bandwidths in wireless communication. Today we are seeing an unprecedented increase in mobile data requirements with an increasing need for higher bandwidths driven by the smart phone market. To address this increasing demand, telecommunication companies have to look at higher frequency solutions pushing into the THz region. Several different approaches have been realised for wireless communication at terahertz frequency with bit rates above 100 Gb/s. Fibre linked wireless systems have set world record bandwidths for wireless communications with bit rates above 400 Gb/s ushering in a new era of ultrafast wireless communication [37].

1.3.5 Art Conservation

Art works are often subject to restoration for preservation. During restoration it is prudent to make a detailed analysis of the original materials and techniques used by

the original artist. If previous restorations have been made the conservator needs to decide if these layers should be removed. A range of tools are available to study paintings [38]. Popular tools are photographic examinations, X-ray fluorescence, and IR spectroscopy. These methods can however be limited and or destructive.
THz radiation can penetrate the paint deeper than any other non-destructive method. THz time domain reflection imaging is able to detect the layers, materials used, and produce a 3D internal image of the painting if raster scanned. No other commonly used method is able to extract this information without being destructive. The use of THz radiation being used for art restoration has already been demonstrated [39].
These techniques can also reveal hidden paintings that the original artist has painted over or originate from criminal damage and forgeries [40]. Recently a fresco was revealed using THz time domain reflection imaging of a painting by Gimapetro Campana at the Louvre museum in Paris [41]. The imaging showed the original Roman Fresco on which Campana painted his forgery. Other methods had been tried to reveal the hidden Fresco but it was only possible with THz radiation.

1.4 Terahertz Time Domain Spectrometer

A milestone for THz science was the demonstration of the generation of freely propagating broadband, single cycle pulses from photoconductive antenna (PCA) by D. H. Auston et al. [16] in 1984. These sources directly led to the application of THz time domain spectroscopy (THz-TDS). THz-TDS employs a synchronous detection scheme resembling a pump-probe setup with inherent high signal to noise ratio which allows for accurate measurements. As the electric field is directly measured within THz-TDS it is not only possible to measure the amplitude information but also the phase which gives it a major advantage over other spectroscopy systems.
THz emitters used in THz-TDS can be broadly divided into two classes. Those based on non-linear frequency conversion of a femtosecond laser spectrum to the THz frequency range and those based on ultrafast currents involving carrier generation, acceleration, and annihilation.
A schematic of a typical THz-TDS system is shown in Fig. 1.2. The beam from an ultrafast laser source is spit into two by an optical beam splitter. The beams are sent along two arms of the setup. One arm leads to the emitter and the other to the detector. The laser pulse is incident on the THz emitter generating a THz pulse which is then propagated by the THz mirrors and or lenses before it is focused onto the detector. The other arm focuses the optical laser pulse onto the detector where it gates the detector measuring the electric field of the THz radiation at a small point in time relative to the length of the THz pulse. By varying the length of either arm using an

optical delay stage the electric field of the THz pulse can be mapped out in time by the detector. The emitter is either electrically or optically modulated to allow for lock-in detection increasing the signal to noise ratio. By applying a Fourier transform onto the data both the amplitude and phase information of the pulse can be found.

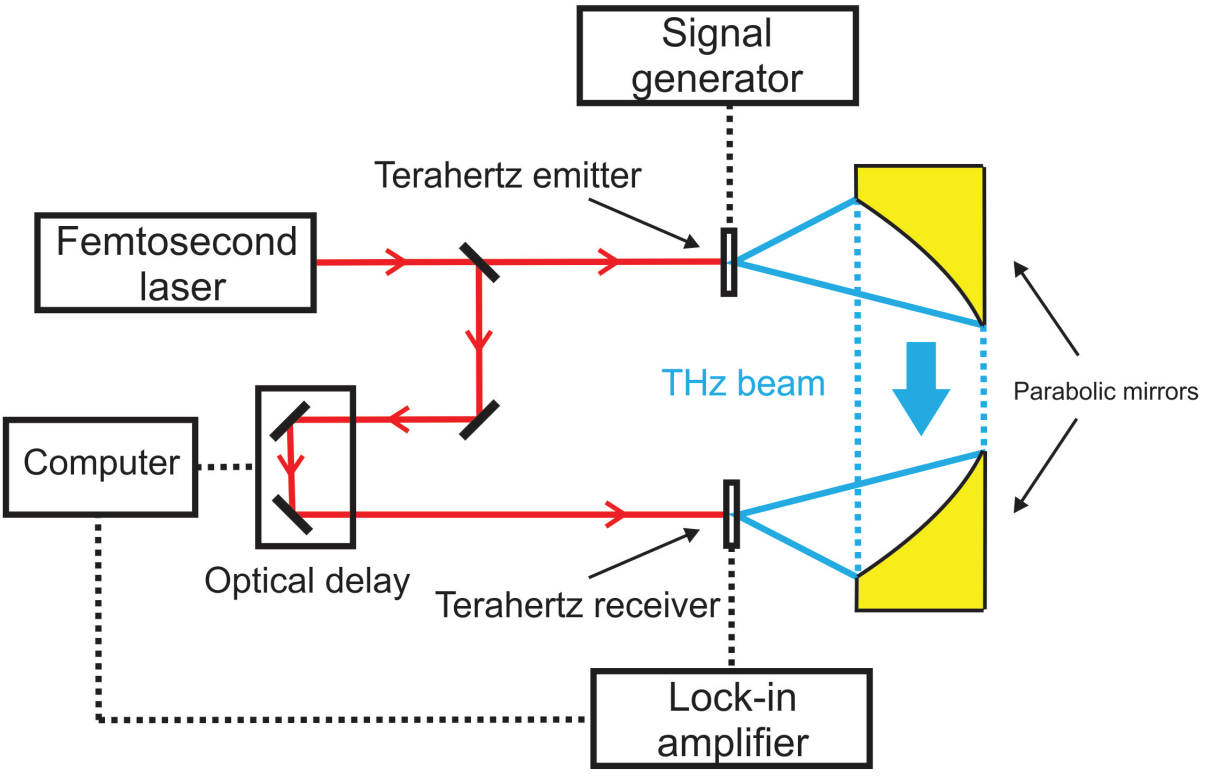

Figure 1.2: Schematic of a typical THz-TDS setup.

For spectroscopy applications a sample is placed within the THz beam path and a trace of the THz electric field is measured. This measurement is compared with a reference scan made without any sample present allowing for both amplitude and phase information of the materials transfer function to be measured using algorithms that model the system [42, 43, 44, 45].

1.5 Generation of THz Pulses

1.5.1 Photoconductive Antennas

In THz-TDS the most commonly used emitters and detectors are gallium arsenide photoconductive antennas (PCS) [46]. These antennas usually have a bandwidth spanning from 100 GHz to 2-3 THz. PC antennas consist of two electrodes fabricated on top of the semiconductor separated by a gap of some microns [47, 48]. For emission a potential is applied to the electrodes which establishes a strong electric field (in the region of 100 kV cm^{-1}) across the antenna gap. A titanium sapphire (Ti:S) ultrafast laser is commonly used to excite carriers across the band-gap of gallium arsenide. An illustration of a bow-tie emitter is shown in Fig. 1.3.

Upon illumination from the femtosecond laser ultrafast carriers are generated and

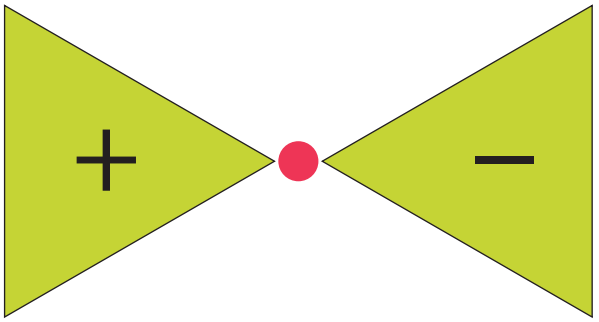

Figure 1.3: Illustration of a typical bowtie emitter. The red dot is the focused laser beam between the two biased antenna structures fabricated on a semiconductor material with a band-gap that matches the energy of the laser.

accelerated by the applied electric field. The leading edge of the laser pulse creates an initially fast changing dipole as photo-carriers are generated and accelerated. The carriers are then quickly recaptured by defect trap sites and carrier-carrier recombination. This fast current sets up and destroys a fast changing dipole that is the source of broadband THz radiation. Typically the gap used in photoconductive emitters is sub wavelength and thus the radiating dipole can be described as a Hertzian dipole that has an emission profile given by

$$E_{THz}(r,t,\theta) = \frac{l_e}{4\pi\epsilon_e c^2 r}\frac{\partial J(t)}{\partial t}\sin\theta \tag{1.1}$$

where $J(t)$ is the photo-current contributing to the emitting dipole, l_e is the effective length of the dipole, ϵ_0 is the permittivity of free space, c is the speed of light, and θ is the angle from the dipole. The emitted electric field is thus proportional to the rate of change of the photo-current. Fig. 1.4 shows the evolution of emitted THz emission

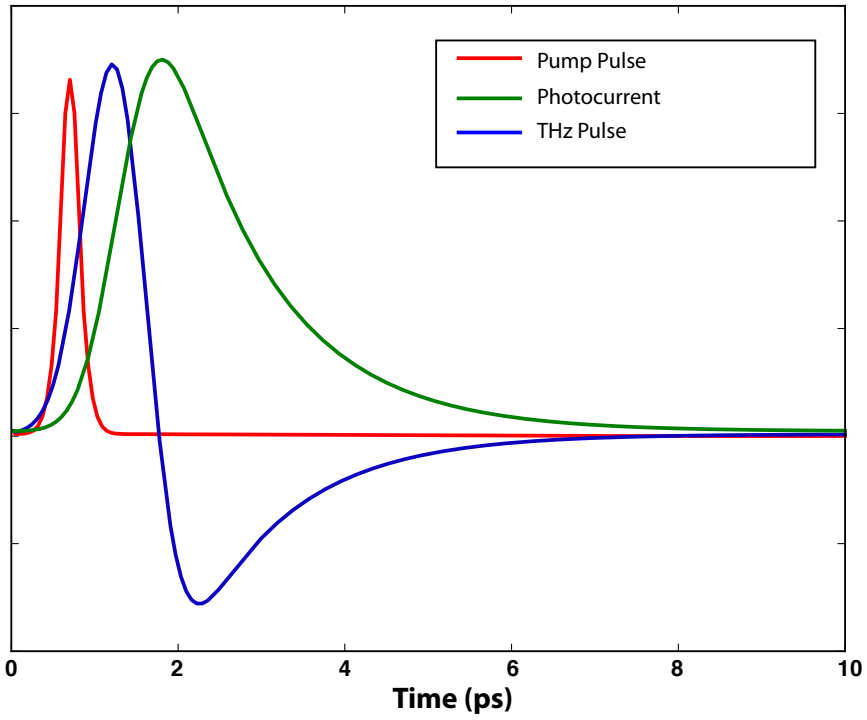

Figure 1.4: Relationship between the optical pulse, photo-current, and emitted THz radiation.

with respect to both the optical pulse and photo-current. The photo-current density in the emitter is the convolution of the temporal envelope of the optical field and the impulse response of the photoconductive switch described by

$$j_{em}(t) = P_{opt}(t) * [n_{em}(t) q v_{em}(t)] \tag{1.2}$$

where $*$ denotes the convolution product, $P_{opt}(t)$ is the optical power, q is the charge, n_{em} is the carrier density, and $v_{em}(t)$ is the drift velocity of the photo-carriers.

1.5.2 Optical Rectification

Another popular emitter is based on the optical rectification of a sub-picosecond laser pulse by a nonlinear crystal. Optical rectification is analogous to electronic rectification where an AC current is transformed into a DC electrical bias. The strength of the bias is proportional to the amplitude of the AC current. For optical rectification of an optical pulse the instantaneous polarisation has a DC component that follows the square of the amplitude of the electric field and thus the intensity of pulse with time, this

phenomenon stems from the second order material susceptibility, $\chi^{(2)}$. By expanding the polarisation, $P(t) = E(t)\epsilon_0\chi$, the second order term gives the contribution $P_2(t) = \epsilon_0\chi^{(2)}E^2(t)$. If we assume an oscillating electric field, $E(t) = E_0\cos(\omega t)$, we find that

$$P_2 = \epsilon_0\chi^{(2)}E_0^2\cos^2(\omega t) = \frac{\epsilon_0\chi^{(2)}E_0^2}{2}\left(1+\cos(2\omega t)\right) \tag{1.3}$$

Here we can see two different components making up the contribution to the second order polarisation. The first term is a DC term which gives us optical rectification where as the second term is second-harmonic generation (SHG). As our pump laser is pulsed the material polarization will follow the envelope of our pulse. If the laser pulse has a length less than 1 ps we expect THz emission as the emitted electric field is the second derivative of the polarization.

$$E_{THz} \propto \frac{\partial^2 P_2}{\partial t^2} \tag{1.4}$$

For THz emission from non-linear crystals the orientation and length of the crystal play an important role. The dielectric tensor that determines the value of $\chi^{(2)}$ is different along different axis and thus the correct cut needs to be chosen carefully. As second order non-linear crystals must be non centrosymmetric they are typically birefringent. Many materials used for THz generation such as ZnTe and CdTe are zincblende structures with a point group symmetry of $\bar{4}$3m which is isotropic around any axis and thus not birefringent. Due to different refractive indices the THz radiation and optical pulse will spatially walk-off due to a group-phase velocity missmatch as they propagate through the non-linear crystal. As this happens the generated THz emission will destructively interfere due to phase mismatching making the crystal only useful for certain lengths. This means that shorter crystals that are phase matched give higher bandwidths and shorter pulses than longer crystals where the group phase missmatch is larger but have lower output power.

1.5.3 Surface Emitters

Ultrafast generation of photo-carriers near the surface of a semiconductor produces picosecond lifetime surge currents that radiate a broadband THz pulse [49, 50, 51, 52, 53]. At low fluencies there are two different mechanisms identified as being responsible for surface emission. The first is surface field emission where carriers are accelerated by a surface field due to band bending. The other is the photo-Dember effect where a net diffusion current forms perpendicular to the surface due to the difference in diffusivity of electrons and holes and a break in symmetry at the surface. Both phenomena suffer from low out-coupling from the semiconductor device that lead to a decline in interest

owing to the high performance of photoconductive (PC) devices.
The electrostatic potential in a homogeneous semiconductor is uniform in the bulk but it changes in the region near the surface. Surface charges may form on the surface of a semiconductor due to impurities. Impurities may form from during growth by being captured by dangling bonds on the surface to complete the crystal or from oxidation when the sample is exposed to air. These surface charges create a depletion or accumulation region within the semiconductor to neutralise the surface charge. This space-charge region causes band bending near the surface creating an intrinsic electric field. Upon photo-excitation, photo-carriers generated within the space charge region are accelerated in this electric field, a simple schematic of this is shown in Fig. 1.5. The ultrafast generation, acceleration, and recombination of the photo-excited carriers

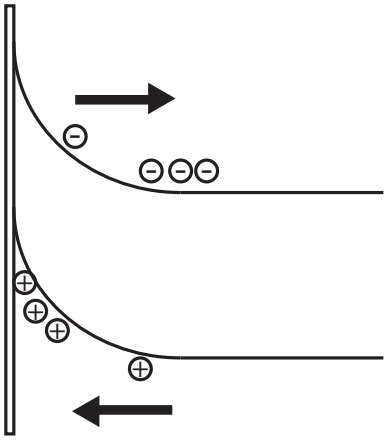

Figure 1.5: Schematic of band bending at the surface of a semiconductor and the acceleration of photo-excited carriers within the depletion region.

generates an ultrafast surge current perpendicular to the surface which emits THz radiation parallel to the surface. The sign of this emission depends on the direction of the surface field which can be flipped by changing the doping of the semiconductor. Complementing or sometimes competing with the surface field effect is another effect based on diffusion rather than drift called the photo-Dember effect. The photo-Dember effect also consists of the formation of a charge dipole in the vicinity of the semiconductor surface after ultrafast generation of carriers. The effect is a diffusion effect that arises form the differing carrier mobilities for electrons and holes in a semiconductor and a break in symmetry at the surface. As the band-gap of the semiconductor is matched with the energy of the laser wavelength the semiconductor is highly absorbing creating a strong carrier gradient perpendicular to the surface; the electrons and holes then diffuse. As the electrons have a higher mobility than the holes a dipole forms that is perpendicular to the surface, as shown in Fig. 1.6. It is the formation and destruction of this dipole that emits THz radiation that is also parallel to the surface.

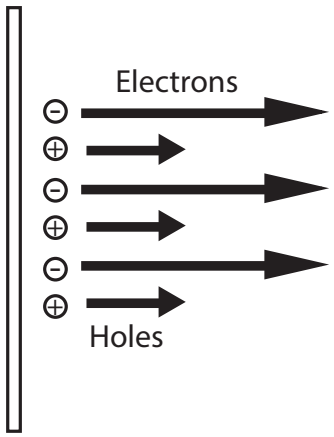

Figure 1.6: Illustration of the photo-Dember effect with a symmetric electron and hole distribution inside a semiconductor producing a dipole collinear to the laser beam and emitting perpendicular to it.

The emission from surface effects is parallel to the surface making it hard to outcouple from the device. By rotating the semiconductor so the laser beam is oriented at 45° to the surface gives a component that radiates parallel to the laser [52], but most of the emission is not outcoupled from the semiconductor device. Another way of enhancing this emission is by using external magnetic fields to rotate the dipole, but this has proven to be impractical due to the applied magnetic field needed being in the order of several Tesla [50].

1.6 Detection of THz Pulses

1.6.1 Photoconductive Antenna

PCAs similar to the ones used as emitters can be used for the detection of THz radiation. In principle the photoconductive detection is the reverse of the generation method. For the detector the antenna is unbiased and upon illumination from the laser pulse photo-carriers are generated which are then accelerated by the incident THz electric field. This current is measured across the antenna gap and is proportional to the strength of the THz electric field. Because the carrier lifetime and laser pulse length is much shorter than the length of the THz pulse the carrier effectively sees the THz electric field as a stationary DC field. As the delay or emitter arm changes path length the detector is gated at different points along the THz pulse allowing for its electric field to be mapped out. The time dependent current created by accelerating the photo-carriers in the device by the THz electric field is the convolution of the THz electric field with

the time dependent conductivity of the detector [47].

$$j(t) = \frac{1}{T}\int_0^T E_{THz}(\tau)\sigma(t-\tau)dt \tag{1.5}$$

where T is the laser repetition rate, E_{THz} is the incident THz electric field, and σ is the conductivity of the detector.

1.6.2 Electro Optical Detector

Nonlinear crystals can also be used for detection. This detection scheme is based on another second order nonlinear effect called the Pockels effect, or the linear electro optical effect, where an external DC field induces a birefringence within the crystal. When the THz radiation is incident on the nonlinear crystal propagating along the principle axis it induces a birefringence where both the ordinary and extra-ordinary refractive indices vary linearly with the electric field. Figure 1.7 shows a schematic of a nonlinear THz detector. The probe beam is passed colinearly with the THz pulse. Due to the birefringence this leads to a change in its polarisation going from linear to elliptical. Using a quarter wave plate, polarising beam splitter, and a pair of balanced photo-diodes the change in polarisation can be measured. Again by changing the delay

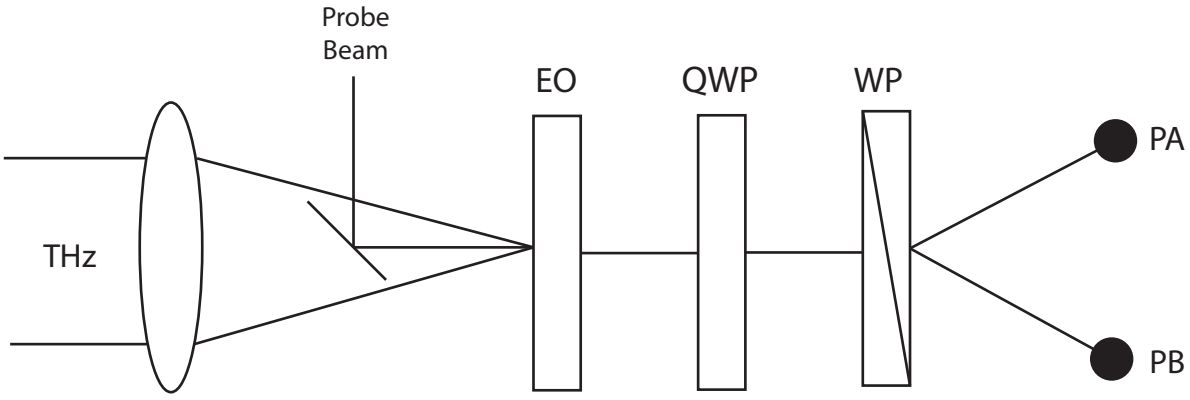

Figure 1.7: Nonlinear electro-optical sampler for mapping THz radiation in a THz-TDS. EO is the nonlinear electo-optical crystal, QWP is a quater wave plate, WP is a wollaston prism, and PA and PB are a pair of balanced photo-diodes

line it is possible to map out the THz electric field.

1.7 Lateral photo-Dember effect

In 2010 Klatt et al. developed a novel method for generating THz radiation from lateral photo-Dember currents [54]. To do this they rotated the distribution of the carrier concentration by 90° so that the dipole is parallel to the surface and thus emitting perpendicular to it; this method can also allow for custom carrier gradients. They achieved this rotation of the geometry by partially masking a semiconductor surface with a deposited metal mask as shown in Fig. 1.8. The spot of an ultrafast band-gap-matched laser is focused half on the metallic mask and half on the semiconductor surface. This generates an asymmetrical distribution of photo-generated carriers near the metal-semiconductor interface that are free to diffuse. Such a device gives intense

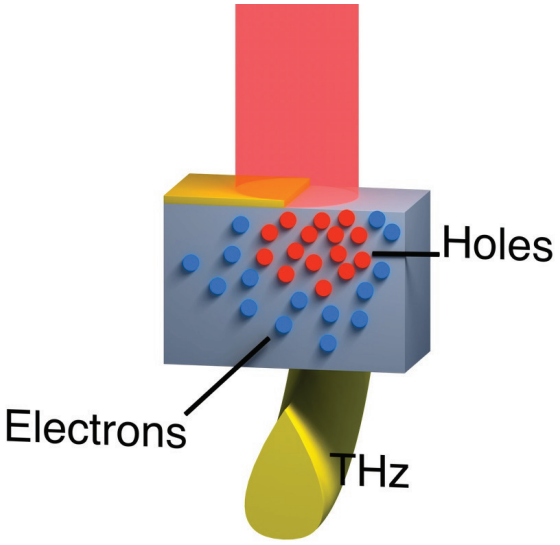

Figure 1.8: A schematic showing the geometry of an LPD emitter; a semiconductor surface partially masked by a deposited metal layer, where an ultralfast band-gap matched laser is focused half on the metallic mask and half on the semiconductor surface creates a distribution of photo-generated carriers near the metal-semiconductor interface that radiate in the same direction as the optical excitation.

THz emission as observed in [1, 55, 56, 57]. They attribute this to an asymmetrical diffusion current because of the initial asymmetrical carrier distribution. The argument is that because the carrier population is steeper at the interface there must be a greater diffusion current moving towards and under the metal mask than that going away from it leading to a net diffusion current. Although the signal from one strip is about 6 times smaller than that of a PC antenna it is possible, with some careful design, to make

a series of antennas which contribute constructively to a single emission. Klatt et al. have demonstrated that by using a multiplex PD antenna design to enhance the THz emission they can reach the same power as PC antenna and potentially beyond [55]. Their multiplex antenna consisted of an array of wedge shaped striplines, as shown in Fig. 1.9, spaced at 3 μm with a width of 2 μm.

One issue with this antenna design is that the fabrication method is not trivial as

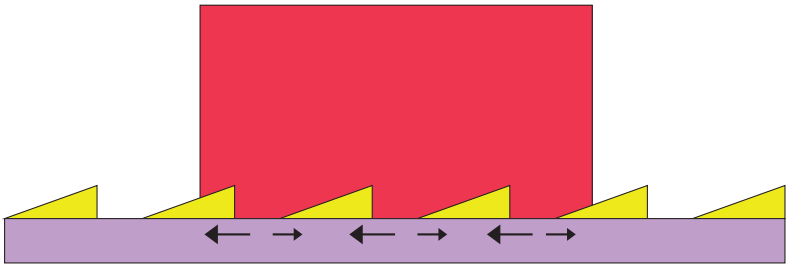

Figure 1.9: Klatt et al. multiplex of wedge photo-Dember antenna

it requires creating a 3D structure of varying thickness. Based on this principle we envisaged and fabricated an array of emitters in [58] with the aim of improving the ease of fabrication and performance. An SEM image of one of these emitters is shown in Fig. 1.10. The design consisted of an array of striplines where one edge was straight while the other edge was made up of thin triangular structures. The idea was that

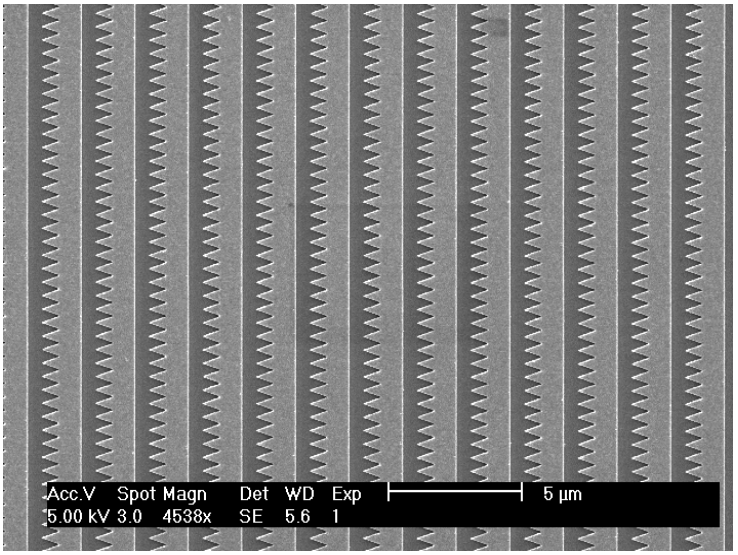

Figure 1.10: 2D multiplex emitter based on the principle given in [1]

on the sides with the triangles the electrons diffuse into the same area from different directions such that an asymmetric electron concentration is created. This breaks the symmetry of the system thus allowing for a net diffusion current across the antenna. I mounted these antennas and tried to generate THz with them in a typical THz-TDS

system, but no measurable THz signal was detected [58]. The structure did generate THz if I only illuminated the edge of the structure just as expected if it were a single gold sheet. This result conflicted with the understanding of the lateral PD effect, as outlined in [1] and that their emitters do produce measurable signals.
To understand these results 1D simulations of the situation with numerical solutions of the drift diffusion equation and Monte Carlo simulations were investigated. Both models take into account generation, drift, diffusion, and recombination of carrier concentrations within a semiconductor. The details of these simulations are described in Chapter 2. The resulting net current from these simulations with the geometry used by [1] or [58] was zero and thus do not predict THz emission. Yet experimentally I was able to generate THz emission from a single stripline PD emitter. With this contradiction in mind I came to realise that the observed THz emission cannot be explained by diffusion alone due to some simple arguments that are presented later.
Theoretical discussions following the realisation of this paradox lead to the development of a new theory of the mechanism involved. This new theory is that the dipole that forms under the metal mask is suppressed thus creating the anisotropy needed for net current. This mechanism explains why a net dipole radiates in the geometry of the lateral PD effect.
Figure 1.11 shows a simple illustration of this mechanism. The emission from the dipole

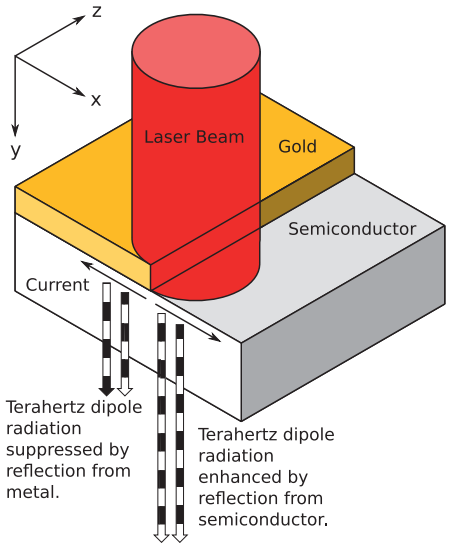

Figure 1.11: Illustration of the PD effect showing the coordinate system used.

that forms under the metal experiences destructive interference from a reflected wave off the metal mask because after reflection it experiences a π phase shift suppressing the dipole [59]. The dipole that forms not under the metal mask however is free to radiate and the source of the detected THz emission. This suppression mechanism is discussed further in Chapter 3.

The explanation given by Klatt et al. was intuitive and they never attempted to give a full theoretical description of the mechanism. Their interpretation however predicted an opposite sign of the THz emission than mine making it easy to test. PD stripline emitters were fabricated on semi-insulating (SI) and low temperature (LT) grown GaAs substrates and the polarity of the THz generated was measured. The results were found to be consistent with new hypothesis and contradicting that of Klatt et al. [60]. This mechanism indicates a novel method of generating THz radiation that is based on the diffusion current created by ultrafast radiation but also uses the inhibition of radiation due to a metal surface. These results are shown and discussed in Chapter 4.
The mechanism involved in LPD emitters was further investigated both theoretically and experimentally. Using our experimental apparatus the THz emission was measured from a LPD emitter with two gold layers deposited on a LT-GaAs substrate with an applied variable bias. Further, by measuring the THz emission as a function of an applied external electric field it was found to be in good agreement with the computer models. Emission dependency on spot position was also measured observing the expected sign dependency of the THz pulse electric field. In another experiment different asymmetrical carrier concentrations were generated away from the gold layers by shadow masking the laser beam with a knife edge. This demonstrated that regardless of the spot shape the sign and form of the emitted THz electric field does not change. Fluence dependency of THz emission from annealed, unanneald LT-GaAs and semi-insulating (SI) GaAs samples were performed to find the optimum parameters of illumination and saturation fluence.
With this new mechanism in mind two types of multiplex emitter designs were designed that were simpler to fabricate than that of Klatt et al. These two new multiplex emitters were fabricated on different substrates and tested. Our measurements of these emitters has shown them to be comparable with commercial PC emitters in terms of both power and bandwidth while being more durable.

1.8 Thesis Outline

The work presented in this thesis aims to describe, simulate, and show experimental evidence of a new mechanism for the generation of broad-band, coherent single cycle pulses of THz radiation for use in THz-TDS.
In Chapter 2, numerical and Monte Carlo models of the carrier dynamics of asymmetrically generated photo-carrier densities are investigated . The details of the theory behind the simulations is present as well as results from the modelling. These results led to insight into the mechanism involved.

In Chapter 3, metal mask dipole suppression is explored theoretically. An exact analytical solution to the diffraction problem of an emitting dipole in the vicinity of a semi-infinite perfect conductor is given. Using results from the numerical model in Chapter 2 with a finite element model the importance of the metal mask used for these devices is shown. Using results from the numerical model in Chapter 2 with a finite element model the importance of the metal mask used for these devices is shown.
In Chapter 4, a number of experiments are shown that validate that diffusion alone cannot account for the observed emission. First the polarity of the emitting dipole is detected and found to be in agreement with the dipole suppression interpretation. An external field is then placed across the LPD device and the emission is measured showing how it is affected by the electric field and how the emission depends on the spot shape and proximity to the metal mask. To eliminate any contribution from drift currents due to band bending near the metal:semiconductor interface an insulated metal contact on a semiconductor was fabricated and showed that it does not hinder the signal or bandwidth from these devices. Finally the spot size, pump fluence, and material properties are explored for annealed, unanneal LT-GaAs and SI-GaAs.
In Chapter 5, two multiplex LPD emitters are presented and the mechanism of how they are expected to work is described. These emitters are fabricated on different semiconductor substrates and tested. The results of these early studies find that these emitters are comparable to state of the art PC emitter in both power and bandwidth. They are also more durable and simpler to fabricate. The results of these early studies find that these emitters are comparable to state of the art PC emitter in both power and bandwidth. Other advantages are that they are more durable and simpler to fabricate.
Finally, Chapter 6 is a summary and conclusion of the work presented in this thesis.

Chapter 2

Theory and modelling of the lateral photo-Dember effect

2.1 Introduction

The lateral photo-Dember (LPD) effect is a mechanism for generating coherent pulses of THz radiation after ultrafast illumination of a bad-gap-matched semiconductor device that is partially masked by a metal contact. These devices were first demonstrated by Klatt et. al. [1] where they attribute the emitted THz radiation from a none zero lateral diffusion current that forms near the surface due an initially asymmetrical carrier concentration. To further investigate this effect I developed a numerical and Monte Carlo simulations to simulate the situation. I found that these models did not predict THz emission by only taking drift and diffusion into account. In this thesis I present an alternative explanation for the origin of the THz emission from lateral diffusion currents with the addition of dipole suppression. The explanation presented here argues that due to dipole suppression a dipole populations forming under the metal mask region is not free to emit. Where as the dipole population not under the metal mask is free to radiate emitting THz radiation perpendicular to the surface of the device. In these models I present the result for the emission across the entire simulation space and the result if only the dipoles away from the metal mask are taken into account.

2.2 Numerical drift-diffusion

A 1D model was used to simulate the carrier dynamics similar to the one in [51, 61]. The model simulates the evolution of carriers in a 1D semiconductor taking into account carrier generation, recombination, and drift-diffusion currents.
Carriers were generated in the model within a 1D space for arbitrary concentration distributions in both space and time. For each time step in the simulation the carriers are free to drift and diffuse depending on the carrier gradient, their diffusivity, mobility, and the local electric field. Carriers may also recombine or be trapped by defects.
The microscopic carrier current is a result of the electric field and diffusion current. For the electrons this is given by,

$$j_e = \mu_e e E n_e + e D_e \frac{\partial n_e}{\partial x} \tag{2.1}$$

where e is the change of an electron, n_e is the electron density, E is the electric field. The mobility, μ_e, and the diffusion coefficient, D_e, follow the Einstein relation assuming quasi-thermal equilibrium.

$$D_i = \frac{\mu_i k_b T_i}{e} \tag{2.2}$$

Where k_B is Boltzmann's constant and T_i is the carrier temperature.
Conservation of charge in Equation 2.1 leads to the equation describing the evolution of the carrier density, including both electric field and diffusion terms, for the electrons and holes is

$$\frac{\partial n_{e,h}}{\partial t} = \frac{1}{e}\frac{\partial j_{e,h}}{\partial x} - b\left(n_e n_h\right) - \frac{n_{e,h}}{\tau_1} + G(x,t) \tag{2.3}$$

Where $G\left(x,t\right)$ is the optical generation term, determined by the laser spot shape, size, and length. b is the bimolecular recombination constant for carrier-carrier recombination and τ_1 is carrier density lifetime due recombination via fast traps. The remaining equation for the model is Gauss's law,

$$\epsilon_0 \frac{\partial E}{\partial x} = \left(n_e - n_h\right) e \tag{2.4}$$

Eliminating the current j in Equation 2.3 gives the equation describing the evolution of the electron density. This includes both drfit and diffusion in both time and space.

$$\frac{\partial n_e}{\partial t} = \mu \frac{\partial}{\partial x}(n_e E) + D \frac{\partial^2 n_e}{\partial x^2} - b\left(n_e n_h\right) - \frac{n_e}{\tau_1} + G(x,t) \tag{2.5}$$

The evolution of this equation was calculated with a Python script. In the model, space was quantised with a mesh size of 10 nm and the simulation was incremented

T_e	3000 K
T_h	300 K
b	20×10^6 cm/s
τ_1	200 fs
μ_e	8500 $\text{cm}^2 V^{-1}\text{s}^{-1}$
μ_h	400 $\text{cm}^2 V^{-1}\text{s}^{-1}$

Table 2.1: Table of properties for LT-GaAs for numerical drift-diffusion model

through time steps of 1 fs. At each step in the simulation first the electric field is calculated by calculating the Coulomb potential for each mesh cell and taking its derivative. The change in carrier concentration for each mesh element is then caluclated using Equation 2.5 and the simulation is updated for the next iteration. The resulting current and carrier densities for electrons and holes was recoded during the simulation and saved. During this investigation we used the material properties of LT-GaAs. [51, 61, 62, 63, 64] as shown in Table 2.1.

Figure 2.1 shows the carrier concentration for electrons and holes 2 ps after photo-excitation for a symmetrical-Gaussian spot with a pulse length of 100 fs and a radius of 30 μm. The separation of charge in this figure is hard to see because of the large restoring fields that forms with the separation of charge that tries to bring the situation back to neutrality. Also the diffusion within a few picoseconds is short and the gradients are gradual.

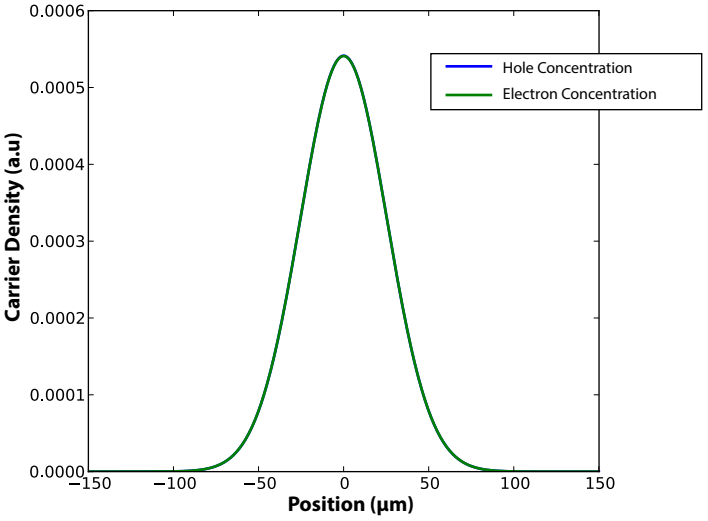

Figure 2.1: Electron and hole carrier concentration 2 ps after symmetrical photo-excitation

Figure 2.2 shows the carrier concentration for electrons and holes 2 ps after photo-excitation for an asymmetrical-Gaussian spot with the same optical and material properties as before. The interface has a gradual cut off as just cutting the Gaussian leads to the numerical differentiation in the model to return infinities. The asymmetrical-Gaussian is the same as the symmetrical situation for the shallow side where as the steep side has a sigma value that is 1/30 of the shallow side. The insert shows a mag-

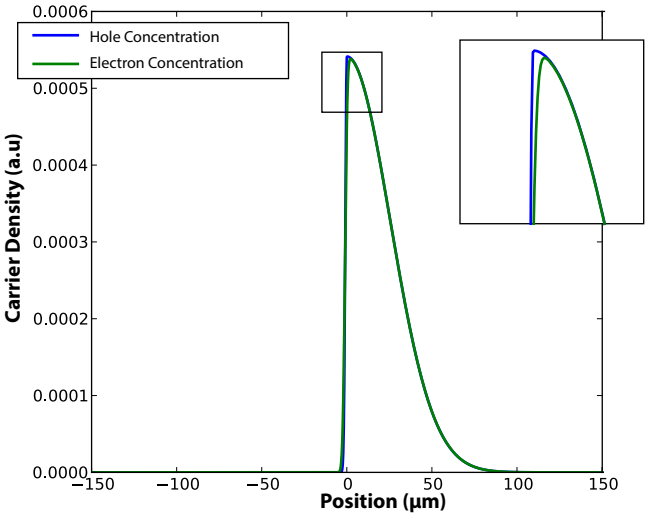

Figure 2.2: Electron and hole carrier concentration 2 ps after asymmetrical photo-excitation

nification of the peak region where the effect of carrier separation is most pronounced. To highlight the charge separation, Fig. 2.3 shows the charge density for both situations with the symmetrical situation magnified by 100. The symmetrical situation shows a symmetrical net charge density as expected because the carrier distribution is symmetrical. In both situations the charge summed over the entire area is zero because the the number of electrons and holes is equal. Further the centre of charge in both situations is at 0 once there is a separation of charge. The centre of charge remains static during the entire simulation regardless of the asymmetry of the carrier concentration. Also during the simulation the centre of charge for both electrons and holes is identical and remains stationary from generation to complete recombination of photo-carriers. To further illustrate this a magnification of the concentration near the interface is shown in Fig. 2.4 for the asymmetrical situation, the centre of charge is shown as a vertical line. This large charge separation at the interface and its ultrafast generation and destruction generates symmetrical currents perpendicular to the surface.

Fig. 2.5 shows the resulting current density for the asymmetrical carrier generation situation, as expected at any point in time during the simulation the total current is

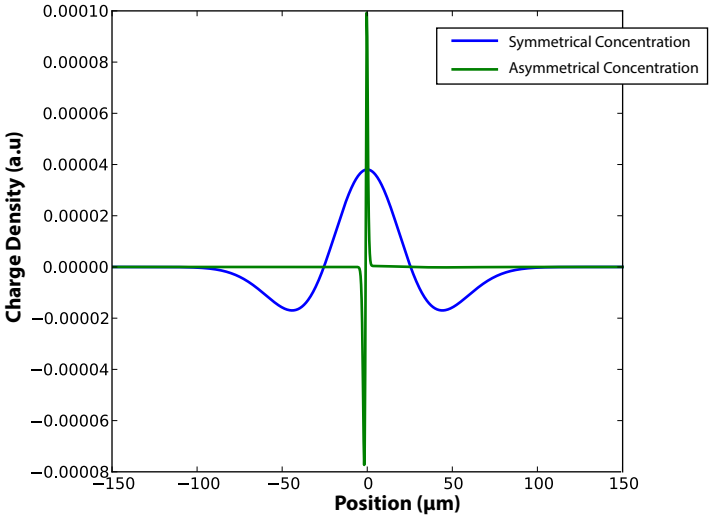

Figure 2.3: Charge density 2 ps after photo-excitation for both symmetrical and asymmetrical spots

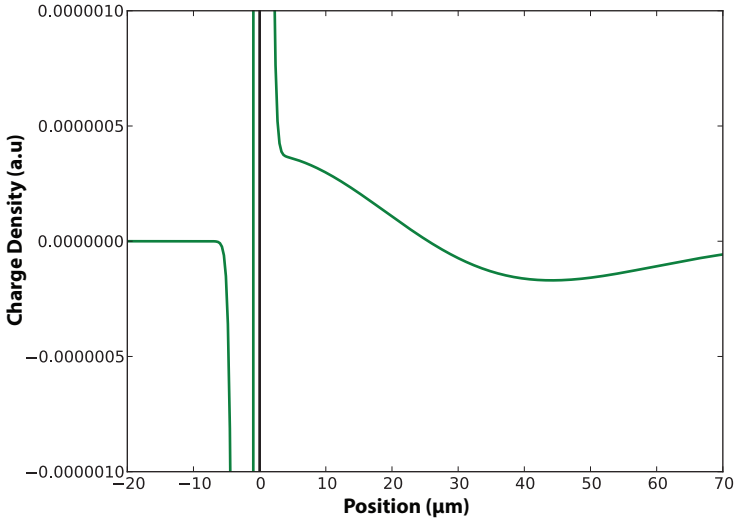

Figure 2.4: Close up of the charge density near the interface for the asymmetrical situation, the vertical black line is the calculated centre of charge that never moves away from 0

zero.

Figure 2.6 shows the net current summed over the entire simulation and the net current only summing microscopic current not under the metal mask. As can be seen the total current across the entire simulation is zero at all points. If only the current in the region free to emit is take into account we see the ultrafast generation and destruction

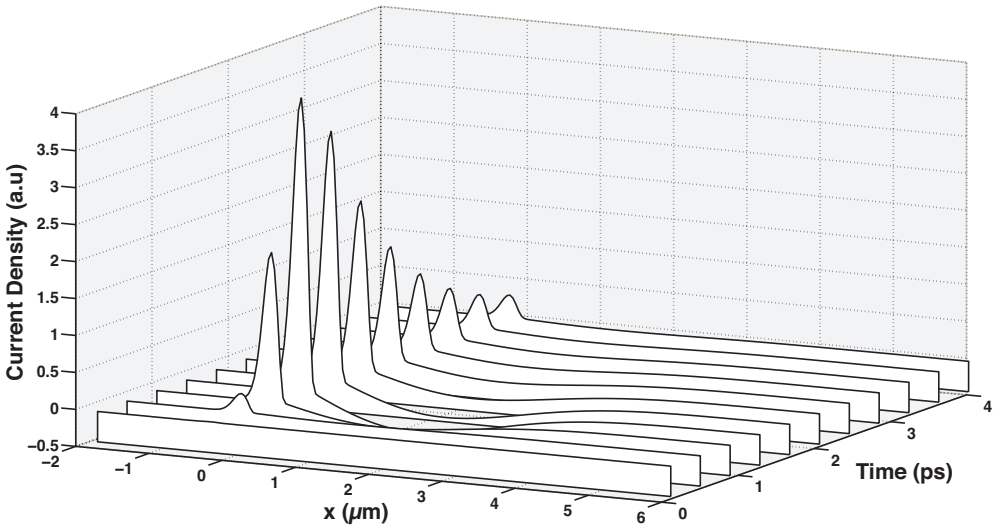

Figure 2.5: Calculated current density from the drift-diffusion equation for asymmetrical carrier excitation at metal-semiconductor interface at $x = 0$, no carriers are excited within negative region.

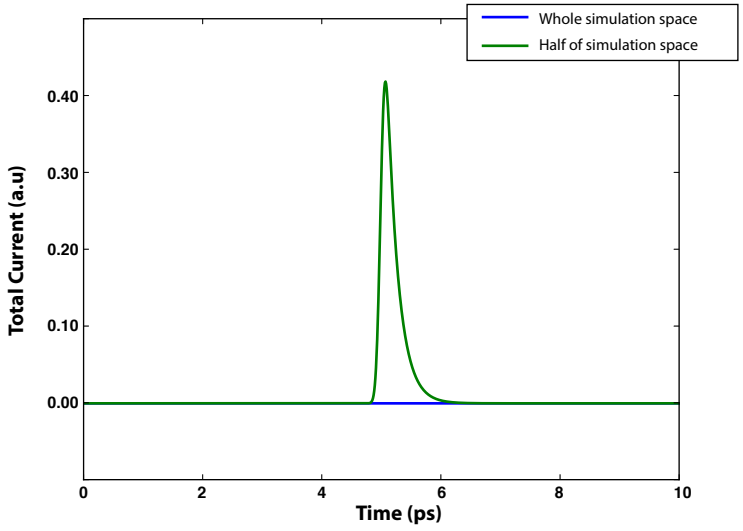

Figure 2.6: Total current as a function of time, the blue line is the total for the entire simulation and the green is the current only talking into account the concentration not under the metal mask.

of non-zero current within the picosecond time frame and therefore leads to THz emission.

By taking the derivative of these currents we get the THz emission. This result is shown in Fig. 2.7. This emission is much faster than what is experimentally measured as it

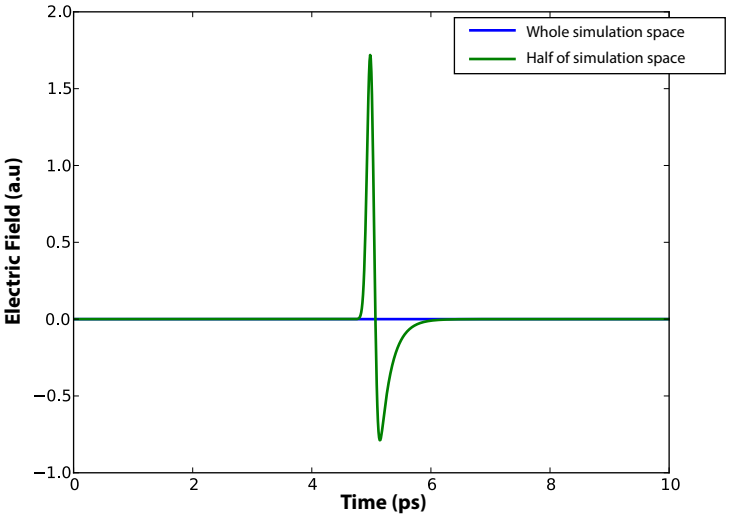

Figure 2.7: Predicted THz Emission, the blue line is whats predicted when taking the entire simulation and the green is what is expect when only the carrier not under the metal mask are taken into account.

has not been convoluted with the detector or experienced dispersion while travelling through the antennas and THz optics.

2.3 Monte Carlo

In semiconductors transport is dominated by random scattering events such as from impurities, carrier-carrier scattering, lattice vibrations etc. These scattering events randomise the energy and momentum of the scattered carrier. This means carrier transport is inherently stochastic and therefore Monte Carlo methods are useful for simulating carrier dynamics.

Alongside the numerical model of the drift-diffusion equation detailed above I developed and investigated the situation using a 1D Monte Carlo simulation (MCS). Ensemble Monte Carlo techniques can be used to simulate nonequilibrium transport for carriers in semiconductor devices [65, 66]. In the MCS algorithm the carrier transport of each particle is simulated as free particle motion after an instantaneous scattering event. Following the algorithm described in [67, 68], after each scattering event for each particle the momentum and energy of the scattered particle is changed and the time till the next scattering event is calculated (free-flight time).

To calculate the free-flight time for each particle the probability density, $P(t)$ needs to be known where $P(t)dt$ is the probability the particle reach time t with out scattering

from time $t = 0$ and have a scattering event in a time interval dt around time t. The latter probability may be written as $\Gamma[\mathbf{k}(t)]\,dt$, where $\Gamma[\mathbf{k}(t)]$ is the sum of all the scattering rates of a particle with wavevector $\mathbf{k}$.
As the probability of scattering in the interval of dt around t is $e^{-\int_0^t \Gamma[\mathbf{k}(t')]dt'}$, the probability $P(t)\,dt$ is

$$P(t)\,dt = \Gamma[\mathbf{k}(t)]\,e^{-\int_0^t \Gamma[\mathbf{k}(t')]dt'}dt \tag{2.6}$$

To generate random flight times according to this probability a random number, r with a uniform distribution between 0, and 1 is generated such that

$$r = \int_0^{t_f} P(t)\,dt \tag{2.7}$$

where t_f is the time of flight.
Integrating this yields

$$-\ln r = \int_0^{t_f} \Gamma\left[\mathbf{k}\left(t'\right)\right] dt' \tag{2.8}$$

To simplify we can introduce a fictitious scattering term called self-scattering to ensure that Γ is constant with time. The concept is that the self-scattering mechanism scatters the particle in such a way that the momentum and energy of the particle are unchanged, i.e it has not scattered at all. The probability of self-scattering adjusts itself so that the total scattering rate Γ is constant with time and $\mathbf{k}$. With this simplification it is trivial to find the random flight time

$$t_f = -\frac{1}{\Gamma}\ln r \tag{2.9}$$

The constant Γ was chosen at the start of the simulation such that Γ without self-scattering does not exceed it. To determine which scattering event happens for each carrier in the simulation we generate a random number, r_s which has a uniform distributions from 0 to 1. This random number is then multiplied with Γ and compared with relative total scattering events. An example of this is shown in Fig. 2.8.

Once the scattering mechanism is chosen the final $\mathbf{k}$ is calculated from the initial wavevector for that particle. For static fields the evolution of $\mathbf{k}$ is given by

$$\mathbf{k}(t) = \mathbf{k}(0) - \frac{e\mathbf{E}t}{\hbar} \tag{2.10}$$

where e is the charge of an electron and $\mathbf{E}$ is the electric field.
During the simulation the carriers propagate as free carriers within an electric field by calculating the drift. The carriers are then interrupted by scattering events which may change their energy and momentum before they continue to propagate freely.
The electric field used for drift is calculated by solving Poisson's equation the same

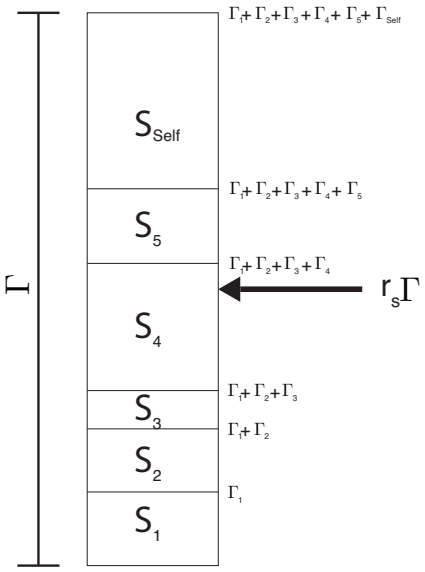

Figure 2.8: Random scattering mechanism selection using random number r, here the number is pointing to scattering mechanism S_4

way as it was in the numerical model, however in this MCS the carriers are not fixed to a grid but exist in continuous space. To solve Poisson's equation we have to generate a mesh and distribute our charges onto grid points by mapping each particle to the nearest grid point as a density. In my simulation I chose a mesh cell size of 10 nm. For simplicity the semiconductor band structure was assumed to be parabolic and only included the Γ valley. For parabolic bands the relationship between E and k is

$$E = \frac{\hbar^2 k^2}{2m^*} \tag{2.11}$$

where m^* is the effective mass of the carrier. A diagram of the band structure is shown in Fig. 2.9 using typical values for the effective mass of electrons and holes and band-gap energy for GaAs as given in Table 2.2. Using parabolic bands, terms for velocity and acceleration are easily found to be

$$\mathbf{v} = \frac{\hbar \mathbf{k}}{m^*}, \ \mathbf{a} = \frac{\hbar}{m^*} \frac{d\mathbf{k}}{dt} \tag{2.12}$$

When the simulation is initialised a pool of carriers is created that will be moved into the simulation as time progresses. The carriers are generated randomly so that they have a half Gaussian profile along the x direction with a width of 1 μm and a full Gaussian distribution in time with a FWHM of $\tau = 10$ fs. An example of this distribution for 1000 carriers is shown in Fig. 2.10. The carriers are also given an initial $\mathbf{k_x}$ with equal probability of pointing in the x or $-x$ direction. Gaussian broadening of the photon

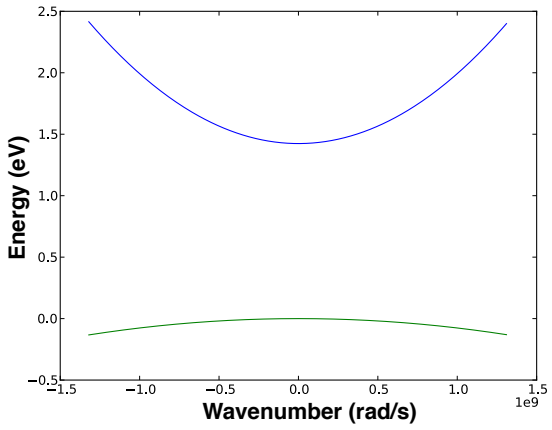

Figure 2.9: Parabolic band structure of GaAs

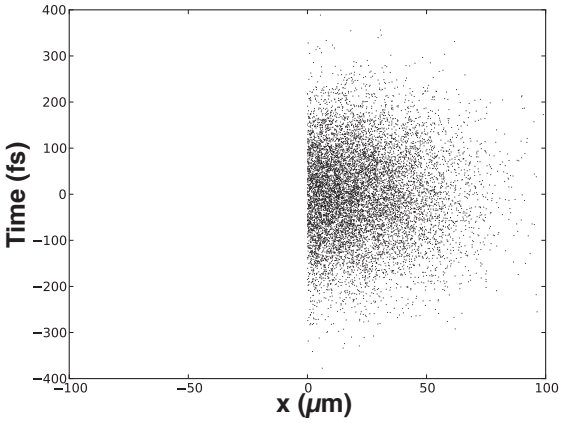

Figure 2.10: Location of carriers in x and t

energies from the pump laser was estimated to have a FWHM of [69]

$$E_f = 4\ln(2)\frac{\hbar}{\tau} \tag{2.13}$$

Where τ is the width of the laser pulse. The magnitude of $\mathbf{k}$ is given by the initial energy of the electron-hole pairs which is the difference between the semiconductor band gap and the photon energy. This energy was partitioned between electrons and holes such that momentum was conserved. The relationship for initial $\mathbf{k}$ values to the difference between the band-gap and photon energy is,

$$k_{init} = \frac{\sqrt{2\mu\Delta E}}{\hbar} \tag{2.14}$$

where μ is the reduced mass of electrons and holes and ΔE is the difference between the band-gap and photon energies. During the simulation the simulation time is checked against the initialisation time of each carrier in the pool. If the simulation time is greater than the initialisation time of the carrier then it is added into the simulation and propagated from its initialisation time to the current simulation time.
The simulation takes into account four scattering events, self scattering, optical-phonon scattering, defect scattering, and trap-carrier recombination. Expressions for carrier scattering were taken from [50, 65, 66]. The expression for optical-phonon scattering for both absorption and emission is,

$$W_p(k) = \frac{m^* \omega_0 q_e^2}{4\pi\epsilon_p \hbar^2 k} \left(f_B(\hbar\omega_0) + \frac{1}{2} \mp \frac{1}{2} \right) \ln \frac{k_{max}}{k_{min}} \tag{2.15}$$

where

$$\begin{aligned} k_{max} &= k \left| 1 + \sqrt{1 \pm \frac{\hbar\omega_0}{E_k}} \right| \\ k_{min} &= k \left| 1 - \sqrt{1 \pm \frac{\hbar\omega_0}{E_k}} \right| \end{aligned} \tag{2.16}$$

Here ω_0 is the angular frequency of the phonon, $1/\epsilon_p = 1/\epsilon_\infty - 1/\epsilon_0$ where ϵ_∞ and ϵ_0 are the high and low frequency limit of the materials permittivity, and $f_B(\hbar\omega_0)$ is the Bose-Einstein distribution. For absorption, the equation uses the top operator of the 'plus or minus' symbols, and for emission it uses the bottom. After scattering the energy of the carrier is either increased or decreased by $\hbar\omega_0$ depending if it absorbed or emitted the phonon.
The expression of defect scattering is,

$$W_{defect}(k) = \frac{2nq^4 k m^*}{\pi\hbar^3 \epsilon_0 \epsilon_r} \frac{1}{\lambda^2 \left(\lambda^2 + 4k^2\right)} \tag{2.17}$$

where n is the impurity density and λ is the inverse of the Debye length. Defect scattering is elastic and thus the energy of the carrier after scattering is unchanged. For carrier recombination I used the trap recombination rate, τ, for LT-GaAs. These scattering rates are shown in Fig. 2.11 as a function of energy in eV.
The model was ran for a half Gaussian spot with a HWFM width of 1 μm and a pulse length of 10 fs for 10^6 electron-hole pairs. The material parameters used were taken from [50] and are shown in Table 2.2.
Figure 2.12 shows in (a) a flow chart of the main MCS procedure and in (b) details of the 'Free-Flight-Scatter procedure' which propagates and scatters each carrier in the simulation. The main MCS procedure first loads the material properties and simulation

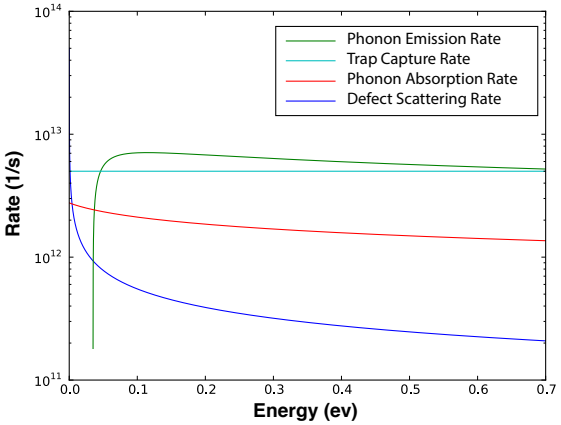

Figure 2.11: Scattering rates used in the Monte Carlo simulation as a function of energy

Hole effective mass, m_h	$0.5m_0$
Electron effective mass, m_h	$0.067m_0$
Band-gap energy	1.5 eV
LO-phonon energy, $\hbar\omega_0$	0.035 eV
Permittivity low frequency limit, ϵ_0	12.95
Permittivity high frequency limit, ϵ_∞	10.9
Defect density, n	10^{19} cm^{-3}
Trap recombination rate, τ	200 fs

Table 2.2: Table of properties for LT-GaAs used for the Monte Carlo simulation.

parameters. Carrier objects are created with randomised position x, creation time t_0, $\mathbf{k}$, and free-flight time t_f. The initial time of the simulation is selected to be when the first carrier will be added into the simulation space. The simulation then enters its main loop. First the electric field for the current state is calculated. Next carriers are added to the simulation from the carrier pool if t_0 is less than or equal to the current simulation time t. The 'Free-Flight-Scatter procedure' is then called for each carrier in the simulation space. Once all the carriers have been propagated and scattered the simulation time moves along by one step dt. The simulation ends when the simulation time reaches the maximum simulation time, t_{max}.

The 'Free-Flight-Scatter procedure', shown in Fig. 2.12(b). deals with the propagation and scattering of the carriers in the simulation space. The procedure is looped over all carriers in the simulation space each time step of the simulation. First Δt is set equal to the simulation time interval dt, this variable is used in this procedure to measure the time from a scatter event to the next simulation time step. If the flight time t_f

is less than the time interval (ie the carrier scatters this time step), then we enter the main loop, otherwise we skip the loop and drift the particle to the next time step and calculate its new value for **k**. In the loop, the carrier is propagated based on its **k** value and local electric field. Once propagated **k** is replaced with a new **k** due to acceleration from drift. The carrier is then scattered randomly by randomly choosing a scattering mechanism and changing its **k** value or tagging it as recombined. If tagged the carrier is removed from the simulation and the procedure is ran for the next carrier. Next, the time to the next time step is calculated and a new free flight time is generated. If the new free flight time is shorter than the time to the next time step, then the main loop is repeated until the next scattering event is later than the next time step or the carrier recombines. Once the main loop is exited the carrier is propagated to the next simulation time and the procedure is performed on the next carrier. Once all carriers have been propagated and scattered the procedure ends. The unoptimised Python script takes about 5 hours to complete a single run over 1 ps of simulation time for 10^6 electron hole pairs on a mid-range desktop computer.

In Fig. 2.13 I show the charge density during the simulation 20 fs after peak photo-excitation. The form of the charge density across space is similar to the charge density calculated from the numerical model shown in Fig. 2.3. As expected summing over all the microscopic currents, $\sum_i q_i \mathbf{v_i} = \mathbf{0}$ for all times, where q_i and $\mathbf{v_i}$ are the charge and velocity of each individual carrier. Becuase the emitted THz wave is the second derivative of the current, this shows that no THz emission is generated from an asymmetrical carrier concentration alone. To calculate the emission if the metal mask suppresses the dipoles forming under it requires a different approach. Complete suppression of the dipoles under the metal mask is assumed which in Chapter 3 I show is quite close to the theoretical expectation. Just summing the velocities of the particles not under the mask does not work because there is isotropic transport across the two regions. It is simpler to calculate the net dipole moment and then take its second derivative to get the THz emission. The resulting predicted emission for the entire simulation and only what is not under the metal mask is shown in Fig. 2.14. It can be seen in this figure that without the suppression of the dipoles under the metal mask no THz emission is expected where as if the suppression is taken into account THz emission is expected. As with the numerical model this model was unable to predict any THz emission from drift and diffusion alone. Similar results to this from Monte Carlo simulations can be seen in [50, 70] as well as the PhD thesis of Klatt [71]. The MCS presented by Klatt in his thesis does predict THz emission without taking into account dipole suppression which is somewhat surprising and in contradiction.

The script used for this simulation is not yet complete and needs to be optimised and expanded to 3 dimensions. It is possible to run all the functions in parallel except for the electric field solver speeding up the simulation. Unfortunately the function that is

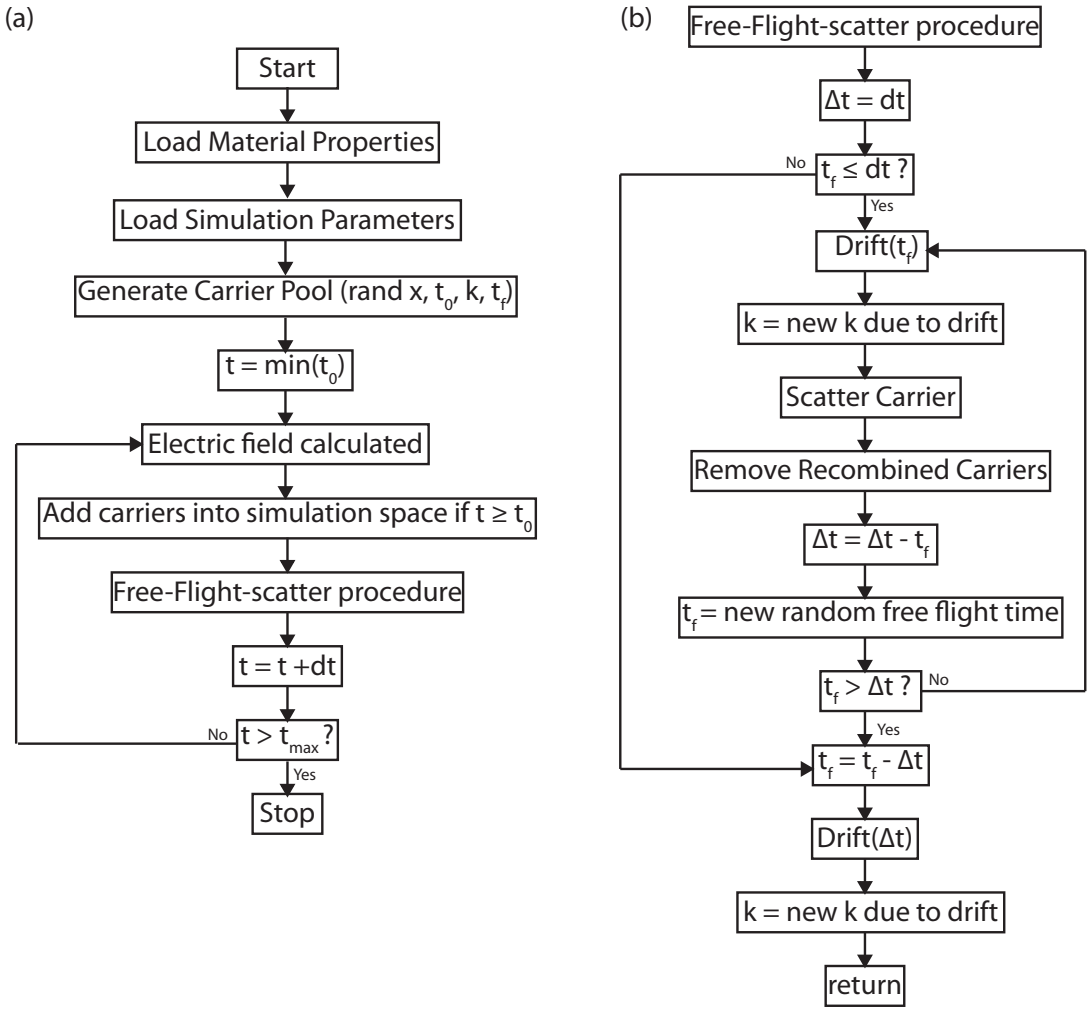

Figure 2.12: (a) Flow chart of the main loop of the MCS. (b) Flow chart of the free-flight and scattering procedure which is ran on each carrier in the simulation.

the most computationally expensive is the electric field solver. Thankfully there is a smarter way of solving the electric field by using a FFT method to solve the Poission equation which scales as $O\left(N \log_2\left(N\right)\right)$. The code can be sped up even further if it was written in a lower level programming language such as C.

2.4 Analytical

During the simulations it is not clear if drift or diffusion plays a greater role. To investigate this a ratio of the drift and diffusion components of the current can be found. In this section I will show that during the period of time it takes to generate

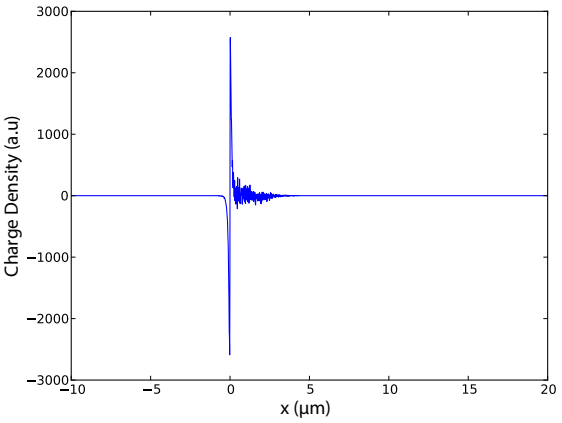

Figure 2.13: Charge density from the Monte Carlo simulation 20 fs after photo-excitation

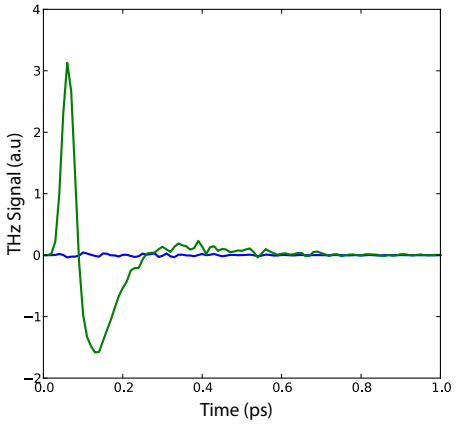

Figure 2.14: Predicted THz emission from the MCS, the blue line is the predicted emission for the entire simulation and the green line is the predicted emission when only dipoles that are not under the masked area are taken into account.

THz radiation the drift component of the drift-diffusion transport model is negligible. In general, the ratio between E-field and diffusion generated currents can be estimated to be $\sim r^2/\lambda^2$, where r is a typical length scale for the diffusion and λ is the Debye length.

2.4.1 Drift vs Diffusion

Microscopic current is the addition of the current at each point due to diffusion and the drift current giving

$$j = e\mu nE + eD\nabla n \tag{2.18}$$

To find which components gives the bigger contribution we find the ratio, R, between the two effects.

$$R = \frac{\mu nE}{D\nabla n} \tag{2.19}$$

Replacing D with the Einstein relation $D = \mu k_b T/e$ gives

$$R = \frac{eE}{k_b T}\frac{n}{\nabla n} \tag{2.20}$$

If we assume a charge density, ρ, and a fixed length, L, that represents the average diffusion distance during the time range we are interested in, then the largest E-field would be created by a sphere which has a volume, $V = (4/3)\pi L^3$,

$$E = \frac{\rho V}{4\pi\epsilon_0 L^2} = \frac{\rho L}{3\epsilon_0} \tag{2.21}$$

Where $\rho = ne$. Putting this back into Equation 2.20 gives.

$$R = \frac{e\rho L}{3k_b T\epsilon_0}\frac{n}{\nabla n} = \frac{1}{3}\frac{ne^2 L}{\epsilon_0 k_b T}\frac{n}{\nabla n} \tag{2.22}$$

The screening length (Debye length) of our system is given as

$$\lambda = \sqrt{\frac{\epsilon_0 k_b T}{ne^2}} \tag{2.23}$$

Substituting this into Equation 2.22 gives

$$R = \frac{1}{3\lambda^2 L^2}\frac{n}{\nabla n} \tag{2.24}$$

If n was plotted with respect to space in any direction there will be a point where $\nabla n = L/n$, giving

$$R = \frac{L^2}{3\lambda^2} \tag{2.25}$$

The importance of the E-field current is dependent on how the Debye length compares with the diffusion distance within the first few picoseconds. In our situation within only a few picoseconds the carriers have not diffused far. This means that $\lambda \gg L$ and

the diffusion term predominates. In fact if the drift component in my simulations is neglected no real difference in the result is observed.

2.5 Conclusion

The conclusion from the simulations is that diffusion alone cannot create a net total current even when starting with an asymmetric carrier concentration. This statement can also be supported with a theoretical argument. If the microscopic diffusion current is proportional to $\partial n_e/\partial x$, the total current due to diffusion is the definite integral $\int (\partial n_e/\partial x)\, dx$ integrating across the entire region of interest. As long as the initial concentration starts from zero and ends to zero this integral will be equal to zero.
Further in [72] they show that for a homogeneous semiconductor any carrier concentration, or recombination centre distribution across the semiconductor cannot lead to a current even if they take into account the electric field created by the separation of photo-carriers.
The theory proposed and investigated in this thesis is that any dipoles forming under the metal mask are suppressed because if allowed to emit they experience destructive interference from the reflected wave off the metal mask. When only the carriers not under the metal mask are taken into account in the simulations we do see an expected THz emission. In the next chapter I will investigate some theoretical analysis for dipole emission under a metal mask.

Chapter 3

Theory of dipole suppression

3.1 Introduction

In the previous chapter I demonstrated that diffusion alone cannot account for the observed THz emission from LPD emitters. To explain this inconsistency I proposed an alternative explanation which I support in this chapter with an analytical model and a finite element analysis model. First I will present an exact analytical model to the problem of the expected detected emission far away from a dipole source that is in the vicinity of a semi-infinite perfect conductor. The result of this model shows that a dipole located much less than a wavelength under a metal mask is heavily suppressed. Results from the numerical drift-diffusion model described in Chapter 2 for an asymmetrical carrier distribution are incorporate into a finite element analysis model of the geometry involved. When a metal mask was present the model does not predict any THz emission propagating perpendicular to the semiconductor device if the metal mask is missing with the same simulation data.

3.2 Analytical

When light is reflected at an interface between two different dielectric materials with refractive indices n_0 and n_1, as shown in Fig. 3.1. The amplitude of reflectance is expressed as the Fresnel equation,

$$\rho = \frac{E_R}{E_I} = \frac{n_0 - n_1}{n_0 + n_1} \tag{3.1}$$

Where E_R is the reflected electric field and E_I is the incident electric field. If n_0 is less

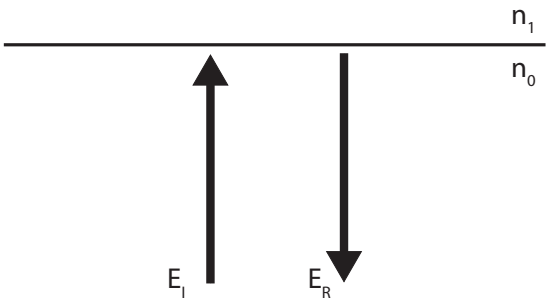

Figure 3.1: Reflection of light at normal incidence on a boundary of two media with different refractive indices.

than n_1, then ρ is negative representing a π phase shift. For a perfect conductor $E_R = -E_I$.

The suppression of radiation in LPD emitters happens due to the long wavelength of the THz radiation in relation to the distance between the dipole and metal. The radiation that is reflected by the surface of the metal acquires a π-phase shift in relation to the non-reflected radiation. Interference between the non-reflected and reflected radiation is destructive and causes the dipole under the metal to be suppressed, and no emission to be generated in the y direction [73, 74].

The problem can also be addressed using the argument made by K. H. Drexhage [75] by summing the number of radiative states of an oscillating dipole as it approaches a plane mirror. In [75] they give an expression for the intensity pattern for a radiating dipole with an emission polarised parallel to a mirror surface.

$$P(\theta) = 1 + \rho^2(\theta) + 2\rho(\theta)\cos\left[\frac{4\pi n d}{\lambda}\cos\theta - \delta(\theta)\right] \tag{3.2}$$

Where θ is the angle between the direction of light emission and the mirror normal, d is the distance to the dipole from the mirror surface, n is the refractive index of the material, λ is the wave length of the emitted light, ρ is the reflection coefficient, and δ is the phase shift on reflection. Figure 3.2 shows this equation plotted in free space with the dipole emitting at 1 THz positioned 1 μm and 675 μm from the surface of an ideal mirror. The emission from the dipole 1 μm from the surface was multiplied by 1000 for comparison. The proportion of the density of radiative states (DOS) for a dipole near the mirror, D_d, compared with the DOS when it is far away from the mirror, D_∞, can be found by integrating the total intensity above the mirror. Assuming a perfect conductor with a reflectivity of 100% for all angles, a phase shift of π on reflection, and the emission being polarised parallel to the surface. An expression is given by K. H. Drexhange as,

$$\frac{D_d}{D_\infty} = 1 - \frac{3\sin x}{2x} - \frac{3\cos x}{2x^2} + \frac{3\sin x}{2x^3} \tag{3.3}$$

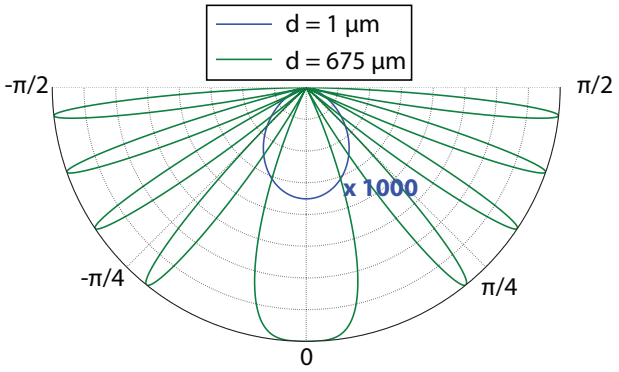

Figure 3.2: Emission pattern form a dipole 1 μm and 300 μm from the surface of a plane mirror. The plot for the 1 μm case has been multiplied by 1000 so it is visible.

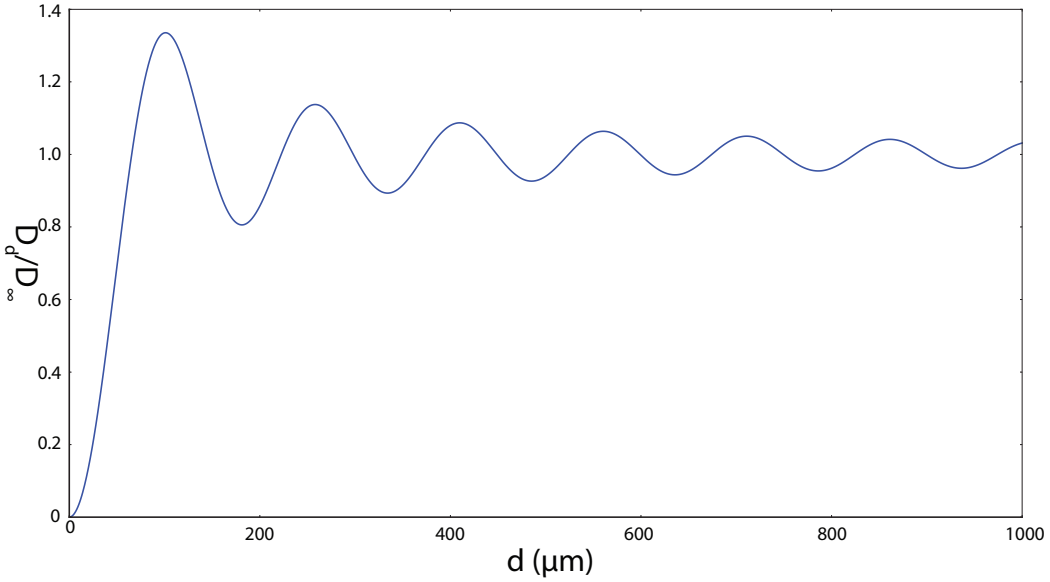

Figure 3.3: Relative density of radiative states (DOS) for dipole emission of 1 THz near the surface of an ideal mirror in comparison to the DOS for a dipole far from the mirror surface.

Where $x = \frac{4\pi nd}{\lambda}$. Figure 3.3 shows this equation plotted as a function of d in free space for a dipole emitting at 1 THz. As can be seen the DOS quickly reduces as the dipole approaches the mirror surface quenching the dipole.

The geometry of the LPD devices however is that of a metal edge and not an infinite sheet. For a more complete model of the problem edge effects must be taken into account. This can be done so by solving the Sommerfeld diffraction problem for a semi-infinite perfect conductor.

3.2.1 Dipole under a semi-infinite metallic mask

The problem of finding a rigorous solution to the diffraction problem of a plane wave incident on a infinitely thin, perfect conducting half-plane was solved in 1896 by Sommerfeld [76]. This solution was also the first exact solution to diffraction problems. Here the problem is similar but rather than measuring the electric field in the vicinity of the perfect conductor and empty space from a source far away I am interested in the opposite situation. Where the electric field is measured far away from a source near the perfect conductor interface.
The Sommerfield problem is tractable and can be used to study analytically the radiation of a dipole under a semi-infinite metallic surface. The problem is solved in free space and in only 2 dimensions. Fig. 3.4 shows a schematic of the problem where a perfectly conducting plane sits in the y plane from $-\infty$ to 0 at $x = 0$. The dipole S is oscillating in the y direction and is positioned at the polar coordinate (r_0, ϕ_0). And P is the position where the electric field is measured with the coordinate (r, ϕ). The

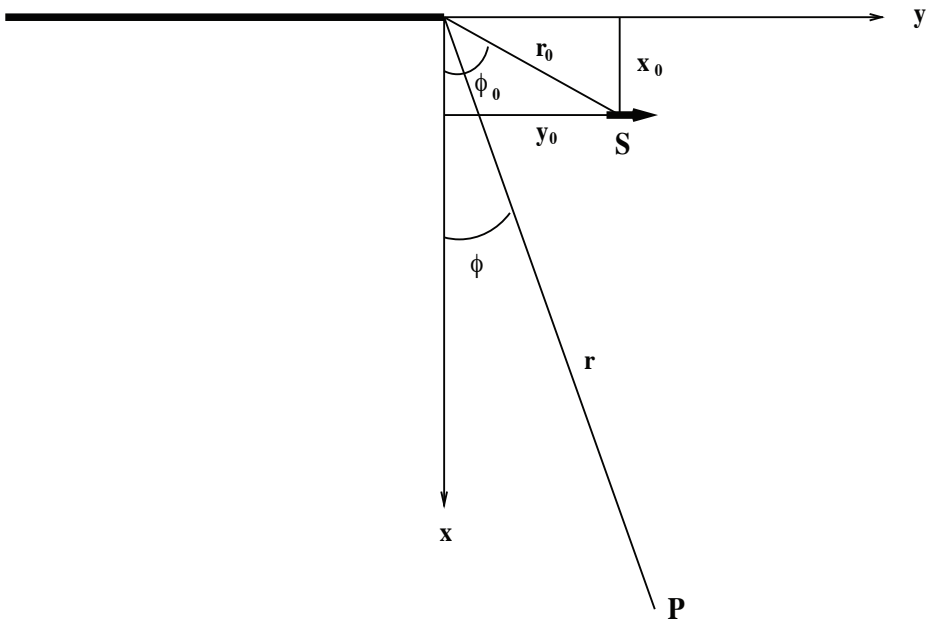

Figure 3.4: Schematic of the problem

current density in the source shown at S is $j_y = \partial(x - x_0)\partial(y - y_0)$ which in free space will produce a field with vector potential $A_i \propto H_0(kR)$ where $R^2 = (x-x_0)^2+(y-y_0)^2$ and H_0 denotes a Hankel function for a cylindrical wave. Along the conducting surface the electric fields must cancel out. This implies that the E field we are looking for in polar coordinates is

$$E_y \propto \left(\frac{1}{r}\frac{\partial}{\partial r} + \frac{1}{r^2}\frac{\partial^2}{\partial \phi^2}\right) A_y \tag{3.4}$$

Angular functions that fit the Dirichlet or Neumann boundary conditions are sine or cosine of $\frac{1}{2}m\phi$, where is m is an integer. In Morse and Feshbach, Methods of Theoretical Physics, p1383 [77] they consider the function

$$u(\phi) = \frac{1}{2}\sum_{m=0}^{\infty} \epsilon_m \cos\left[\frac{1}{2}m(\phi-\phi_0)\right] \begin{cases} J_{\frac{1}{2}m}(kr)H_{\frac{1}{2}m}(kr_0), & r<r_0 \\ J_{\frac{1}{2}m}(kr_0)H_{\frac{1}{2}m}(kr), & r>r_0 \end{cases} \tag{3.5}$$

were $\epsilon_m = 1$ when $m = 0$ and 2 when $m > 0$. This function is a solution to the wave equation in terms of half-integral trigonometric and Bessel functions. Its is interesting to note that this function is cyclic only after ϕ has reached a value of 4π, rather than 2π. This is useful as we can use half of its range to describe 'real space', for example from $-\frac{1}{2}\pi < \phi < \frac{3}{2}\pi$, and the region $\frac{3}{2}\pi < \phi < \frac{7}{2}\pi$ is the 'image space' which is out of the region we make the measurment where we can place the image source. When we set the boundary conditions only in the negative y axis the regions for the real and image space are as given in the example. The electric field at any point is the addition of the incident and scattered electric fields. For a point at infinity in 'real space' at $\phi = 0$ in the 'image space' would be at $\phi = 3\pi$. The combination of $u(\phi) - u(3\pi - \phi)$ is proportional to A_y allowing for us to use Eq. 3.4 to find E_y which satisfies the boundary conditions. This result is proportional to

$$\frac{\partial^2}{\partial x^2}\sum_{m=0}^{\infty} \epsilon_m \sin\left[\frac{1}{4}m(3\pi-2\phi_0)\right]\sin\left[\frac{1}{4}m(+3\pi+2\phi)\right] \begin{cases} J_{\frac{1}{2}m}(kr)H_{\frac{1}{2}m}(kr_0), & r<r_0 \\ J_{\frac{1}{2}m}(kr_0)H_{\frac{1}{2}m}(k0), & r>r_0 \end{cases} \tag{3.6}$$

As we are interested in the observation at a large distance away normal to the interface the Hankel functions can be replaced by their asymptotic form; using the convention that outgoing waves vary as $\exp(ikr)$, then the function is

$$H_\nu^{(1)}(z) \sim \sqrt{\frac{2}{\pi z}} e^{-i\pi\left(\frac{1}{4}+\frac{1}{2}\nu\right)} e^{iz} \tag{3.7}$$

With these simplifications and that for $\phi = 0$, $x = r$ Eq. 3.5 becomes:

$$E_y \propto \frac{\partial^2}{\partial r^2}\sum_{m=0}^{\infty} \epsilon_m e^{-\frac{1}{4}im\pi} \sin\left[\frac{1}{4}m(3\pi-2\phi_0)\right]\sin\left[\frac{3}{4}m\pi\right] J_{\frac{1}{2}m}(kr_0)\frac{e^{ikr}}{\sqrt{r}} \tag{3.8}$$

In Morse and Feshbach they show that u can be expressed exactly as

$$u\,(r,\phi) = \frac{e^{-ikr_0\cos\phi_0}}{\sqrt{i\pi}}\Phi\left[\sqrt{2kr_0}\cos\left(\frac{\phi_0}{2}\right)\right] \tag{3.9}$$

where Φ is the Fresnel integral defined by $\Phi(z) = \int_{-\infty}^{z} e^{it^2} dt$. In terms of the function $C(z)$ and $S(z)$ used by Abramowitz and Stegun [78]

$$\Phi(z) = \sqrt{\frac{\pi}{2}} \left[\frac{1}{2}(1+i) + C\left(\sqrt{\frac{2}{\pi}} z\right) + iS\left(\sqrt{\frac{2}{\pi}} z\right) \right] \tag{3.10}$$

As before the solution satisfying the boundary condition and wave equation is the combination $u(\phi) - u(3\pi - \phi)$ and thus

$$E_y = \frac{1}{2\sqrt{i\pi}} \left[e^{-ikr_0 \cos\phi_0} \Phi\left(\sqrt{2kr_0} \cos\frac{1}{2}\phi_0\right) - e^{+ikr_0 \cos\phi_0} \Phi\left(-\sqrt{2kr_0} \sin\frac{1}{2}\phi_0\right) \right] \tag{3.11}$$

Which is the solution found by Sommerfeld.
If kr_0 is large then both the Fresnel equations will approach the value $\sqrt{i\pi}$. With the source near the surface of the conducting sheet we get.

$$E_y \approx \frac{1}{2}\left(e^{-ikx_0} - e^{ikx_0}\right) = -i\sin(kx_0) \tag{3.12}$$

Thus $|E_y| \approx kx_0$ and independent of y_0. If the source is away from the conductor then the only term that is large is

$$E_y \approx \frac{1}{2} e^{-ikx_0} \tag{3.13}$$

and $|E_y| \approx \frac{1}{2}$
Fig. 3.5(a) shows a plot of Eq. 3.11 for a dipole being translated from -300 μm to 300 μm along the y direction at a position $x = 1$ μm under the conducting sheet with a frequency of 1 THz. As expected, there is suppression of the dipole when it is under the conducting sheet, however when the dipole is away from the conducting sheet it is free to emit. The amount of suppression depends on how close the dipole is to the metal and the oscillation frequency. The independence of y_0 for when the dipole is far from the edge of conductor as described by Eq. 3.12 and 3.13 is visible in the case under the metal mask. Fig. 3.5(b) is surface plot of the detected electric field for a dipole over a large range for x and y. The emitted radiation drops close to zero as it approaches the conductive sheet, the oscillations in the strength of radiation reveal interference phenomena, however experimentally, where a wide spread of frequencies are present, the oscillations are not expected to be noticeable.

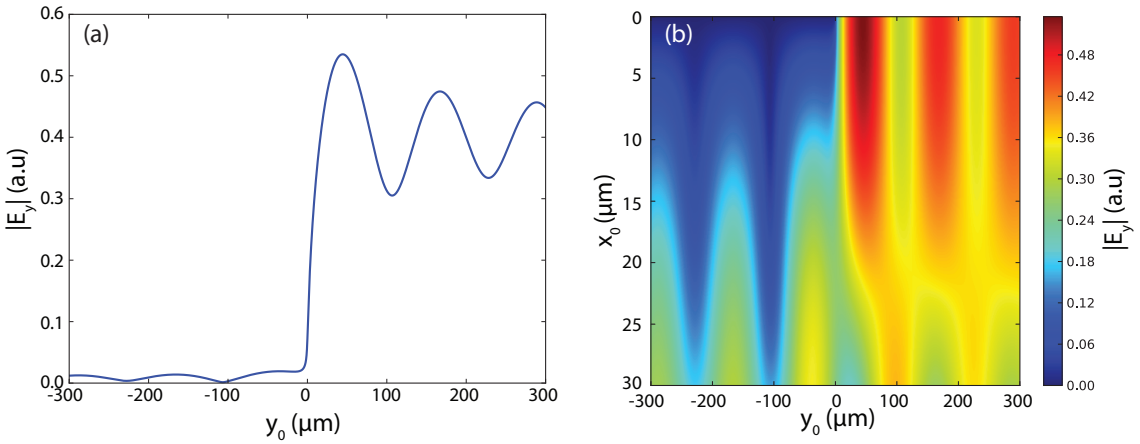

Figure 3.5: Plot of Equation 3.11 (a) Shows a plot of the equation corresponding to the electric field of a dipole radiating at 1 THz at a distance of 1 μm below the metal. (b) shows the same plot but over a wide range of spatial parameters in the form of a surface plot

3.3 COMSOL

Using a simple 1D drift diffusion model described in Section 2.2 and [58, 60] I modelled the evolution of an asymmetrical carrier concentration during and after photo-excitation from a sub-picosecond ultrafast laser pulse. The laser spot that generated the carriers has a FWHM size of 60 μm and had a FWHM length of 100 fs. The semiconductor was simulated such that it was partially obscured by a metal mask giving the carrier concentration an asymmetrical shape. The simulation was ran for 10 ps and the resulting current density evolution is shown in Fig. 3.6 for a number of time steps during the simulation. These data were then imported as a current along a 30 μm long 1D wire within a COMSOL model of the semiconductor device. The wire was positioned 1 μm bellow the semiconductor parallel to surface in the model. The wire can be seen in the close up of part of the first tile in Fig. 3.7. The problem was solved with and without a metal mask situated such that the edge of the mask matched the cut off used in the drift-diffusion model. Using the Transient Electromagnetic Waves module the model was run solving for the electric field in the y direction in plane with the simulation and parallel to the surface. In both situations the simulation was ran for 4 picoseconds after photo-excitation and I recorded the resulting electric field. Fig. 3.7 shows the electric field across the simulation for different time steps for both configurations. The configuration without the metal mask shows a quadrupole radiation pattern which has a zero component in the direction perpendicular to the surface. The configuration with the metal mask shows a dipole radiation pattern emitting perpendicular to the surface, the suppression of the emission under the metal mask is noticeable at early

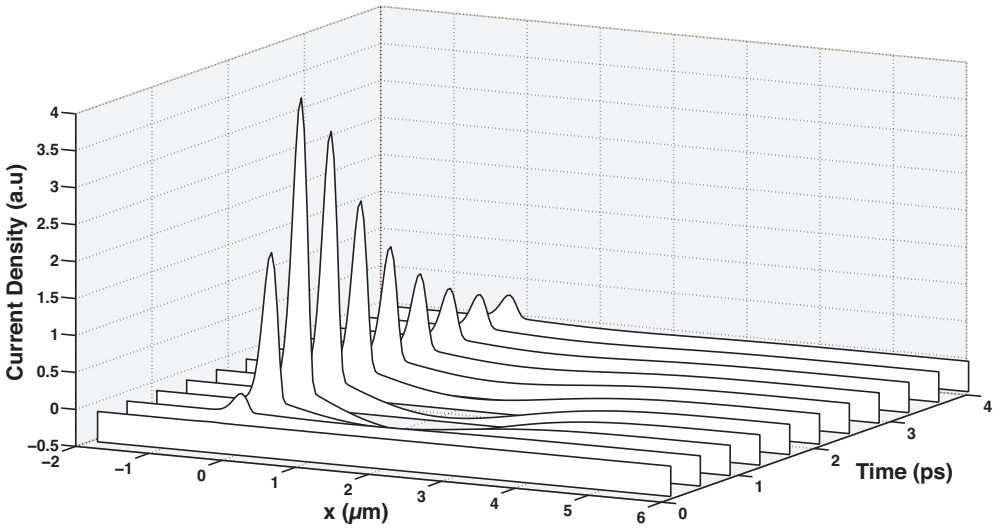

Figure 3.6: Calculated current density from the drift-diffusion equation for asymmetrical carrier excitation at metal-semiconductor interface at $x = 0$, no carriers are excited within negative region.

time steps. Fig 3.8 shows the electric field at the bottom centre of the simulation space as a function of time for both situations. This demonstrates that we only expect to see THz emission along the laser propagation axis if and only if there is a metal mask present near the carrier concentration. The direction of the propagation of the THz pulse is not exactly perpendicular to the surface of the semiconductor. Experimentally this is observed as to get the best alignment the Si-Lens needs to be aligned slightly of axis from the pump laser beam.

3.4 Conclusion

In this chapter I have demonstrated theoretically that any dipoles that form under a metal mask that are much less than a wavelength away will be suppressed, preventing it from radiating in the direction perpendicular to the surface. This prediction and the fact that asymmetrical carrier distributions cannot account for the detected emission. I propose an alternative explanation for observed THz emission from LPD emitter geometries. The suppression of radiation happens due to the long wavelength of the THz radiation in relation to the distance between the dipole and metal. The radiation that is reflected by the surface of the metal acquires a π-phase shift in relation to the non-reflected radiation [73, 74]. Interference between the non-reflected and reflected

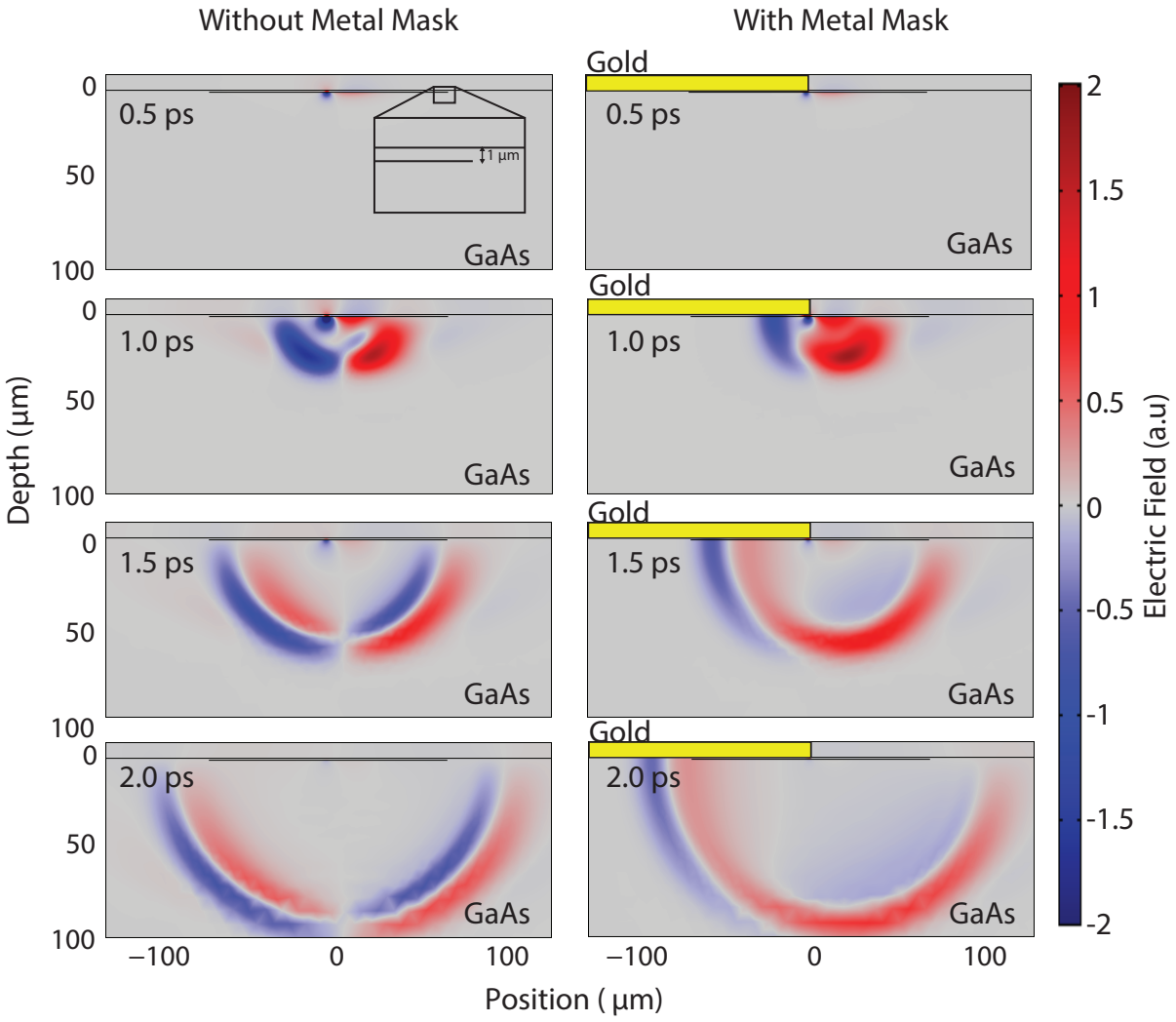

Figure 3.7: A model of the electric field produced by drift-diffusion after an asymmetric distribution of carriers is generated in GaAs; red is a positive field, blue is a negative field. The row on the left shows the evolution of the electric field in the situation when there is no gold layer. The row on the right shows the situation with a gold mask shown as a yellow rectangle.

radiation is destructive and causes the dipole under the metal to be suppressed, and no emission to be generated in the y direction [75].

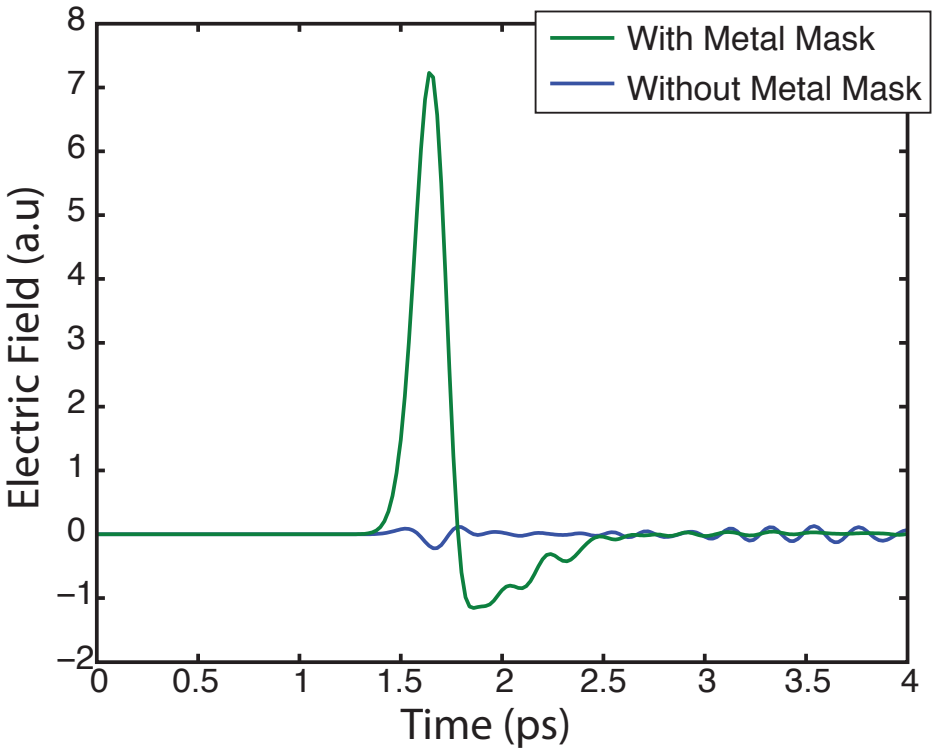

Figure 3.8: A model of the dynamic electric field (z-axis) produced by drift-diffusion after an asymmetric distribution of carriers is generated in GaAs; red is a positive field, blue is a negative field. In (a), a layer of gold is on top the GaAs indicated by the yellow rectangle. In (b), there is no gold layer and the horizontal white line denotes the surface of the semiconductor.

Chapter 4

Lateral Photo-Dember THz Emitters

4.1 Introduction

So far I have discussed an alternative explanation for mechanism of THz generation from lateral photo-Dember emitters and presented theoretical arguments supporting this mechanism and show that the mechanism presented in [1] is not enough to explain the THz emission. In this chapter I will present experimental results that support this new interpretation and present further experimental studies to investigate the nature of the THz emission mechanism.

In the first experiment I experimentally verify the direction of the emitting dipole from a LPD device and show that its direction is in agreement with my interpretation and contradicts the explanation given by Klatt et. al. In the second experiment I fabricated a LPD emitter with an insulating layer between the metal contact and the semiconductor surface. By doing this I eliminated any internal electric field that may have arisen from the Schottky contact and observe no loss in THz emission demonstrating that the emission observed is form diffusion currents alone. Next I experimentally study the effect of an applied external bias across a LPD emitter demonstrating enhancement and suppression of the emission as well as further demonstrating the direction of the emitting dipole and confirming the validity of our model. I then study how the emission depends on the spots shape and proximity to the metal:semiconductor interface. Finally I study the emission as a function of fluence and spot sizes up to saturation for different semiconductor substrates.

The experiments presented here were all conducted with a THz-TDS setup here at the University of Southampton THz Lab. To study the LPD effect the optical beam was

modulated using a mechanical chopper, rather than a modulated electric bias, allowing for synchronous detection with a lock-in amplifier. A 100 fs Ti:Sapphire laser centred at 800 nm and repetition rate of 80 MHz was used as the pump. For all of the experiments the detector used was a PC antenna from Menlo GMBH. A schematic of a typical LPD THz-TDS is shown in Fig. 4.1.

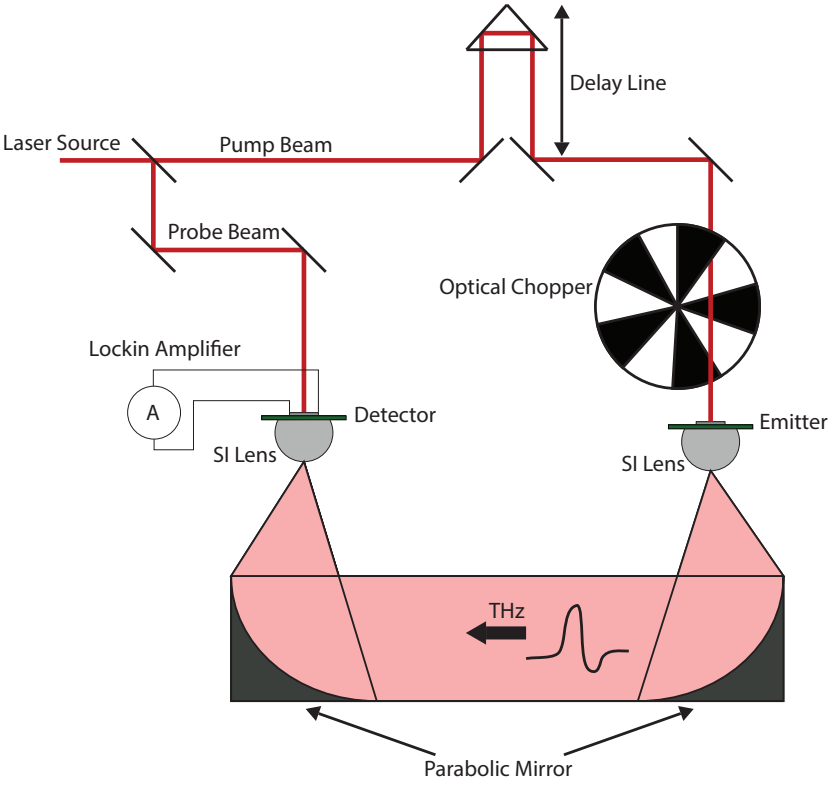

Figure 4.1: Schematic of a typical THz-TDS.

4.2 Parity Experiment

The hypothesis in [1] is that the discontinuity in the carrier distribution will create a dipole directed towards the metallic region while my theoretical model predicts the formation of a net dipole in the opposite direction due to the suppression of dipoles beneath the metal. Figure 4.2 shows a simple schematic of the emitting dipoles for both interpretations. In THz-TDS the amplitude and phase of the electric field is directly measured thus the direction (sign) of the E-field can found and compared between experiments. At first a 5 μm-gap LT-GaAs bow-tie PC antenna emitter was used biased with a 9V battery, as shown in Fig. 4.3(a) with the laser focused on top of position A.

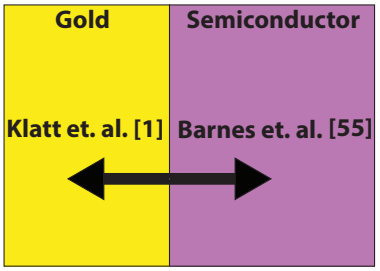

Figure 4.2: Schematic showing the different direction of the predicted dipole moment from the theory given in [1] and the one presented here.

The polarity of the THz emission was mapped to the direction of emitting dipole by

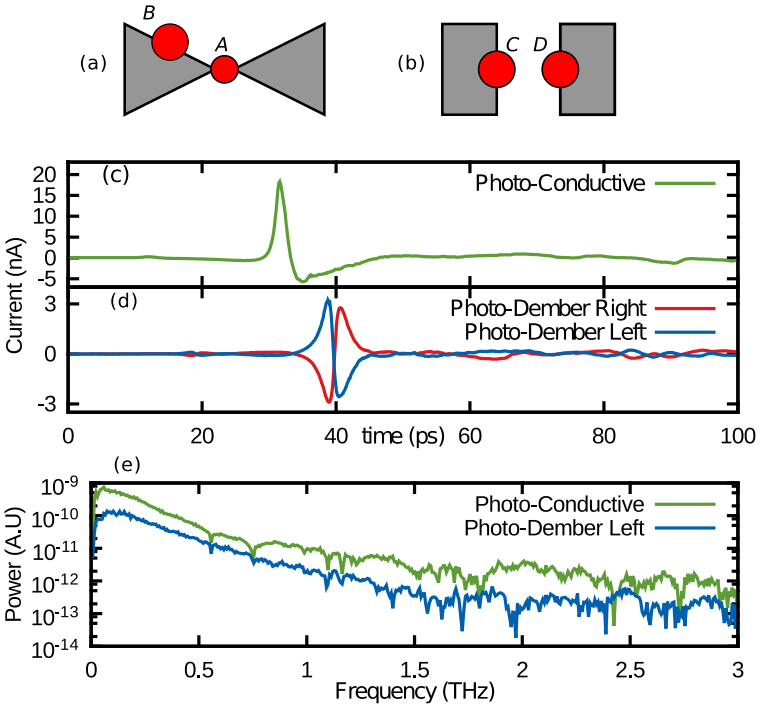

Figure 4.3: Diagram showing the placement of the laser beam on (a) the bow-tie PC emitter and (b) the LPD emitter. (c) Shows the current recorded in the time domain for a PC antenna. (d) shows THz emission at two opposite boundaries to observe the predicted sign change. (e) shows the Fourier transform of (a) and (b) demonstrating comparable bandwidth between the PC and LPD emitter. The experiment was performed in ambient atmosphere.

measuring the sign of the THz emission and then flipping the battery. One of the measurements is shown in Fig. 4.3(c). The same PC antenna was then disconnected from the battery and translated so that the pump was at position B, shown in Fig. 4.3(a) where a metallic edge was used as a LPD emitter. The polarity of the THz waveform indicated that the current was flowing as expected in our argument where

the radiating dipole is in the non-masked region of the antenna. The PC emitter was then replaced with a dedicated LT-GaAs LPD emitter and the LPD effect was measured on two opposite edges of metal strips, areas C and D in Fig. 4.3(b); The results are shown in Fig. 4.3(d), where I note the expected polarity change between opposite edges. In Fig. 4.3(e) the spectra of PC and LPD antennae are illustrated, showing similar bandwidths produced from the LPD and the biased PC emitter. The spectra were obtained in ambient atmosphere and show water absorption features. This result is the main result that I present in [60].

4.3 Insulating Layer

Near a metal:semiconductor interface, if there is a difference between the work functions of the metal and semiconductor, there will exist a depletion region near the contact as the Fermi-energy level has to be continuous. This depletion region creates an electric field near the contact which can accelerate photo-excited carriers generated within this region. Fig. 4.4 illustrates what happens to the conduction band in a semiconductor as a metal approaches its surface. Fig. 4.4(a) represents the situation when the metal

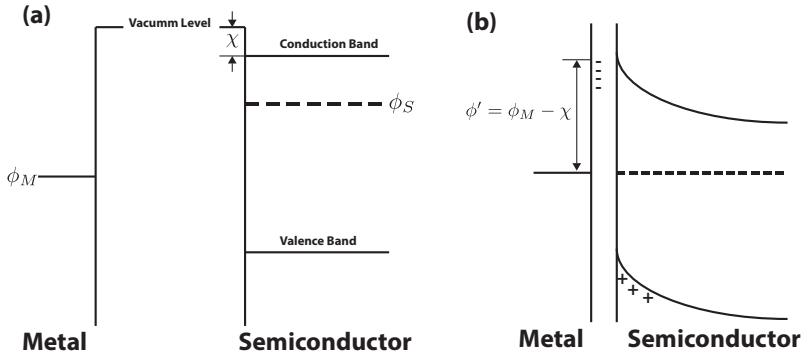

Figure 4.4: Energy diagram showing the formation of a barrier and band bending due to a metal contact on a semiconductor without surface charges. (a) Shows the situation when the contact is far away from the semiconductor surface and thus there is no band bending. (b) shows the situation when the metal is close or in contact with the semiconductor surface.

is far from the semiconductor surface. Here the Fermi level of the metal and semiconductor are ϕ_M and ϕ_S respectively, the electron affinity of the semiconductor is given as χ and represents the energy to move an electron from the conduction band just inside the semiconductor into the vacuum just outside of the semiconductor. As the metal and semiconductor approach carriers flow between the two until an equilibrium is reached and the Fermi energy is continuous. This situation is shown in Fig. 4.4(b). This leads to band bending as charge builds up at the interface. Because the

charge density of the semiconductor is much lower than the metal the carrier density is affected far into the semiconductor. The change in density produces a space charge region and the band bending. The amount of band bending and its direction depends on the metals and semiconductors work functions. For n-type semiconductors a positive space charge region forms when the work function of the metal is greater than that of the semiconductor, as shown in Fig. 4.4(b). for p-type semiconductors a negative space charge region forms when the work function of the metal is less than that of the semiconductor.

To eliminate the possible contribution of this electric field to the detected THz emission from my devices we fabricated a LPD sample with two contacts, one with an insulating layer between the metal and the semiconductor and one without. A metal contact of 5 nm of Chromium and 100 nm of Gold was evaporated onto the surface of a LT-GaAs substrate. The sample was then spun coated with 100 nm of insulating poylmide (PI) and another Cr:Au contact was evaporated onto the sample as shown Fig. 4.5. The

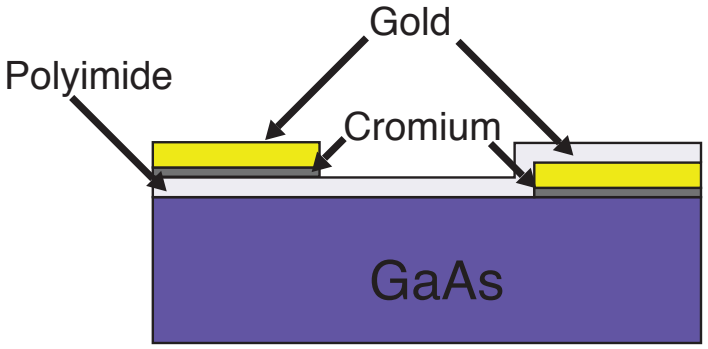

Figure 4.5: Schematic of LPD with and without insulating layer

sample was used as a LPD emitter in a typical THz-TDS. First the emitter was aligned for emission from the metal:semiconductor contact and the emission was measured. The sample was then translated to the insulated contact and the emission was still observed with the same peak to peak current, same shape but opposite sign as expected. A scan of this result is shown in Fig. 4.6. This conclusively demonstrates that the source of the detected THz radiation from our LPD emitters on LT-GaAs are not due to drift currents within the depletion region at the metal:semiconductor interface.

4.4 Bias

To investigate the validity of the numerical model I determined experimentally how an applied electric field suppresses or enhances the LPD effect. I fabricated a LPD emitter with two Cr:Au contacts separated by a 200 μm semiconductor gap on the surface of

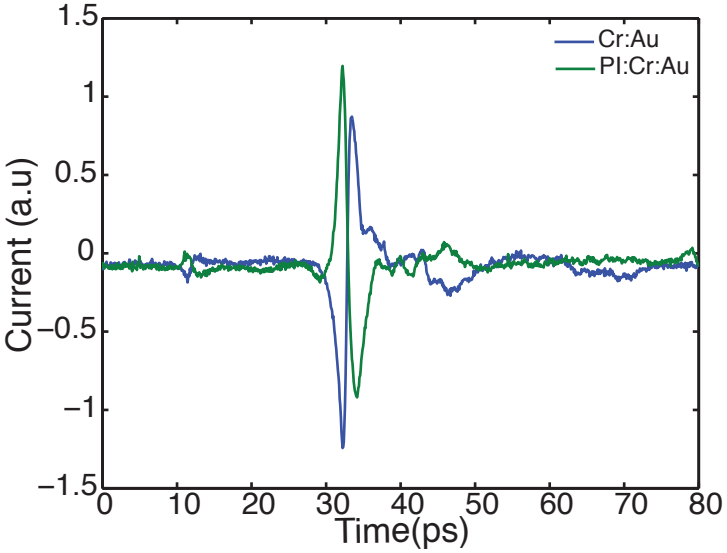

Figure 4.6: Emission from insulated and non-insulated LPD emitter

an LT-GaAs substrate. These metal contacts were used as both electric contacts to apply an external bias and metal masks for the LPD effect. The pump laser of the THz-TDS was focused onto the LPD emitter half on the gold mask and half on the semiconductor with a spot size of $\sim$ 60 μm FWHM and average power of 150 mW. The gold contacts were connected to a DC variable power supply. I then measured the THz emission from the LPD emitter as a function of applied external electric field from -0.75 kV/cm to $+0.75$ kV/cm. In Fig. 4.7 I have plotted the time domain scans of the detected THz pulse with a DC electric field of -0.75 kV/cm, $+0.75$ kV/cm and 0 kV/cm showing a clear enhancement and suppression of the THz emission. Using the drift-diffusion model described in Chapter 2 I added an applied electric field to the electric field in Equation 2.5 such that $E = E_{bias} + E_{\phi}$ where E_{bias} is the applied electric field across the region not under the metal contacts and E_{ϕ} is the electric field found by solving Possion's equation for the carrier densities in the model. The resulting peak amplitude of the predicted THz emission is plotted in the insert of Fig. 4.7 as a function of DC electric field. A clear linear dependency was discovered that is in good agreement with the theoretical diffusion model showing that the drift-diffusion equation adequately describes the LPD emitter geometry. The experimental parameters used were still in the linear regime of THz emission as a function of bias voltage and thus I did not observe enhancement of photoconductive emission due to trap enhanced electric fields [79, 80]. According to [81] where a LT-GaAs strip line emitter has been tested I was using a much lower bias than would be ideal for a strip line emitter with a gap of 200 μm.

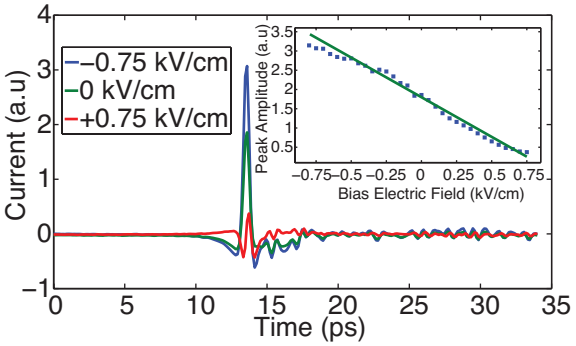

Figure 4.7: Time domain of detected THz emission from LPD emitter biased at −0.75 kV/cm, 0 kV/cm and +0.75 kV/cm; the sign of the electric field corresponds to the sign of the charge of the irradiated electrode. Insert shows experimental and theoretical results of the amplitude of THz pulse peak from LPD emitter as a function of applied electric field.

4.5 Dependency on spot shape and metal mask position

So far in this chapter experimental evidence were given that support the validity of the dipole quenching mechanism interpretation and the validity of the simple drift-diffusion model. To further investigate the nature of this emission I measured the emitted THz emission for different spot shapes and their position to the metal mask.

Experimentally, an impedance matched hyper-hemispherical Si-Lens is used to help out-couple the THz from the semiconductor device and minimise internal reflections and beam dispersion. The alignment of the Si-lens is critical and I have found that for optimal performance with LPD emitters the position of the lens needs to be slightly off axis from the laser beam path. The reason for this is apparent in Fig. 3.7 for the case without the metal mask where it can be seen that the peak emission emits slightly off axis. When having the Si-Lens centred away from the laser beam axis and the laser spot far away form the metal interface I could still detect THz radiation but it was almost 50 times less than that when the laser is focused at the interface for the LPD effect. Fig. 4.8(a) shows this emission in comparison to the radiation of the LPD effect. The origin of this weak THz signal is likely to be due to the out-coupling of the quadrupole radiation generated by LPD effect as seen in Fig. 3.7(b) and of the radiation generated from the surface emission effect which is quite prominent in GaAs [50, 53]. With the Si-Lens fixed to the LPD emitter and centred in between the two deposited gold layers, the sample was translated so the laser spot moved across the surface of the emitter. The signal amplitude of the main peak of the emitted THz was recorded as a function of spot position and shown in Fig. 4.8(b) where the two gold edges are positioned at $x = 0$ & $200\,\mu$m.

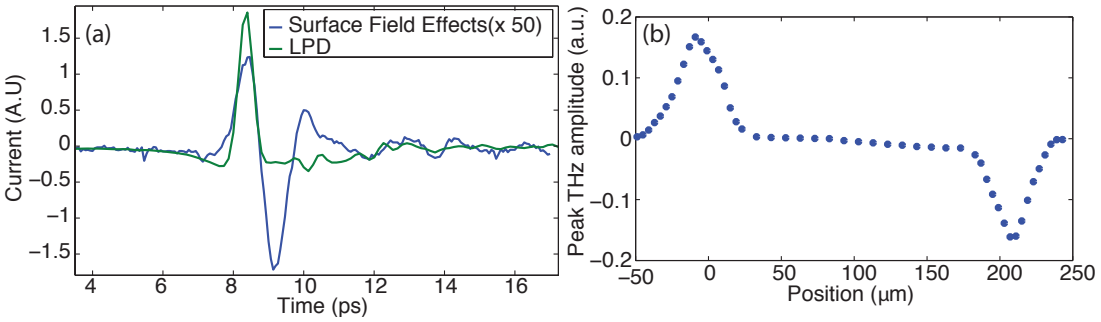

Figure 4.8: (a) The THz radiation from a Gaussian pump spot on bare LT-GaAs in comparison to the radiation observed from radiation of the metal edge (LPD effect). (b) The peak THz signal detected as a function of position across the semiconductor surface which is enclosed between two parallel gold regions separated by 200 μm. THz radiation from bare LT-GaAs originates from diffusion current and surface fields, due to the strong focusing provided from the combination of the Si-lens and parabolic mirrors.

As expected, the THz signal detected depends on the position with respect to the gold edges. The sign of the THz electric field flips when the laser is centred on the left or right metal mask. Half way across the gap the signal competently vanishes as the Si-Lens and laser spot are perfectly aligned and thus no emission is observed. This flipping of sign is characteristic of lateral photo-Dember currents and is consistent with both the explanation given by Klatt et.al [1] and the one presented here.

Next I aligned the same LPD emitter with the Si-Lens fixed to the laser pump beam

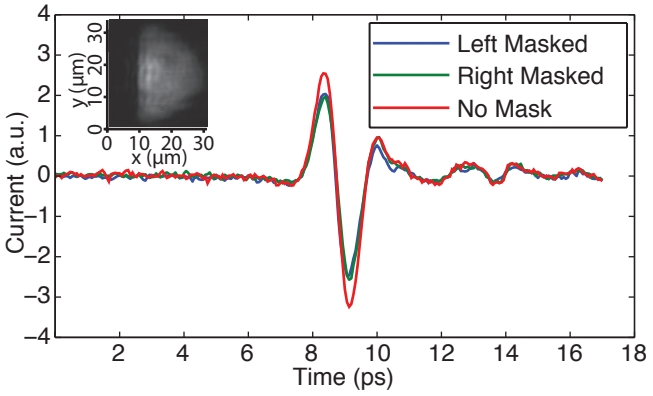

Figure 4.9: The THz radiation from bare LT-GaAs from a whole spot and two half-masked Gaussian spots, by shadow-masking opposite sides of the Gaussian laser spot. The insert shows a photo of an image of the shadow masked spot on the bare semiconductor surface, we found the spot to have a HWHM on one side to be ~ 3 μm and the other to be ~ 12 μm.

and translated the sample such that the laser spot with a spot size of ~ 30 μm FWHM was more than 50 μm away from the metal edge on the semiconductor surface where

I could only measure the weak THz radiation explained above. A THz-TDS scan of this emission from an un-masked guassian laser spot is shown as one of the scans in Fig. 4.9 and is similar to the surface field effects scan shown in Fig. 4.8(a). A knife edge was then imaged onto the surface and used to shadow-mask the laser spot such that it formed a semicircular, half-Gaussian spot, thus creating an asymmetrical carrier distribution similar to that when using a metal mask, a schematic of this is shown in Fig. 4.10(a); a THz-TDS scan was then measured at this configuration. The knife edge was then rotated such that it masked only the opposite half of the laser spot and again a scan was acquired. The results of this experiment are shown in Fig. 4.9, there is no enhancement when the carrier concentration is made asymmetrical and the sign of the THz emission does not flip when the knife was rotated.

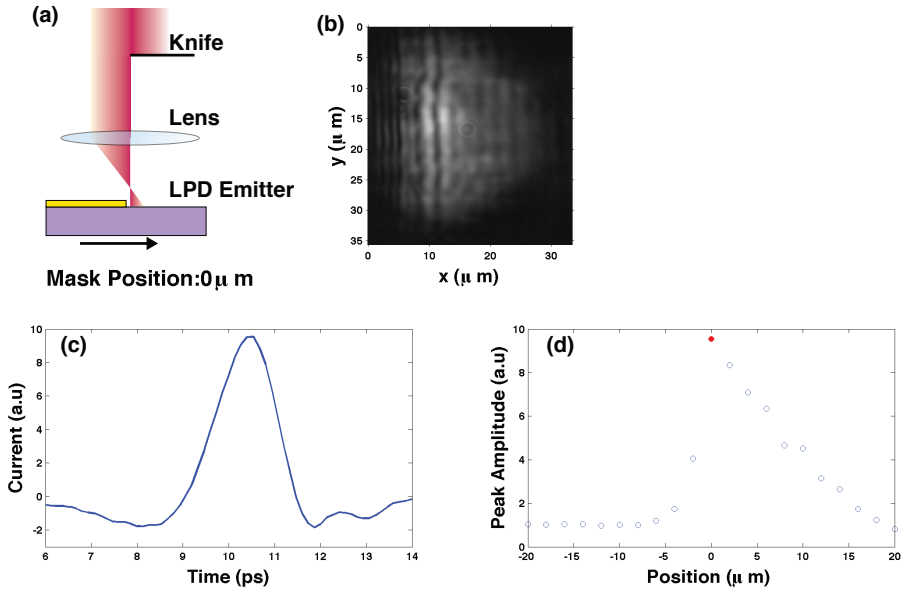

Figure 4.10: (a) Schematic of experiment where the metal-semiconductor interface of the LPD emitter (extending to the left) is translated underneath the shadow masked semicircular pump spot. The rest of the figure is the central frame from Media 1 in [2]. (b) Shows an image and scale of the semicircular pump spot on the surface of the LPD emitter (c) time scan of detected THz signal (d) peak amplitude of detected THz emission for different metal mask positions, highlighted spot is the current position. In this case the metal-semiconductor interface is at the sharp edge of the semicircular pump spot, which we define as mask position 0. Position -20 μm is when the metal edge is to the far left of the image; position 20 μm is when the metal edge is to the far right and all the illuminated spot is covered by the metallic region.

With an asymmetrical spot I translated the metal edge of the LPD emitter under the shadowed region as shown in Fig. 4.10(a), and took THz-TDS scans every 2 μm until

the spot was completely on the metal mask. Figure 4.10(b)(c)(d) shows the central frame from Media 1 video in [2] where these results are presented.
These experiments, the bias experiment, and the insulating layer experiment have been published in [2, 82, 83].

4.6 Fluence and Spot Size

Unannealed LT-GaAs suffers from a lower dark resistivity than annealed LT-GaAs due the arsenic point defects allowing for electron hopping [84]. The annealing process creates precipitates from the excess arsenic [85] increasing the dark resistance. A large difference between dark and light resistance is preferable for PC switch antenna as the emission is from an ultrafast current that is generated when carriers are generated by a laser pulse and accelerated by an external electric field [86]. Annealing also increases the carrier mobilities but increases the carrier lifetime from hundreds of femto-seconds to a few pico-seconds [87]. LPD emitters do not require an external bias and thus the difference between light and dark resistivity is less important. Terahertz emission from the LPD effect is affected by the difference in mobilities of the carriers and carrier lifetime. However it is not immediately clear if greater mobilities or faster carrier lifetimes is more important. To investigate this I tested the performance of unannealed/annealed LT-GaAs and semi-insulating (SI) GaAs samples. SI-GaAs is high quality grown GaAs giving it a greater difference in mobilities than LT-GaAs but also much longer carrier lifetimes [88].
The emission for each emitter is measured for different fluence and spot size pump parameters all centred on the semiconductor:metal interface. A neutral density filter wheel was used to vary the average pump power and focusing optics were translated to vary the spot sizes. Knife edge measurements were used to calculate the $1/e^2$ spot size radius. For each sample the peak to peak amplitude of the emitted THz electric field from one metal edge for different spot sizes and average pump powers were measured. From these data I calculated the fluence for each measurement and fitted a saturation curve. The saturation curve was given by $E_{THz}(F) = A\omega F/(F + F_{sat})$, where A is a coefficient of conversion and alignment efficiency, ω is the $1/e^2$ spot radius, and F_{sat} is the saturation fluence.
The results from this experiment have been presented partly in [2, 89] and a journal publication that is currently under peer review.

4.6.1 Unannealed LT-GaAs

The results from the unannealed LT-GaAs emitter are shown in Figure 4.11(a), the lines are the fit of the saturation curve. For this sample the the average saturation fluence was found to be $F_{sat} = 0.116$ mJ/cm^2. The saturation arises due to the finite density of states in the conduction band. As it can be seen in Fig. 4.11(a), higher THz peak to peak currents were observed for larger spots with the same average fluence. This demonstrates that for optimal performance large spot sizes are needed with high average pump powers. Figure 4.11(b) shows the calculated efficiency curve for the

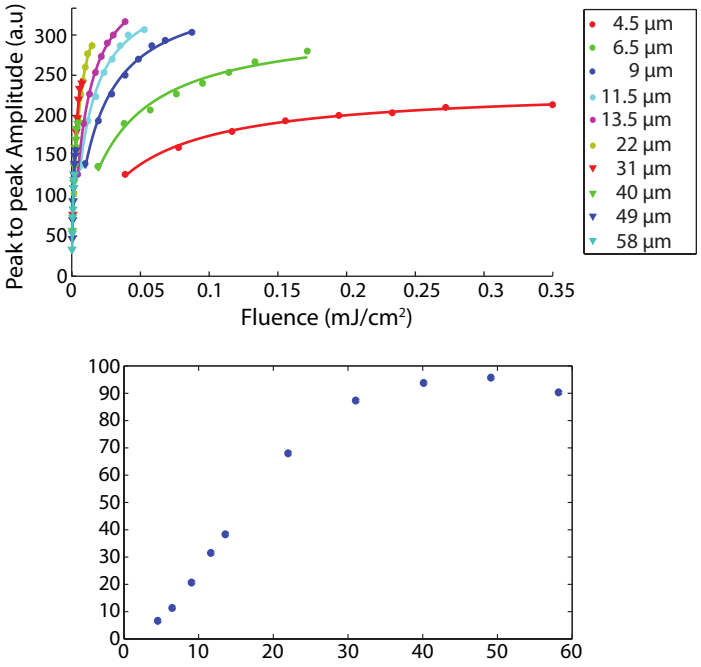

Figure 4.11: THz emission from unannealed LT-GaAs. (a) Peak to Peak amplitude of detected THz emission for different spot size radii ($1/e^2$) and average powers plotted as a function of fluence. The solid lines are saturation curve fits. (b) Calculated efficiency curve using the saturation formula and fitting parameters from the fits shown in Fig. 4.11(a) for a constant fluence of 0.01 mJ/cm^2 with increasing spot size.

emitter using the saturation formula and fitting parameters obtained from Fig. 4.11(a). Here a constant fluence of 0.01 mJ/cm^2 was used with increasing spot size. There is an initial increase in efficiency of the device as the spot gets bigger before reaching roll-over. The increase in efficiency is expected because the emitting region at the interface is getting expanded thus increasing the number of participating carriers. I attribute roll-over in this figure to a loss in out coupling efficiency with the Si-Lens as the spot

size approaches the wavelength of THz radiation and we move away from a point dipole approximation.

4.6.2 Annealed LT-GaAs

Duncan McBryde performed the same experiment on an annealed LT-GaAs sample which I then analysed the data from. Figure 4.12 shows the results for the annealed LT-GaAs sample. The saturation curves of the annealed LT-GaAs sample has a similar

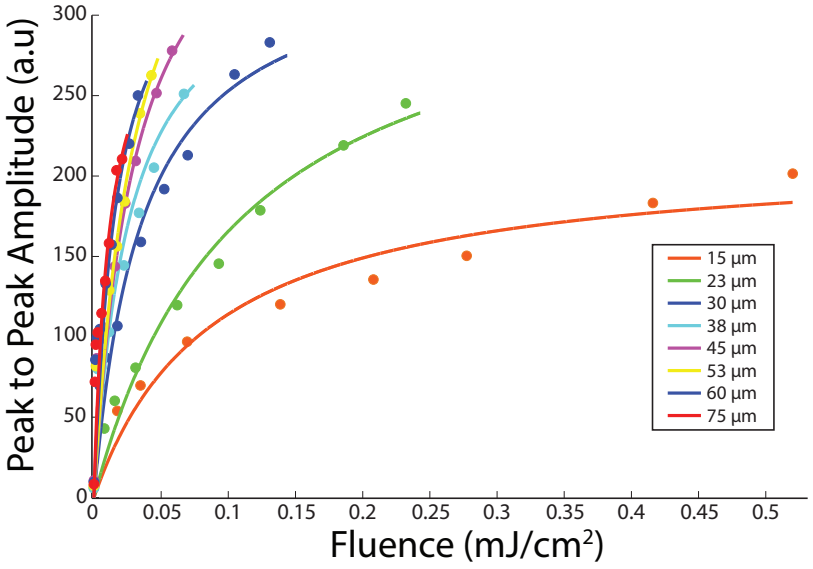

Figure 4.12: Peak to Peak amplitude of detected THz emission from annealed LT-GaAs for different spot size radii ($1/e^2$) and average powers plotted as a function of fluence. The data points above 3 μJ/cm^2 are fitted to the typical saturation curve. The data points below 3 μJ/cm^2 are excluded as they form a different saturation regime.

shape to the results of the unannealed LT-GaAs. At a fluence below 3 μJ/cm^2 however the sample is more efficient than the unannealed emitter before rolling off and then increasing in power again to produce the main saturation curve seen here. Figure 4.13 shows a close up of the region around 3 μJ/cm^2 showing this initial roll over region. Annealed LT-GaAs LPD emitters thus have two distinct saturation domains where as unannealed samples do not. Before the first saturation, the output from the annealed sample is greater than that from either the unannealed sample and the semi-insulating samples at the same spot size and fluence. After this saturation region the THz output power goes linearly with optical fluence till the second saturation point. Time domain scans from the two different regions is shown in Fig. 4.14. The pulse shape from

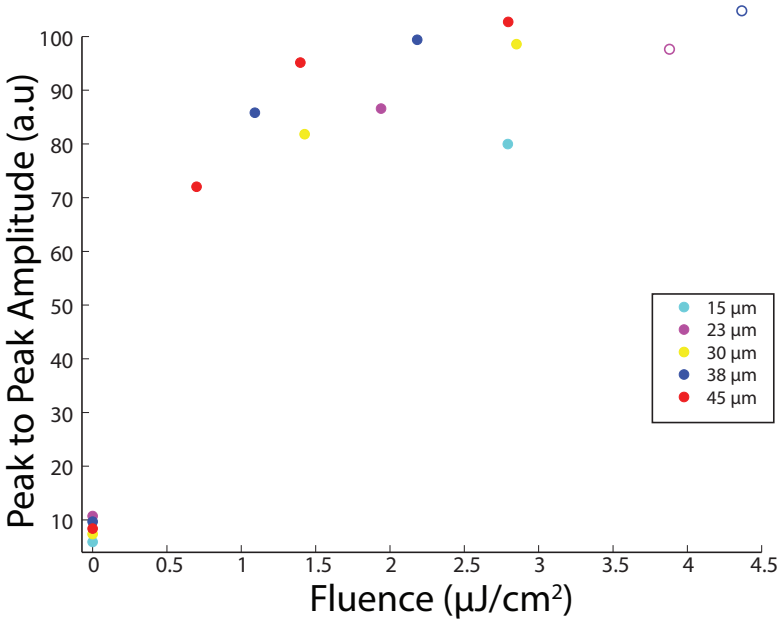

Figure 4.13: Close up of Figure 4.15 showing the region below 3 μJ/cm^2. The filled circles show the first saturation regions.

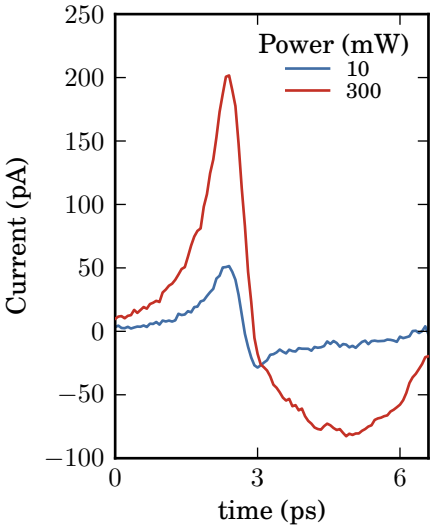

Figure 4.14: THz time domain scans for annealed LT-GaAs LPD emitter for emission within the two different saturation regions. For both scans the spot radius was 75 μm.

either region is different from one another with the second saturation region having a longer tail. This indicates that different carrier dynamics are at play between the two regions. Longer tails are characteristic of longer carrier recombination times and the sample taking longer to reach equilibrium. At low fluence the trap sites responsible for fast carrier recombination have not been saturated. But as the fluence increases traps become saturated and filled increasing the carrier lifetime of the carriers in the sample. As the carrier density increases the carrier scattering time drops reducing the mobility of the electrons [90]. As the top LT-GaAs layer becomes saturated it will become transparent and the pump will penetrate deeper into the sample also exciting the SI-GaAs substrate further changing the carrier dynamics of the sample [91]. The change in carrier dynamics within annealed LT-GaAs with fluence has been observed with THz-TDS [92]. Here I have fitted the saturation curve to the second saturation region as there is insufficient data points for the first domain to get a good fit.

4.6.3 SI-GaAs

Duncan McBryde also performed this measurement on a SI-GaAs sample which I then later analysed. Figure 4.15 shows the results from the SI-GaAs sample. The SI-GaAs LPD emitters were significantly less efficient than either the annealed or unannealed LT-GaAs emitter. The carrier mobilities are larger in SI-GaAs than LT-GaAs however the carrier lifetime is much longer indicating that the carrier lifetime and existence of traps plays a bigger role for LPD emitters than the carrier mobility. SI-GaAs is also easier to saturate due to longer carrier lifetime and the lack of fast traps. Interestingly the SI-GaAs based LPD emitters exhibit a drastic reduction in signal after saturation. This reduction continues till the sign of the THz pulse flips. Fig. 4.16 is Figure 4.15 plotted on a semi-log plot by taking the log of the x axis. This makes it easy to see the inversion and the curve fitting which was only fitted to data before the power started to drop. The flip in sign interestingly depends strongly on the optical beam position and the effect is only observable when the centre of the pump beam is within ± 20 μm from the metal:semiconductor interface. Figure 4.17 shows time domain scans from the same emitter as the pump power is increased for a spot size of 15 μm, showing the flip between these two different regimes. The flip indicates that there are two competing mechanisms for SI-GaAs LPD emitters at high fluence. This competing mechanism is under investigation by Duncan McBryde and maybe due to an inversion of the Schottky barrier very close to the interface which occurs only at high flunece as carriers building up at the interface forming mirror charges [93]. An insulated contact was also fabricated on an SI-GaAs sample which again showed no loss in performance however the flipping of the THz emission was not observed further indicating that the

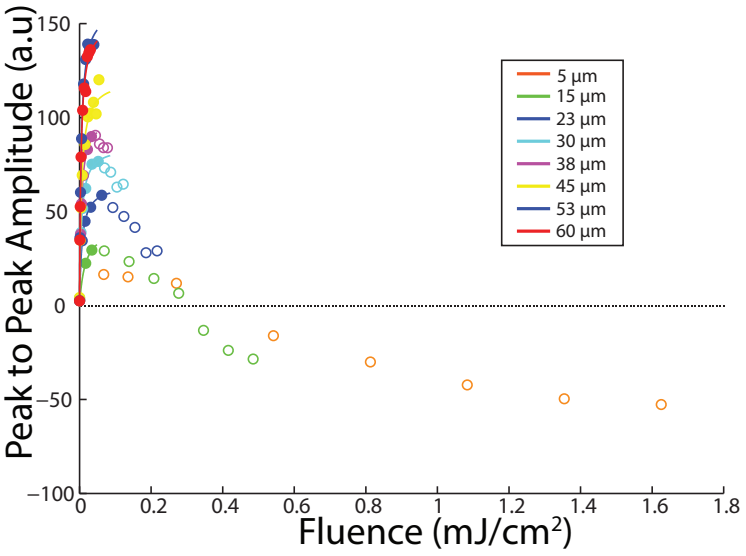

Figure 4.15: Peak to Peak amplitude of detected THz emission from SI-GaAs for different spot size radii ($1/e^2$) and average powers plotted as a function of fluence. The dependency at first gives a normal saturation curve but then starts to drop and at high fluence the sign of the THz emission flips. This flip is due to another mechanism becoming more dominant. The saturation fit was only fitted at low fluence before the competing mechanism is noticeable. Circled data at higher fluence are excluded from the fit.

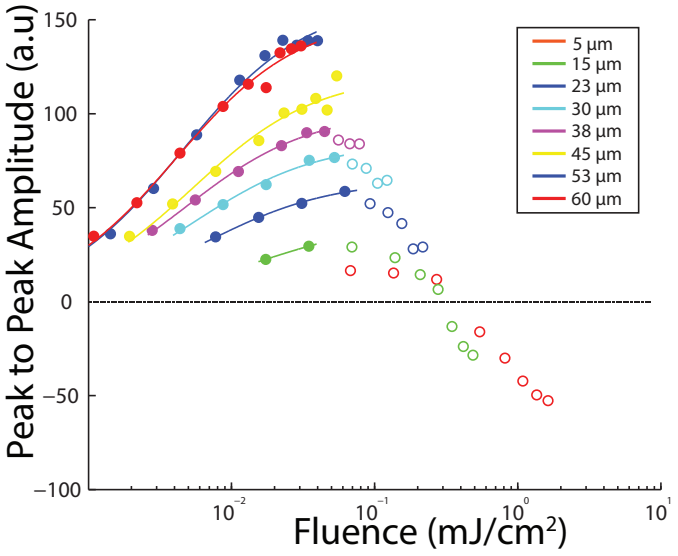

Figure 4.16: Semi-log plot of Fig. 4.15. Log graph showing the fitting of the saturation curve before the power drops off and inverts. Only filled circles are fitted to.

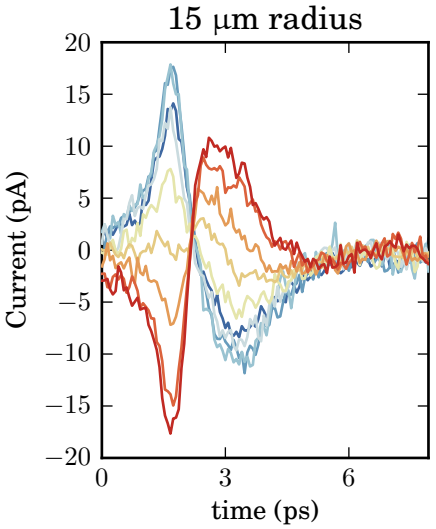

Figure 4.17: THz time domain scans for the SI-GaAs LPD emitter with a spot size of 15 μm for different pump intensities demonstrating the flip in sign at high fluence.

the Schottky barrier is playing a role for this competing mechanism. The electric field in this case is likely to be very strong and in opposition to the diffusion currents that are normal responsible for emission from LPD emitters. Fluence dependent THz polarity from Au:GaAs interfaces in PC emitters has also been observed in Ref. [94].
Using the same equation for saturation I fitted the curve to the annealed LT-GaAs data excluding data from the first saturation region and for the SI-GaAs data excluding data when the second mechanism starts competing with the primary mechanism. The resulting saturation fluence were found to be 0.0437 mJ/cm^2 for annealed LT-GaAs and 0.0058 mJ/cm^2 for SI-GaAs.

4.7 Conclusion

LPD devices as demonstrated in [1, 55, 56, 57, 60] can efficiently generate THz radiation that is easily out-coupled. A single LPD emitter can give comparable THz bandwidth to a PC antennae albeit approximately a sixth of the peak THz current [1, 60]. An advantage of LPD devices over PC devices is that they do not require a high-voltage bias to be maintained across the semiconductor making them more durable. Furthermore, emitters based on lateral diffusion currents and dipole radiation suppression are simple to fabricate, opening up possibilities for easier THz integration and interfacing with other THz elements.
Here I have presented experimental evidence that the sign of the emitted THz emission from LPD emitters is in contradiction with the idea that an asymmetrical carrier

distribution alone can lead to net diffusion current but is in agreement with the new theory of the mechanism presented in this thesis. Contribution from drift currents at the Au:GaAs interface was also eliminated by using an insulating layer without reduction of THz emission. I have also further investigated the role of the metal mask used for LPD emitters and how it affects the THz emission changing it from a weak THz radiation originating from surface field effects to THz radiation from the diffusion current of the LPD effect. Furthermore, the emitted THz radiation was enhanced or suppressed by applying a DC electric field across the LPD emitter and gave good agreement with results from my numerical computer model. I demonstrated that regardless of the symmetry of the carrier distribution without a metal mask no dipole emission was generated from lateral diffusion currents. However, I was able to observe quadrupole radiation from diffusion and surface emission effects when in a lateral transmission geometry depending on the alignment of the hyper-hemispherical Si-Lens with the beam axis. Finally, I have taken saturation measurements of the LT-GaAs and SI-GaAs samples finding the saturation fluence for the effect and showing that the optimal parameters are high powers and large spot sizes making the emitters very easy to align. For comparison the peak to peak amplitude for all three samples for a spot size of 22 μm is plotted in figure 4.18.

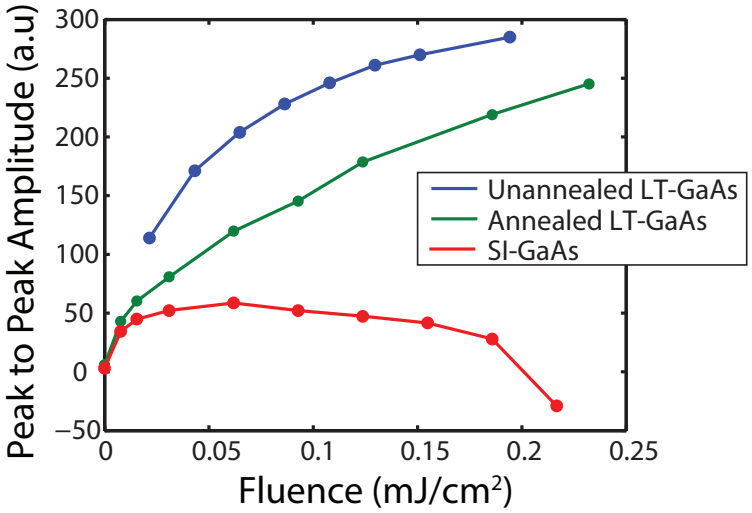

Figure 4.18: peak to peak amplitude of unannealed LT-GaAs, annealed LT-GaAs, and SI-GaAs as a function of fluence for a spot size of 22 μm. Line are for guiding the eye

Unannealed LT-GaAs gave the best efficiency and highest saturation fluence and behaved as expected over the parameter range tested. Annealed LT-GaAs on the other hand exhibited a double saturation which can be explained with trap saturation. The SI-GaAs exhibited a competing mechanism for high fluence which is still under investigation.

Chapter 5

Multiplex lateral Photo-Dember Emitter Design

5.1 Introduction

LPD emitters have advantages over PC emitters in that they do not require an external bias, are easier to fabricate, and slightly higher bandwidths. However single LPD emitters are not as efficient as PC emitters limiting their usefulness. In [56] Klatt et. al. present a multiplex LPD emitter that is comparable to commercial PC emitters however the fabrication of these devices is complicated as it requires the fabrication of 3D structures. To address this short coming and with the full mechanism in mind I proposed two different designs for multiplex LPD emitters. One based on an array of gold strip-lines on a semiconductor and lenticular lens array for the focus geometry and the other based on a double metal strip-line pattern without the need for any focusing geometries. In this chapter I will give a description of these two types of multiplex emitters. I will then present the fabricated devices and experimental evidence of their functionality done in collaborations with Duncan McBryde and Paul Gow. We find that both new types of emitters work as well as the ones presented by Klatt et. al. yet are simpler to fabricate.

5.2 Antenna Design

The first emitter design consists of an array of gold strip-lines evenly spaced across the substrate. In order for each strip-line to act as an emitter, the pump beam needs to be focused only on one side of each strip-line. If the entire pattern was illuminated there

would be no THz emission as both sides of each metal strip line will radiate causing destructive interference preventing wave propagation perpendicular to the surface. In order to focus only on one side of each metallic strip a mico-lenticular lens array can be used as the focusing optic if its period is chosen to complement the striplines fabricated on the device. Fig. 5.1 shows a schematic of single metal stripline LPD multiplex emitter and focusing optics. Upon illumination each strip line will act as an individual

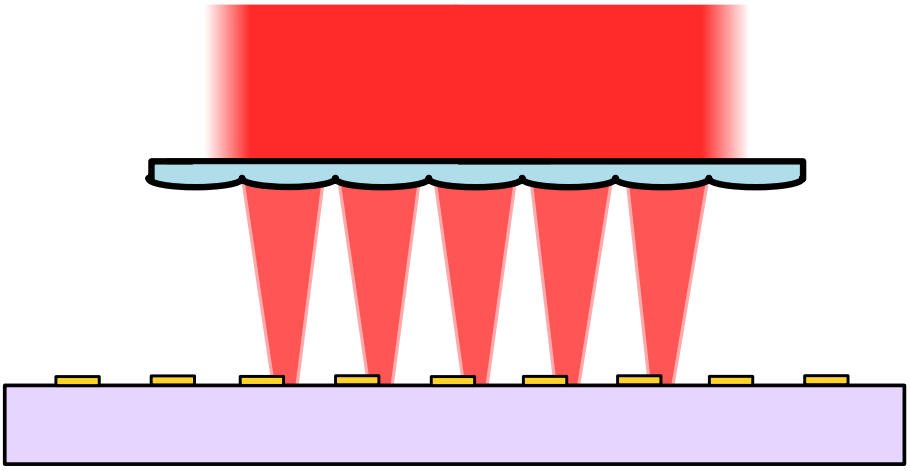

Figure 5.1: Illustration of the single metal stripline LPD multiplex emitter and focusing optics.

LPD emitter and the emission will constructively interfere in the far field producing a plane wave pulse of THz radiation. This emitter design has the benefit of being very simple to fabricate, however, the focusing optic makes the alignment of the emitter more complex than a single LPD emitter or PC antenna.
The second multiplex LPD emitter design consists of strip-lines made from two different metals deposited on a semiconductor substrate. On the surface of the semiconductor first gold strip-lines are deposited. Once deposited another deposition is done placing another strip-line made from thinner layer of metal next to each gold strip line. When illuminated the different thickness and or types of metal will suppress the emission by a different amount on either side of each strip-line giving the asymmetry needed for THz emission perpendicular to the surface. Figure 5.2 shows a schematic of this emitter design. For this emitter the entire device is illuminated and no focusing optics are required. This design is harder to fabricate but alignment is simpler.

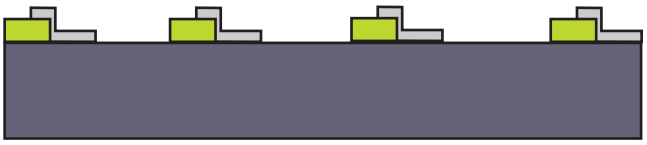

Figure 5.2: Illustration of the double metal strip-line LPD multiplex emitter

5.3 Experimental Method and Results

5.3.1 Single Metal Multiplex LPD Emitter Array

The single strip multiplex emitters were fabricated and tested in collaboration with Paul Gow. Two single metal multiplex LPD emitters were fabricated by photo-lithography where 100 nm thick strips of gold were evaporated onto the surface of GaAs substrates. One of the emitters comprised of 200 μm period gold strips on a SI-GaAs substrate. The other emitter fabricated had 15 μm period gold strips deposited on a LT-GaAs substrate. The setup for this experiment was a typical THz-TDS but with a modification of using a lenticular micro-lens array for the focusing optics onto the multiplex emitters. PC and single strip-line PD emitters emit as point sources and thus a hyper-hemispherical silicon lens is used to help guide the THz radiation into the parabolic mirrors of the spectrometer. Emitter arrays on the other hand emit over the whole structure which is much larger than the THz central wavelength and thus emit a plane wave making the Si lens unnecessary. The multiple foci produced by the lens array were aligned against correlating gold edges on the emitter, which was positioned at the focal distance from the lens. A schematic of this modified setup is shown in Figure 5.3.

The THz emission from both emitters were measured for different optical powers. The results from these emitters are shown in Fig. 5.4 and compared with a single edge emitter fabricated on LT-GaAs using a single cylindrical lens for focusing. The results show that the 15 μm period multiple emitter fabricated on LT-GaAs exhibits a greater increase in peak-to-peak power of emitted THz radiation in comparison with a single emitter and the 200 μm period array fabricated on SI-GaAs. This result is in agreement with the work presented in Chapter 4 and [89] where I showed that LT-GaAs performs better than SI-GaAs. The presence of the Si-lens for the single edge makes makes a true comparison with the multiplex emitters difficult. It is also hard to compare the multiplex emitters fabricated on the SI-GaAs sample as the single emitter is on LT-GaAs. The average output power from LT-GaAs multiple emitters was found to be 5.2 times greater than that from the single emitter also on LT-GaAs. The sample measurements were also unsaturated meaning we can expect to get more power from this devices before roll-over.

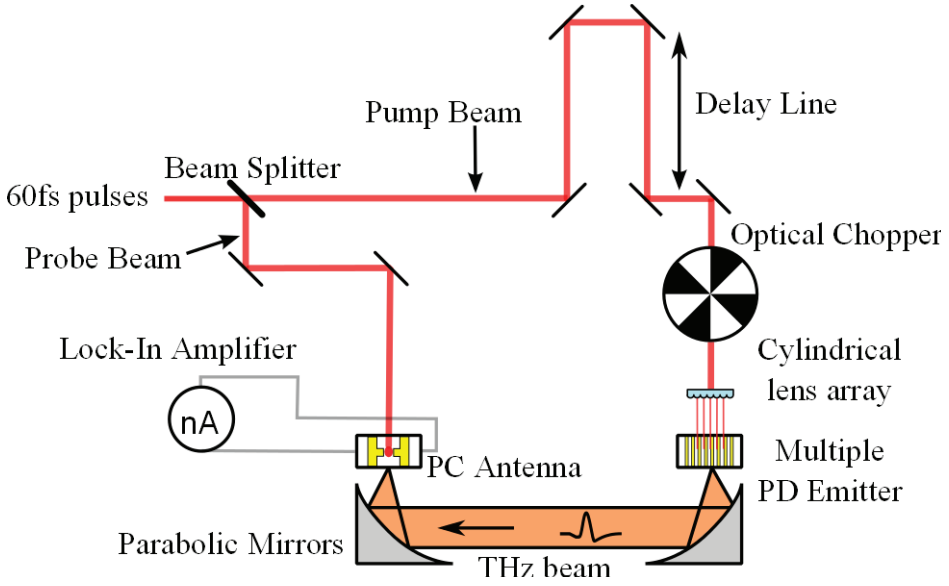

Figure 5.3: Illustration of the experimental setup for testing multiplex LPD emitters with a typical THz THS system.

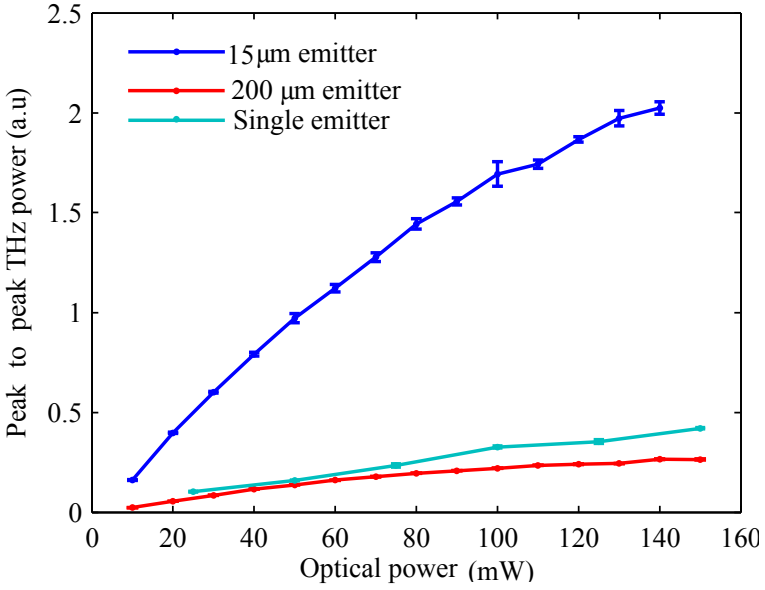

Figure 5.4: Graph of peak-to-peak THz power as a function of optical power for three different emitters.

Figure 5.5 show the peak to peak amplitude of the detected THz radiation from the two single metal LPD multiplex emitters. The results for the LT-GaAs emitter are shown in the main figure and the results of the SI-GaAs are shown in the insert. The number of foci produced by each micro-lens array that fell within the $1/e^2$ spot radius was calculated. This allowed us to estimate the number of gold strips we were illuminating

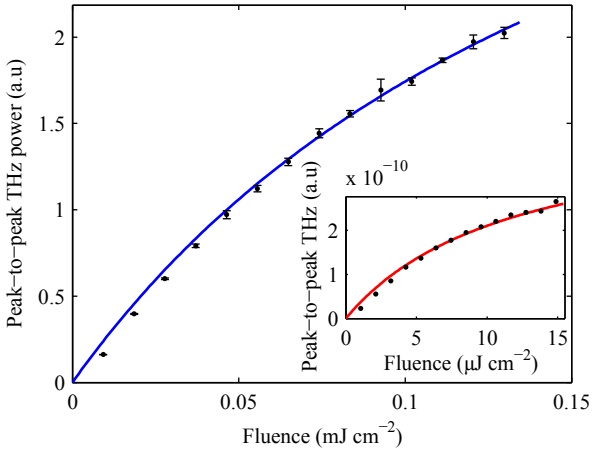

Figure 5.5: Peak to peak amplitude of the detected THz for the 15 μm period LT-GaAs multiple emitters plotted as a function of fluence. The inset shows the same but for the 200 μm period SI-GaAs emitters. The solid lines represent saturation curve fits.

on each array. We illuminated 7 and 82 strips for the 200 μm and 15 μm period arrays respectively. The fluence was found by estimating the area of illumination for each focus and the percentage of total power focussed into each area. The saturation curve that was fitted was the same used in Chapter 4 and [2]. The formula for the curve is, $E_{\mathrm{THz}}(F) = A\omega F/(F + F_{\mathrm{sat}})$, where A is a coefficient of conversion and alignment efficiency, ω is the $1/\mathrm{e}^2$ spot radius and F_{sat} is the saturation fluence. The average saturation fluence for LT-GaAs was found to be $F_{\mathrm{sat}} = 0.18$ mJ/cm^2, and for SI-GaAs $F_{\mathrm{sat}} = 12$ μJ/cm^2. These values are consistent with the work from previous chapters and [2].

For a comparison of bandwidth and power, scans were made with the 15 μm period multiple emitter illuminated with 100 mW pump power. The emitter was then replaced with a Menlo systems PC antenna which was aligned with a hyper-hemispherical Si-lens. Time domain scans were taken with the emitter biased at 5 V and both detector and emitter optical powers at 5 mW. Figure 5.6 shows the time-domain scans and frequency spectra of this. The multiple emitter shows comparable bandwidth to a PC antenna, spanning 3 THz and exhibiting similar power. This work on single metal multiplex LPD emitters has been submitted for publication in November 2013, shortly before the submission of this thesis.

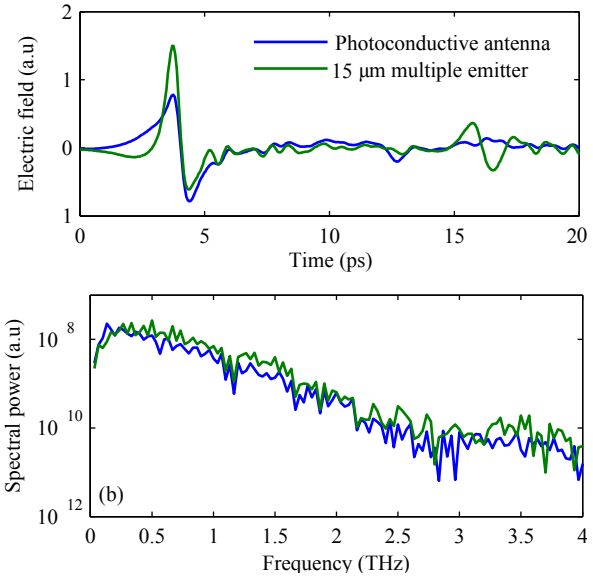

Figure 5.6: Comparison of power, (a), and bandwidth, (b), between the 15 μm period multiple emitter and a Menlo systems PC antenna. The Menlo systems antenna was biased at 5 V with both detector and emitter optical power at 5 mW. The 15 μm period multiple emiiter was illuminated with optical power of 100 mW.

5.3.2 Double Metal Multiplex LPD Emitter Array

The double metal LPD multiplex emitters were fabricated and tested in collaboration with Duncan McBryde. Although single metal LPD multiplex emitters are simple to fabricate it is difficult to align the required focusing optics. An alternative multiplex LPD emitter design was also envisioned where no focusing optics are required. The antenna design is that of metal strip lines where each strip line is made from two different metals at different thickness next to each other. A schematic of this has already been shown in Fig. 5.2. The metals and their thickness is chosen such that they are both thick enough to block the optical pump laser while one of the metals is thin enough to allow for transmission of THz radiation and thus reducing the dipole suppression on just one side of each strip line giving the needed asymmetry for THz emission perpendicular to the surface.

The skin depth for Au at 1 THz is 80 nm [95] where as Pb has a skin depth of 238 nm at 1 THz. And bellow 24 nm Pb is completely transparent at 1 THz [96]. Figure 5.7 shows the calculated skin depths for Au and Pb using the refractive indices form the tables in [95, 97]. For our device we chose to use 100 nm of Au and 60 nm of Pb to form our double metal LPD multiplex emitters. The emitters were fabricated by Duncan McBryde using the metal and thicknesses I had determined. The double metal

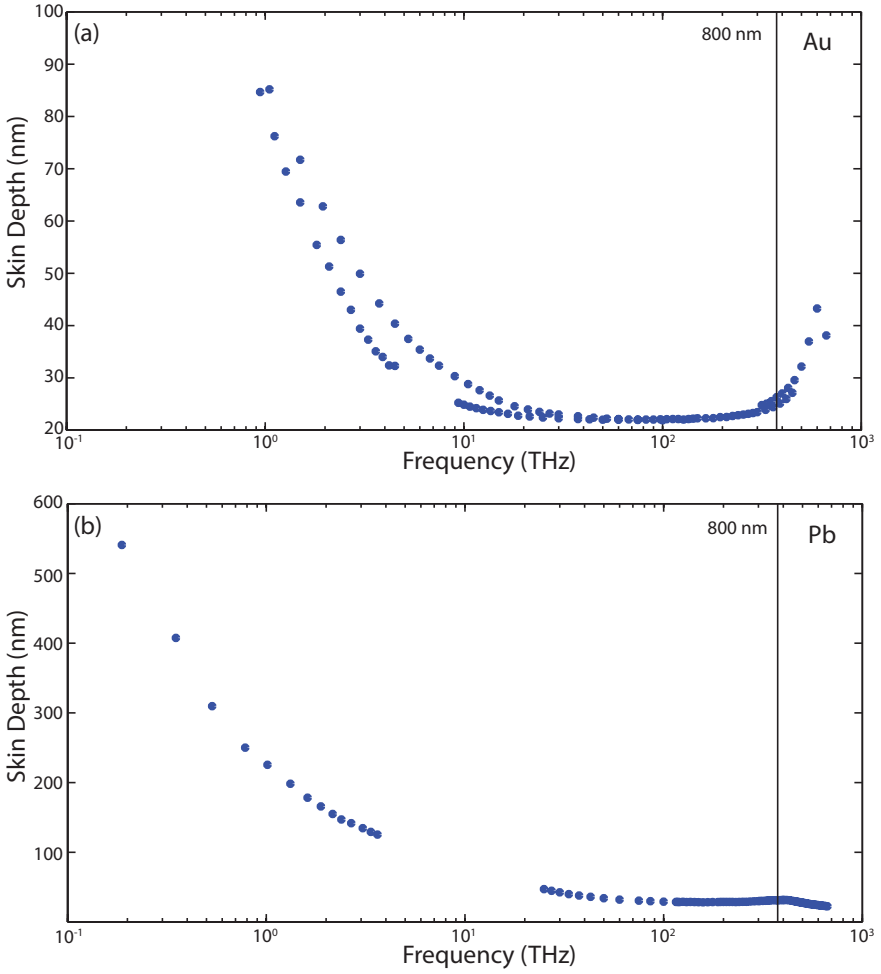

Figure 5.7: Skin depth of (a) Au and (b) Pb as a function of frequency

array of strip lines were 4 μm wide with a period of 15 μm and deposited by doing two photo-lithographic and deposition runs. The substrate used first was Si-GaAs due to abundance of this material in our supply and limited supply of LT-GaAs. Figure 5.8 shows a photograph of our double metal strip lines under a microscope. The two metals can be seen and the overlap is clearly visible. The emitter was tested in a typical THz-TDS similar to that shown in Fig. 5.3 but without the focusing optics for the emitter. An example of the THz emission from the emitter is shown in Fig. 5.9. The emitter again was tested for different pump powers to measure its efficiency. The unfocused laser spot size had a radius of 0.52 mm allowing for the total fluence to be calculated. Figure 5.10 shows the peak to peak amplitude of the THz emission as a function of fluence. Using the saturation curve fitting as already described; the saturation fluence for this device was found to be 1.1 μJ/cm^2.

At the time of writing this the fabrication and testing of double metal LPD emitter on LT-GaAs is under way and being tested by Duncan McBryde. We are also in

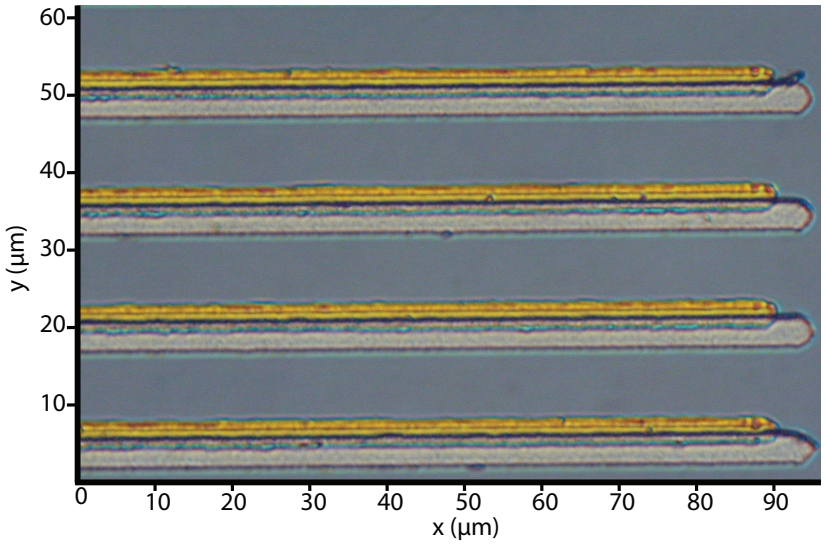

Figure 5.8: Image of the fabricated double metal emitter showing the overlap of the Au and Pb strip lines.

the processes of producing multiplex emitters with an insulating layer to eliminate contributions for Schottky contacts. If the LPD effect is the predominant emission mechanism for multiplex emitters then it is expected that the LT-GaAs will outperform the SI-GaAs. If however the difference between Schottky barriers for the two different metals is more important then the SI-GaAs emitters may out perform LT-GaAs emitters as SI-GaAs has less surface defects. A paper for this work is also in preparation.

5.4 Conclusion

LPD emitters are more robust and simpler to fabricate than PC emitters however they are not as efficient. These emitters however are scalable and arrays of emitters are simple to fabricate on a single device. Here I have presented two different multiplex emitter designs that exploit LPD emission. Both emitters have been fabricated and tested showing that they are comparable to commercial photoconductive emitters in both power and bandwidth. One emitter was made from single metal strip lines and a micro cylindrical lens array and the other was a double metal strip line design that does not need focusing optics. Both devices perform better than single LPD emitters on the same substrate.

These emitter designs hold promise that LPD emitters are commercial attractive as an alternative to PC emitters and are also easier to fabricate and more robust than multiplex PC emitters. The work in this chapter is on going within our group and the devices will be tested on more substrates and strip line parameters.

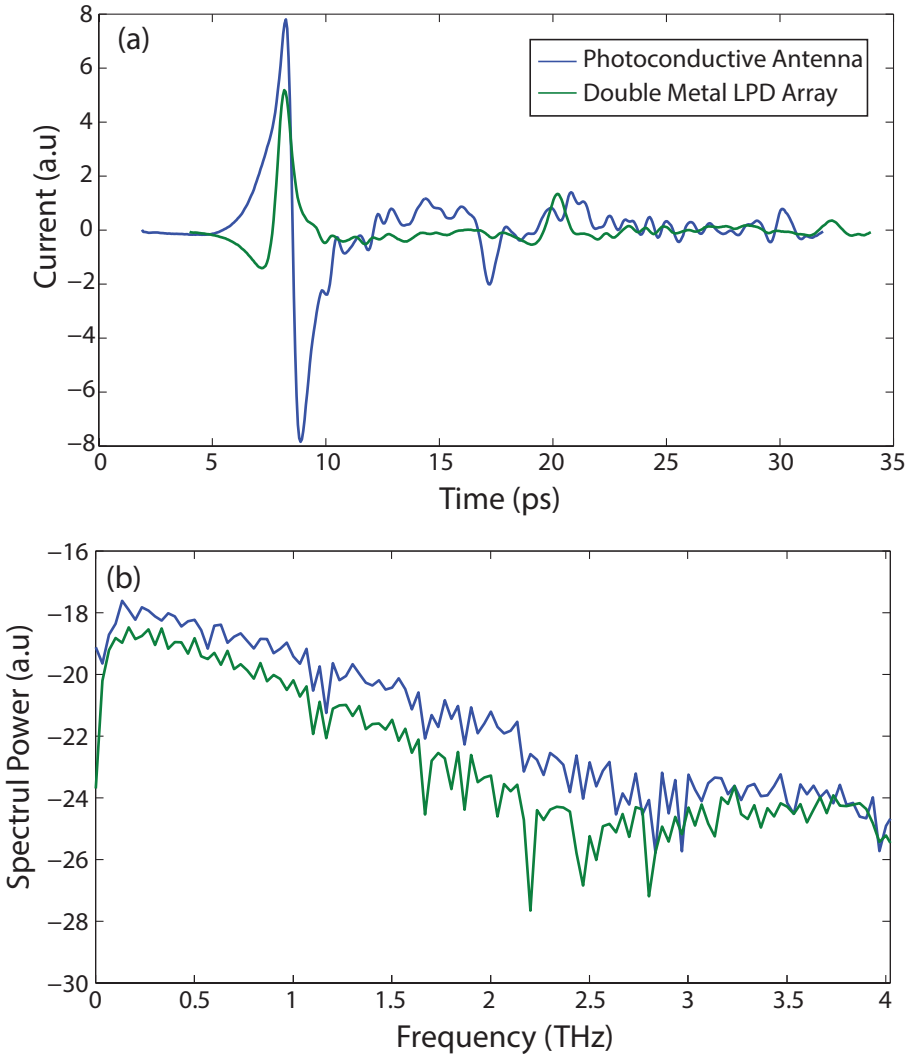

Figure 5.9: THz TDS scan of THz emission from a double metal LPD multiplex emitter on SI-GaAs

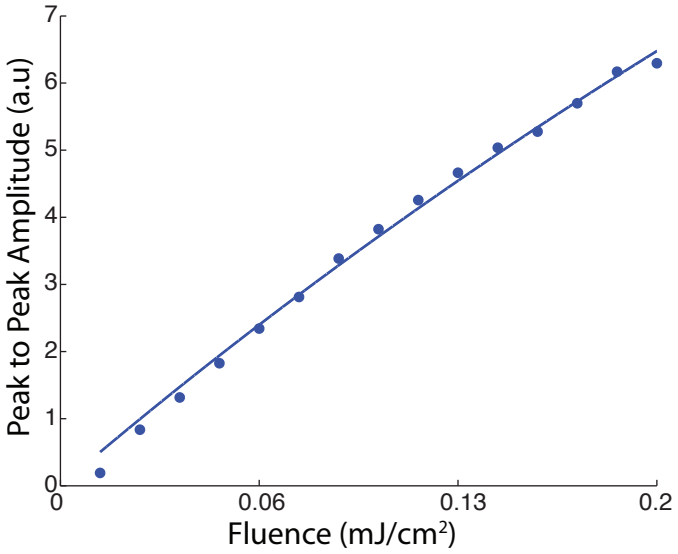

Figure 5.10: Peak to peak amplitude of THz emission from a double metal LPD multiplex emitter on SI-GaAs

Chapter 6

Conclusion

The work presented in this thesis focuses on the development of a novel mechanism for generating single cycle pulses of THz radiation based on lateral diffusion currents and dipole suppression. The work was initially inspired by the work of Klatt et. al. [1, 54, 55] who demonstrated novel THz emitters that utilised ultrafast lateral diffusion currents inside their devices. I was able to replicate their results with similar success however was unsure of the proposed origin of the detected THz radiation. They attributed the THz emission to be from lateral diffusion currents that form due to an initial asymmetrical carrier distribution produced on the surface of the semiconductor due to partial masking of the excitation pump. Computer simulations however were unable to predict the emission from lateral diffusion currents alone suggesting that the theory of the mechanism was incomplete. In this thesis detailed arguments of why their interpretation was incomplete and an addition to the theory was proposed that takes into account dipole suppression from the metal mask giving the needed asymmetry.

In this thesis I first presented numerical and Monte Carlo simulations of carrier transport within 1D semiconductor devices during and after ultrafast carrier excitation for asymmetrical excitation spots. In both simulations THz emission was not predicted for asymmetrical carrier excitation alone. By suppressing the dipole under the masked region it was demonstrated that THz emission would be expected from both simulations. Diffusion components of the carrier transport was shown to be more important than any drift components from restoring field after charge separation during the time frame of THz generation.

Next I further explored the suppression of dipoles near the metal mask. First an exact analytical solution to the problem of the detected electric field far from a point dipole near a semi-infinite perfect conductor. The solution was similar to the Sommerfeld diffraction problem [76] and demonstrated a very strong dipole suppression when the

emitting dipole is placed much less than a wavelength under the perfect conductor but is not suppressed when away from the perfect conductor. The geometry of the device was also simulated with a COMSOL model that used results from the numerical drift-diffusion model and demonstrated that we would only expect THz emission propagating perpendicular to the surface when the metal mask is present regardless of the symmetry of the initial carrier concentration.

The new theory of THz emission from these devices presented here made a prediction that the sign of THz emission would have the opposite polarity in contrast if the emission was from an asymmetrical carrier concentration alone. In this work and in [60] experimental evidence is given that shows that the sign of the detected THz emission is in agreement with the dipole quenching interpretation. Further experiments were conducted to explore and characterise THz emission from these devices. By applying an external electric field across a LPD emitter the emission was shown to either be enhanced or completely suppressed by the electric field. The importance of the proximity of carrier population to the metal mask was explored by imaging a knife edge on to bare semiconductor forming a semicircular spot and then translating the metal mask under the shadowed region. When the metal mask approached the sharp edge of the laser spot the detected THz emission was greatly enhanced. To eliminate contributions from Schottky barrier potentials near the metal:semiconductor interface a sample with an insulating layer was fabricated and I demonstrated no lose in THz emission was observed.

The pump parameters and different substrates were tested and if was found that unannealed LT-GaAs performed better that annealed LT-GaAs which in turn performed better than SI-GaAs despite its higher mobility. These experiments revealed that fast trapping of the carriers not only increased the saturation fluence but also increased the efficiency of the devices.

Finally I presented and demonstrated two different multiplex LPD emitter arrays that both produced THz emission that is comparable to commercial PC emitters in terms of both power and bandwidth. The first was based on an array of single metal strip lines and a micro cylindrical lens array. The other was based on an array of strip lines made from two different metals that requires no focusing optics. Both devices are easier to fabricate and more robust than multiplex PC emitters.

Further work on the multiplex emitters is being conducted to see how they work on different substrates and with different strip line parameter. In order to be sure if the THz emission is again due to diffusion currents and not Schottky barriers imbalance multiple emitters will be fabricated with insulating layers. Other ideas for future work on LPD emitters is to use nano structures to form plasmonic emitters to enhance the carrier concentrations near the interface. The multiplex LPD emitters may also be able to produce steerable THz emission by placing delays for the optical pulse on different

strip-lines of the emitter. As the emitters do not need to be biased and are simple to fabricate they may also be integrated with on-chip THz technologies such as wave guides and amplifiers.

Appendix A

Journal and Conference publication during this thesis

M. E. Barnes, Z. Mihoubi, K. G. Wilcox, A. H. Quarterman, I. Farrer, D. A. Ritchie, A. Garnache, S. Hoogland, V. Apostolopoulos, and A. C. Tropper. "Gain bandwidth characterization of surface-emitting quantum well laser gain structures for femtosecond operation.", *Optics Express, 18(20), 2010*

Duncan McBryde, **Mark E. Barnes**, Geoff J. Daniell, Aaron L. Chung, Zakaria Mihoubi, Adrian H. Quarterman, Keith G. Wilcox, Anne C. Tropper, Vasilis Apostolopoulos School. "Simulation of metallic nanostructures for emission of THz radiation using the lateral photo-Dember effect". *2011 International Conference on Infrared, Millimeter, and Terahertz Waves*

M. E. Barnes, D. McBryde, G. J. Daniell, G. Whitworth, A. L. Chung, A. H. Quarterman, K. G.Wilcox, A. Brewer, H. E. Beere, D. A. Ritchie, and V. Apostolopoulos. "Terahertz emission by diffusion of carriers and metal-mask dipole inhibition of radiation.", *Optics Express, 20(8), 2012*

M. E. Barnes, S. A. Berry, P. Gow, D. McBryde, G. J. Daniell, H. E. Beere, D. A. Ritchie, V. Apostolopoulos. "Investigation of the role of the lateral photo-Dember effect in the generation of terahertz radiation using a metallic mask on a semiconductor", *Optics Express, 21(14), 2013*

Mark E. Barnes, Duncan McBryde, Sam A. Berry, Pual C. Gow, Geoff J. Daniell, Harvey E. Beere, David A. Ritchie, Vasilis Apostolopoulos. "Terahertz Emission From

Lateral Surge Currents And Suppression Of dipoles Under A Metal Mask.", *2013 International Conference on Infrared, Millimeter, and Terahertz Waves*

Mark E. Barnes, Duncan McBryde, Paul C. Gow, Sam A. Berry, Geoff J. Daniell, Harvey E. Beere, David A. Ritchie, Vasilis Apostolopoulos. "Investigation Into The Role Of The Metal Mask And Pump Laser Illumination Parameters For Lateral Photo-Dember Emitters.", *2013 International Conference on Infrared, Millimeter, and Terahertz Waves, 2013*

Duncan McBryde, **Mark E. Barnes**, Paul C. Gow, Sam A. Berry, Geoff J. Daniell, Harvey E. Beere, David A. Ritchie, Vasilis Apostolopoulos. "Characterisation Of Low Tempreture And Semi-insulating GaAs Lateral photo-Dember THz Emitters.", *2013 International Conference on Infrared, Millimeter, and Terahertz Waves, 2013*

Aaron L. Chung, **Mark E. Barnes**, Sam A. Berry, Duncan McBryde, Geoff J. Daniell, Axel Zeitler, Vasilis Apostolopoulos. "Angular profile determination of THz-TDS.", *2013 International Conference on Infrared, Millimeter, and Terahertz Waves, 2013*

P. Gow, S. A. Berry, D. McBryde, **M. E. Barnes**, H. E. Beere, D. A. Ritchie, and V. Apostolopoulos. "Multiple lateral photo-Dember terahertz emitters illuminated by a cylindrical micro-lens array." *submitted to Applied Physics Letters, 2013*

D. McBryde, **M. E. Barnes**, S. A. Berry, P. Gow, H. E. Beere, D. A. Ritchie, V. Apostolopoulos. "Saturation and polarisation dependence of GaAs based Lateral Photo-Dember terahertz emitters" *submitted to Optics Express, 2013*

References

[1] G. Klatt, F. Hilser, W. Qiao, M. Beck, R. Gebs, A. Bartels, K. Huska, U. Lemmer, G. Bastian, M. B. Johnston, M. Fischer, J. Faist, and T. Dekorsy, "Terahertz emission from lateral photo-Dember currents," *Optics express*, vol. 18, pp. 4939–47, Mar. 2010.

[2] M. E. Barnes, S. A. Berry, P. Gow, D. McBryde, G. J. Daniell, H. E. Beere, D. a. Ritchie, and V. Apostolopoulos, "Investigation of the role of the lateral photo-Dember effect in the generation of terahertz radiation using a metallic mask on a semiconductor," *Optics express*, vol. 21, pp. 16263–72, July 2013.

[3] P. H. Siegel, "Terahertz technology," *IEEE Trans. Microwave Theory Tech.*, vol. 50, 2002.

[4] T. G. Phillips and J. Keene, "Submillimeter astronomy [heterodyne spectroscopy]," *Proceedings of the IEEE*, vol. 80, pp. 1662–1678, 1992.

[5] J. C. Wiltse, "History of millimeter and submillimeter waves," *IEEE Trans. Microwave Theory Tech.*, vol. 32, pp. 1119–1127, 1984.

[6] D. Grischkowsky, S. Keiding, M. V. Exter, and C. Fattinger, "Far-infrared time-domain spectroscopy with terahertz beams of dielectrics and semiconductors," *Journal of the Optical Society of America B*, vol. 7, no. 10, pp. 2006–2015, 1990.

[7] Q.-L. Zhou, Y. Shi, T. Li, B. Jin, D. Zhao, and C. Zhang, "Carrier dynamics and terahertz photoconductivity of doped silicon measured by femtosecond pump-terahertz probe spectroscopy," *SCIENCE CHINA Physics,Mechanics and Astronomy*, vol. 52, no. 12, p. 4, 2009.

[8] H. P. Porte, P. U. Jepsen, N. Daghestani, E. U. Rafailov, and D. Turchinovich., "Ultrafast release and capture of carriers in InGaAs/GaAs quantum dots observed by time-resolved terahertz spectroscopy," *Applied Physics Letters*, vol. 94, no. 26, p. 262104, 2009.

[9] A. D. Jameson, J. L. Tomaino, Y. S. Lee, J. P. Prineas, J. T. Steiner, M. Kira, and S. W. Koch, "Transient optical response of quantum well excitons to intense narrowband terahertz pulses," *Applied Physics Letters*, vol. 95, no. 20, p. 201107, 2009.

[10] M. C. Beard, G. M. Turner, and C. A. Schmuttenmaer., "Size-Dependent Photoconductivity in CdSe Nanoparticles as Measured by Time-Resolved Terahertz Spectroscopy," *Nano Letters*, vol. 2, no. 9, pp. 983–987, 2002.

[11] N. Nagai, M. Sumitomo, M. Imaizumi, and R. Fukasawa, "Characterization of electron- or proton-irradiated Si space solar cells by THz spectroscopy," *Semiconductor Science and Technology*, vol. 23, no. 22, pp. 201–209, 2006.

[12] D. H. Auston, "Picosecond optoelectronic switching and gating in silicon," *Applied Physics Letters*, vol. 26, no. 3, pp. 101–103, 1975.

[13] C. H. Lee, "Picosecond optoelectronic switching in GaAs," *Applied Physics Letters*, vol. 30, no. 2, p. 84, 1977.

[14] T. Yajima and N. Takeuchi, "Spectral Properties and Tunability of Far-Infrared Difference-Frequency Radiation Produced by Picosecond Laser Pulses," *Japanese Journal of Applied Physics*, vol. 10, pp. 907–915, 1970.

[15] K. H. Yang, P. L. Richards, and Y. R. Shen, "Generation of Farinfrared Radiation by Picosecond Light Pulses in LiNbO3," *Applied Physics Letters*, vol. 19, no. 9, p. 320, 1971.

[16] P. Auston, DH and Cheung, KP and Smith, "Picosecond photoconducting Hertzian dipoles," *Applied Physics Letters*, vol. 45, no. 3, pp. 284–286, 1984.

[17] D. H. Auston, K. P. Cheung, and D. A. Kleinman, "Cherenkov Radiation from Femtosecond Optical Pulses in Electro-Optic Meida," *Physical Review Letters*, vol. 53, no. 16, pp. 1555–1558, 1984.

[18] D. H. Auston and K. P. Cheung, "Coherent time-domain far-infrared spectroscopy," *Journal of the Optical Society of America B*, vol. 2, no. 4, pp. 606–612, 1985.

[19] A. P. DeFonzo, M. Jarwala, and C. Lutz, "Transient response of planar intergrated optoelectronic antennas," *Applied Physics Letters*, vol. 50, no. 17, p. 1155, 1987.

[20] A. P. DeFonzo and C. Lutz, "Optoelectronic tranmission and reception of ultrashort electrical pulses," *Applied Physics Letters*, vol. 51, no. 4, p. 212, 1987.

[21] M. van Exter, C. Fattinger, and D. Grischkowsky, "High-brightness terahertz beams characterized with an ultrafast detctor," *Applied Physics Letters*, vol. 55, no. 4, p. 337, 1989.

[22] D. E. Spence, P. N. Kean, and W. Sibbett, "60-fsec pulses generation from a self-mode-locked Ti:sapphire laser," *Optics Letters*, vol. 16, no. 1, pp. 42–44, 1991.

[23] Q. Wu and X. C. Zhang, "Free-space electro-optic sampling of terahertz beams," *Applied Physics Letters*, vol. 67, no. 24, p. 3523, 1995.

[24] D. M. Mittleman, R. H. Jacobsen, and M. C. Nuss, "T-ray imagaing," *IEE Journal of Selected Topics In Quantum Electronics*, vol. 2, p. 3, 1996.

[25] M. Tonouchi, "Cutting-edge terahertz Technology," *Nature Photonics*, vol. 77, p. 1396, 2007.

[26] B. B. Hu and M. C. Nuss, "Imaging with terahertz waves," *Optics Letters*, vol. 20, no. 16, p. 1716, 1995.

[27] P. F. Taday, I. V. Bradley, D. D. Arnone, and M. Pepper, "Using terahertz pulse spectroscopy to study the cryastalline structure of a drug: A case study of the polymorphs of ranitidine hydrochloride," *Journal of Pharmaceuticals Science*, vol. 92, no. 4, pp. 831–838, 2003.

[28] D. Crawley, C. Longbottom, V. P. Wallace, B. Cole, D. Arnone, and M. Pepper, "Three-dimensional terahertz pulse imaging of dental tissue," *Journal of Biomedical Optics*, vol. 8, no. 2, pp. 303–307, 2003.

[29] R. M. Woodward, V. P. Wallace, D. D. Arnone, E. H. Linfield, and M. Pepper, "Terahertz pused imaging of skin cancer in the time and frequency domain," *Journal of Biological Physics*, vol. 29, no. 2-3, pp. 257–259, 2003.

[30] V. P. Wallace, A. J. Fitzgerald, S. Shankar, N. Flanagan, R. Pye, J. Cluff, and D. D. Arnone, "Terahertz pulsed imaging of basal cell carcinoma ex vivo and in vivo," *British Journal of Dermatology*, vol. 151, no. 2, pp. 424–432, 2004.

[31] A. Welch, "Full-Body Scanners: Full Protection from Terrorist Attacks or Full-On Violation of the Constitution?," *Transportation Law Journal*, vol. 37, no. 167, 2010.

[32] A. W. M. Lee, B. S. Williams, S. Kumar, Q. Hu, and J. L. Reno, "Real-time imaging using a 4.3- THz quantum cascade laser and a 320 240 Microbolometer Focal-Plane Array," *IEEE Photonics Technology Letters*, vol. 18, no. 13, 2006.

[33] H. Zhong, J. Xu, X. Xie, T. Yuan, R. Reightler, E. Madaras, and X.-C. Zhang, "Nondestructive defect identification with terahertz time-of-flight tomography," *IEEE Sensors Journal*, vol. 5, no. 2, pp. 203–208, 2005.

[34] N. Nagai and R. Fukasawa, "Abnormal dispersion of polymer films in the THz frequency," *Chemical Physics Letters*, vol. 338, no. 4-6, pp. 479–482, 2004.

[35] N. Nagai, T. Imai, R. Fukasawa, K. Kato, and K. Yamauchi, "Analysis of the intermolecular interaction of nanocomposites by THz spectroscopy," *Applied Physics Letters*, vol. 85, no. 18, p. 4010, 2004.

[36] M. Misra, K. Kotani, I. Jawayama, H. Murakami, and M. Tonouchi, "Observation of TO1 soft mode in SrTiO3 fi lms by terahertz time domain spectroscopy," *Applied Physics Letters*, vol. 87, no. 18, p. 182909, 2005.

[37] J. Yu, X. Li, and N. Chi, "Faster than fiber: over 100-Gb/s signal delivery in fiber wireless intergration system," *Optics Express*, vol. 21, no. 19, p. 22885, 2013.

[38] D. Pinna, M. Galeotti, and R. Mazzeo, *Scientific Examination for the Investigation of Paintings: A Handbook for Conservator-Restorers*. Centro Di, Firenze, 2009.

[39] K. Fukunaga, I. Hosako, M. Picollo, and Y. Kohdzuma, "Application of THz Sensing to Analysis of Works of Art for Conservation," in *Microwave Photonics (MWP), 2010 IEEE Topical Meeting on*, pp. 147–150, 2010.

[40] J. B. Jackson, M. R. Mourou, J. F. Whitaker, I. N. Duling, S. L. Williamson, M. Menu, and G. A. Mourou, "Terahertz time-domain reflectometry applied to the investigation of hidden mural paintings," in *Conference on Quantum Electronics and Laser Science. CLEO/QELS*, 2008.

[41] S. Hauser, "What Lies Beneath?." http://www.rochester.edu/pr/Review/V75N6/0403_terahertz.html, July-Aug 2013.

[42] L. Duvillaret, F. Garet, and J.-L. Coutaz, "A reliable method for extraction of material parameters in terahertz time-domain spectroscopy," *Selected Topics in Quantum Electronics, IEEE Journal of*, vol. 2, no. 3, pp. 739 – 746, 1996.

[43] L. Duvillaret, F. Garet, and J.-L. Coutaz, "Highly Precise Determination of Optical Constants and Sample Thickness in Terahertz Time-Domain Spectroscopy," *Applied Optics*, vol. 38, no. 2, pp. 409–415, 1999.

[44] T. D. Dorney, R. G. Baraniuk, and D. M. Mittleman, "Material parameter estimation with terahertz time-domain spectroscopy," *Journal of the Optical Society of America A*, vol. 18, p. 1562, July 2001.

[45] A. L. Chung, G. J. Daniell, A. H. Quarterman, K. G. Wilcox, H. E. Beere, D. A. Ritchie, A. C. Tropper, and V. Apostolopoulos, "Material parameter extraction in THz-TDS using a converging beam transfer function," in *Infrared Millimeter and Terahertz Waves (IRMMW-THz), 2010 35th International Conference on*, pp. 1–2, 2010.

[46] P. U. Jepsen, D. G. Cooke, and M. Koch, "Terahertz spectroscopy and imaging - Modern techniques and applications," *Laser & Photon. Rev.*, vol. 5, no. 1, pp. 124–166, 2011.

[47] P. U. Jepsen, R. H. Jacobsen, and S. R. Keiding, "Generation and detection of terahertz pulses from biased semiconductor antennas," *Journal of the Optical Society of America B*, vol. 13, p. 2424, Nov. 1996.

[48] L. Duvillaret, F. Garet, J.-F. Roux, and J.-L. Coutaz, "Analytical modeling and optimization of terahertz time-domain spectroscopy experiments, using photoswitches as antennas," *IEEE Journal of Selected Topics in Quantum Electronics*, vol. 7, pp. 615–623, 2001.

[49] V. Malevich, R. Adomavicius, and A. Krotkus, "THz emission from semiconductor surfaces," *Comptes Rendus Physique*, vol. 9, no. 2, pp. 130–141, 2008.

[50] M. B. Johnston, D. Whittaker, A. Corchia, A. G. Davies, and E. Linfield, "Simulation of terahertz generation at semiconductor surfaces," *Physical Review B*, vol. 65, pp. 165301–8, Mar. 2002.

[51] K. Liu, J. Z. Xu, T. Yuan, and X. C. Zhang, "Terahertz radiation from InAs induced by carrier diffusion and drift," *Physical Review B*, vol. 73, no. 15, p. 155330, 2006.

[52] P. Gu, M. Tani, S. Kono, K. Sakai, and X. C. Zhang, "Study of terahertz radiation from InAs and InSb," *Journal of Applied Physics*, vol. 91, no. 9, pp. 5533–7, 2002.

[53] A. Reklaitis, "Crossover between surface field and photo-Dember effect induced terahertz emission," *J. Appl. Phys*, vol. 109, no. 8, pp. –, 2011.

[54] G. Klatt, F. Hilser, W. Chao, R. Gebs, A. Bartels, K. Huska, U. Lemmer, G. Bastian, M. B. Johnston, M. Fischer, J. Faist, and T. Dekorsy, "Intense terahertz generation based on the photo-Dember effect," *OSA / CLEO / QELS 2010*, 2010.

[55] G. Klatt, B. Surrer, D. Stephan, O. Schubert, M. Fischer, J. Faist, A. Leitenstorfer, R. Huber, and T. Dekorsy, "Photo-Dember terahertz emitter excited with an Er:fiber laser," *Applied Physics Letters*, vol. 98, no. 2, 2011.

[56] G. Klatt, D. Stephan, M. Beck, J. Demsar, and T. Dekorsy, "Large-area laser-driven terahertz emitters," *Electronics Letters*, vol. 46, no. 26, p. S24, 2010.

[57] W. Qiao, D. Stephan, M. Hasselbeck, Q. Liang, and T. Dekorsy, "Low-temperature THz time domain waveguide spectrometer with butt-coupled emitter and detector crystal," *Optics Express*, vol. 20, p. 19769, Aug. 2012.

[58] D. McBryde, M. E. Barnes, A. L. Chung, Z. Mihoubi, G. J. Daniell, A. H. Quarterman, K. G. Wilcox, H. E. Beere, D. A. Ritchie, A. C. Tropper, and V. Apostolopoulos, "Simulation of metallic nanostructures for emission of THz radiation using the lateral photo-Dember effect," in *IRMMW-THz 2011*, (Houston, Texas), pp. 1–2, IEEE, Oct. 2011.

[59] K. H. Drexhage, "Influence of a dielectric interface on fluorescence decay time," *Journal of Luminescence*, vol. 1,2, pp. 693–701, 1970.

[60] M. E. Barnes, D. Mcbryde, G. J. Daniell, G. Whitworth, A. H. Quarterman, K. G. Wilcox, A. Brewer, H. E. Beere, D. A. Ritchie, and V. Apostolopoulos, "Terahertz emission by diffusion of carriers and metal-mask dipole inhibition of radiation," *Optics express*, vol. 20, no. 8, pp. 1–2, 2012.

[61] T. Dekorsy, T. Pfeifer, W. Kütt, and H. Kurz, "Subpicosecond carrier transport in GaAs surface-space-charge fields," *Physical review. B, Condensed matter*, vol. 47, pp. 3842–3849, Feb. 1993.

[62] I. S. Gregory, W. R. Tribe, C. Baker, B. E. Cole, M. J. Evans, L. Spencer, M. Pepper, and M. Missous, "Continuous-wave terahertz system with a 60 dB dynamic range," *Applied Physics Letters*, vol. 86, no. 20, p. 204104, 2005.

[63] I. S. Gregory, "The development of a continuous-wave terahertz imaging system," *PhD Thesis, University of Cambridge*, no. December, 2004.

[64] C. Baker, "Development of Semiconductor Materials for Terahertz Photoconductive Antennas," *PhD Thesis, University of Cambridge*, 2004.

[65] C. Jacoboni and P. Lugli, *The Monte Carlo Method for Semicon- ductor Device Simulation.* Springer-Verlag, New York, 1989.

[66] C. Jacoboni and L. Reggiani, "The Monte Carlo method for the solution of charge transport in semiconductors with applications to covalent materials," *Reviews Of Modern Physics*, vol. 55, no. 3, pp. 645–705, 1983.

[67] D. Vasileska, K. Raleva, and S. M. Goodnick, *Applications of Monte Carlo Method in Science and Engineering.* InTech, 2011.

[68] S. M. G. C. R. S. S. A. N. A. A. H. R. H. A. A. B. P. Dragica Vasileska, Katerina Raleeva, *Nanohub Resource on Monte Carlo Device Simulation Study*, ch. Monte Carlo Device Simulations, pp. 1–76. Nanohub Research Profeesionals, 2011.

[69] T. Kuhn and F. Rossi, "Monte Carlo simulation of ultrafast processes in photoexcited semiconductors: Coherent and incoherent dynamics," *Physical Review B*, vol. 46, no. 12, 1992.

[70] D. Cortie and R. Lewis, "Role of vanguard counter-potential in terahertz emission due to surface currents explicated by three-dimensional ensemble Monte Carlo simulation," *Physical Review B*, vol. 84, pp. 1–9, Oct. 2011.

[71] G. Klatt, *Charakterisierung neuartiger Terahertz-Emitter mittels schneller, praziser Terahertz-Spektroskopie*. PhD thesis, University of Konstanz, 2011.

[72] J. Tauc, "Generation of and emf in Semicondutors with Nonequilibrium Current Carrier Concentrations," *Reviews Of Modern Physics*, vol. 29, no. 3, pp. 308–324, 1957.

[73] T. Doi, K. Toyoda, and Y. Tanimura, "Effects of phase changes on reflection and their wavelength dependence in optical profilometry," *Applied optics*, vol. 36, pp. 7157–61, Oct. 1997.

[74] H. Yasuda and I. Hosako, "Measurement of Terahertz Refractive Index of Metal with Terahertz Time-Domain Spectroscopy," *Japanese Journal of Applied Physics*, vol. 47, pp. 1632–1634, Mar. 2008.

[75] K. Drexhage, "Influence of a dielectric interface on fluorescence decay time," *Journal of Luminescence*, vol. 1-2, pp. 693–701, 1970.

[76] A. Sommerfeld, "Mathematische Theorie der Diffraction," *Mathematische Annalen*, vol. 47, pp. 317–374, 1896.

[77] P. M. Morse and H. Feshbach, *Methods of theoretical physics*. New York: McGraw-Hill Book Company, Inc., 1953.

[78] M. Abramowitz and I. A. Stegun, *Handbook of Mathematical Functions, with Formulas, Graphs, and Mathematical Tables*. New York: Dover Publications, 1972.

[79] S. E. Ralph and D. Grischkowsky, "Trap-Enhanced Electric-Fields in Semi-Insulators - The Role of Electrical and Optical Ccarrier Injection," *Applied Physics Letters*, vol. 59, no. 16, pp. 1972–1974, 1991.

[80] N. Katzenellenbogen and D. Grischkowsky, "Efficient generation of 380 fs pulses of Tliz radiati'on by ultrafast laser pulse excitation of a biased metal-semiconductor interface," *Applied Physics Letters*, vol. 58, no. 3, 1991.

[81] M. Tani and K. Sakai, "Emission characteristics of photoconductive antennas based on low-temperature-grown GaAs and semi-insulating GaAs," *Applied Optics*, vol. 36, no. 30, pp. 7853–7859, 1997.

[82] M. E. Barnes, D. McBryde, S. A. Berry, P. C. Gow, G. J. Daniell, H. E. Beere, D. A. Ritchie, and V. Apostolopoulos, "Terahertz Emission From Lateral Surge Currents And Suppression Of dipoles Under A Metal Mask," in *2013 International Conference on Infrared, Millimeter, and Terahertz Waves*, 2013.

[83] M. E. Barnes, D. McBryde, P. C. Gow, S. A. Berry, G. J. Daniell, H. E. Beere, D. A. Ritchie, and V. Apostolopoulos., "Investigation Into The Role Of The Metal Mask And Pump Laser Illumination Parameters For Lateral Photo-Dember Emitters," in *2013 International Conference on Infrared, Millimeter, and Terahertz Waves*, 2013.

[84] J. K. Luo, H. Thomas, D. V. Morgan, and D. Westwood, "Transport properties of GaAs layers grown by molecular beam epitaxy at low temperature and the effects of annealing," *Journal of Applied Physics*, vol. 79, no. 7, p. 3622, 1996.

[85] S. Fleischer, C. D. Beling, S. Fung, W. R. Nieveen, J. E. Squire, J. Q. Zheng, and M. Missous, "Structural and defect characterization of GaAs and AlGaAs grown at low temperature by molecular beam epitaxy," *Journal of Applied Physics*, vol. 81, no. 1, p. 190, 1997.

[86] E. S. Harmon, M. R. Melloch, J. M. Woodall, D. D. Nolte, N. Otsuka, and C. L. Chang, "Carrier lifetime versus anneal in low temperature growth GaAs," *Applied Physics Letters*, vol. 63, p. 2248, Oct. 1993.

[87] I. S. Gregory, C. Baker, W. R. Tribe, M. J. Evans, H. E. Beere, E. H. Linfield, a. G. Davies, and M. Missous, "High resistivity annealed low-temperature GaAs with 100 fs lifetimes," *Applied Physics Letters*, vol. 83, no. 20, p. 4199, 2003.

[88] J. S. Blakemore, "Semiconducting and other major properties of gallium arsenide," *J. Appl. Phys.*, vol. 53, no. 10, 1982.

[89] D. McBryde, M. E. Barnes, P. C. Gow, S. A. Berry, G. J. Daniell, H. E. Beere, D. A. Ritchie, and V. Apostolopoulos., "Characterisation Of Low Tempreture And Semi-insulating GaAs Lateral photo-Dember THz Emitters," in *2013 International Conference on Infrared, Millimeter, and Terahertz Waves*, 2013.

[90] Z. Mics, A. D'Angio, S. A. Jensen, M. Bonn, and D. Turchinovich, "Density-dependent electron scattering in photoexcited gaas in strongly diffusive regime," *Applied Physics L*, vol. 102, no. 23, p. 231120, 2013.

[91] M. C. Beard, G. M. Turner, and C. A. Schmuttenmaer, "Subpicosecond carrier dynamics in low-temperature grown GaAs as measured by time-resolved terahertz spectroscopy," *Journal of Applied Physics*, vol. 90, no. 12, p. 5915, 2001.

[92] T. S. T. Sosnowski, T. B. T. Norris, H. H. Wang, P. Grenier, J. F. Whitaker, and C. Y. Sung, "High-carrier-density electron dynamics in low-temperature-grown GaAs," *Applied Physics Letters*, vol. 70, no. 24, p. 3245, 1997.

[93] Y. Shi, Y. Yang, X. Xu, S. Ma, W. Yan, and L. Wang, "Ultrafast carrier dynamics in AuGaAs interfaces studied by terahertz emission spectroscopy," *Applied Physics Letters*, vol. 88, no. 16, p. 161109, 2006.

[94] Y. Jin, X. F. Ma, G. a. Wagoner, M. Alexander, and X.-C. Zhang, "Anomalous optically generated THz beams from metal/GaAs interfaces," *Applied Physics Letters*, vol. 65, no. 6, p. 682, 1994.

[95] M. A. Ordal, L. L. Long, R. J. Bell, S. E. Bell, R. R. Bell, R. W. Alexander, and C. a. Ward, "Optical properties of the metals Al, Co, Cu, Au, Fe, Pb, Ni, Pd, Pt, Ag, Ti, and W in the infrared and far infrared.," *Applied optics*, vol. 22, pp. 1099–20, Apr. 1983.

[96] R. Singh, E. Smirnova, A. J. Taylor, J. F. O'Hara, and W. Zhang, "Optically thin terahertz metamaterials.," *Optics express*, vol. 16, pp. 6537–43, Apr. 2008.

[97] M. A. Ordal, R. J. Bell, R. W. Alexander, L. L. Long, and M. R. Querry, "Optical properties of Au, Ni, and Pb at submillimeter wavelengths.," *Applied optics*, vol. 26, pp. 744–52, Feb. 1987.